ADVANCED CONTROL STRATEGIES OF RENEWABLES SUPPORTING POWER SYSTEM OPERATION

XUE LYU

PhD

The Hong Kong Polytechnic University

2019

The Hong Kong Polytechnic University

Department of Electrical Engineering

Advanced Control Strategies of Renewables Supporting Power System Operation

XUE LYU

A thesis
submitted in partial fulfillment of the requirements for
the degree of Doctor of Philosophy

May 2019

CERTIFICATE OF ORIGINALITY

I hereby declare that this thesis is my own work and that, to the best of my knowledge and belief, it reproduces no material previously published or written, nor material that has been accepted for the award of any other degree or diploma, except where due acknowledgement has been made in the text.

___________________________(Signed)

__________Xue LYU______________________(Name of student)

Abstract

Renewable energy has gained significant attentions in recent years due to energy crisis and environmental awareness. Specifically, rapid development of wind and solar power generation has been witnessed around the world. However, the high penetration of renewable generation imposes severe challenges towards power grids operation. One negative influence is that system inertia becomes less and less as synchronous generators (SGs) are replaced by these electronic interfaced renewable generators. In addition, the power reserve requirement is accordingly increased due to the fluctuating and un-dispatchable characteristic of renewable generation. To cope with these challenges, this thesis is mainly focused on advanced active power control strategies of solar and wind power generation systems for providing system ancillary service.

In this thesis, a novel frequency control strategy is proposed for the two-stage three phase photovoltaic (PV) generation system, which involves simultaneously utilizing DC-link voltage control and the deloading control to support system frequency. When frequency variation is detected, the DC-link capacitor is utilized to provide inertia or frequency response. In addition, the deloading control is applied to reserve some PV generation beforehand. Therefore, the PV generation output can be up/down-regulated accordingly to also provide primary frequency support based on a droop control logic. Considering time varying characteristics of the irradiance and ambient temperature, the droop coefficient is adaptively adjusted in the proposed control strategy to improve the efficiency of the primary frequency regulation under

changing working conditions. The effectiveness of the proposed control strategy is verified through extensive case studies.

The maximum power point tracking (MPPT) control is usually adopted by wind turbines to maximize wind power harvesting. Besides the MPPT operation mode, the wind turbine can also regulate its output power according to system operator's commands. To achieve this, two power regulation control schemes are proposed for permanent magnet synchronous generator (PMSG) based wind turbine (WT). The first strategy aims to regulate power output through simultaneously utilizing the DC-link voltage control, rotor speed control and pitch angle control, while the second one coordinates these three controls in a hierarchical manner to reduce the overall impacts wind turbine operation, in which the power regulation tasks are allocated to individual control modules or their combinations dynamically in line with WT's operation states. Both control strategies implement active power regulation successfully, while the second control strategy outperforms the first one in the following aspects 1) requiring less activations of pitch angle control, and 2) imposing less impacts on wind energy harvesting. Case studies of the proposed control strategies are conducted to compare performance of the control strategies in active power regulation.

Owing to the increasing penetration of wind power in modern power systems, wind farms are expected to operate in a dispatchable manner to a certain extent by actively fulfilling dispatch orders sent from system operators. To coordinate mutually influenced wind turbines (WTs) within a wind farm due to non-negligible wake effects, a novel wind farm control strategy is proposed by 1) using the existing resources (i.e. kinetic energy (KE) and adjusting blade pitch angle) of doubly fed induction generator

(DFIG) based wind turbine to satisfy the dispatch order efficiently and reliably; 2) dynamically allocating power regulation tasks to individual wind turbine so that the loss of energy harvest can be reduced and wear outs caused by pitch control can be somehow mitigated. Extensive case studies are conducted out to verify the effectiveness of the proposed control strategy. Simulation results exhibit that the proposed strategy has better control performance in terms of total energy harvesting and pitching manipulation.

The ever-increasing penetration of wind energy in today's power system exposes the necessity of smoothing out power fluctuations in an effective and conducive way. Considering that adjusting wind power output using hard-coded filtering algorithms that can result in visually smoothed power output with unmeasurable impacts on system generation-demand balance. Therefore, a novel wind power smoothing control paradigm in context of performance-based regulation service is also proposed. Distinguished from conventional methods, the newly proposed control method smooths wind power output from a power system perspective by using the regulation mileage as a key performance indicator. To simultaneously address the system needs and maximize wind energy harvesting, a mileage-responsive framework is developed to enable wind farms to optimally generate smoothing power. The effectiveness of the proposed method is well demonstrated through case studies, of which the simulation results show a great potential for practical applications.

List of Publications Arisen from the Thesis

Technical Papers in Refereed Journals

[1] **Xue Lyu**, Zhao Xu, Jian Zhao, and Kit Po Wong, “Advanced frequency support strategy of photovoltaic system considering changing working conditions”, *IET Generation, Transmission & Distribution*, vol.12, no.2, pp. 363-370, 2017.

[2] **Xue Lyu**, Jian Zhao, Youwei Jia, Zhao Xu, and Kit Po Wong, “Coordinated control strategies of PMSG-based wind turbine for smoothing power fluctuations”, *IEEE Transaction on Power Systems*, vol. 34, no. 1, pp. 391-401, 2018.

[3] **Xue Lyu**, Youwei Jia, Zhao Xu, “A novel control strategy for wind farm active power regulation considering wake interaction”, *IEEE Transaction on Sustainable Energy*, accepted to be published.

[4] **Xue Lyu**, Youwei Jia, Zhao Xu, Jacob Østergaard, “Mileage-responsive wind power smoothing”, *IEEE Transaction on Industrial Electronics*, accepted to be published.

[5] **Xue Lyu**, Youwei Jia, Zhao Xu, “Revenue-aware power regulation schemes for variable speed wind turbines in a performance-based balancing market”, *IEEE Transaction on Sustainable Energy* (in revision).

[6] **Xue Lyu**, Youwei Jia, Zhao Xu, “Adaptive Frequency-responsive Control for Wind Turbines Considering Wake Interaction”, *Renewable Energy* (under review).

[7] Jingjing. Zhao, **Xue Lyu***, Yang Fu, Xiaoguang Hu, and Fangxing Li, “Coordinated microgrid frequency regulation based on DFIG variable coefficient using virtual inertia and primary frequency control”, *IEEE Transaction on Energy Conversion*, vol.31, no.3, pp. 833-845, 2016. (*Xue Lyu is the corresponding author)

[8] Youwei Jia, **Xue Lyu**, Zhao Xu, Minghua Chen, “Optimum-tracking approach to microgrid real-time scheduling regime”, *Journal of Modern Power Systems and Clear Energy*, accept to be published.

Conference Papers in Refereed Proceedings

[1] **Xue Lyu**, Zhao Xu, Jian Zhao, “A coordinated frequency control strategy for photovoltaic system in microgrid”, *The International Conference* on *on Electrical Engineering*, Weihai, China, Jul. 2017, pp. 1-5.

[2] Youwei Jia, Yufei He, **Xue Lyu**, Songjian Chai, Zhao Xu, “Hardware-in-the-loop Implementation of Residential Intelligent Microgrid”, *2018 IEEE PES General Meeting*, Portland, USA, Aug. 2018, pp. 1-5.

[3] **Xue Lyu**, Youwei Jia, Zhao Xu, and Xu Xu, " An active power regulation strategy for wind farm considering wake effect," *2018 10th IEEE/PES Innovative Smart Grid Technologies*, Washington D.C., USA, Feb. 2019, pp. 1-5.

Acknowledgements

Undertaking this PhD is really a memorable and a significant experience for me. I would like to extend thanks to many people who generously gave me support and guidance.

First and foremost, I would like to express my sincerest gratitude to my supervisor, Professor Zhao Xu, for his guidance and encouragement throughout my entire PhD study. I really appreciate that Prof. Xu took a chance on me so that I can pursuit a higher level of degree. It was Prof. Xu's trust offered me this valuable opportunity to prove myself worthy. Without his guidance this PhD would not have been achievable. I will never forget Prof. Xu's rigorous research attitude and I will work harder in the future to live up to his expectation.

I am grateful to Professor Zhaoyang Dong, who hosts me during my visit at University of New South Wales. It was fantastic to have the opportunity to study in Porf. Dong's lab.

Many thanks to my lab-mates. Especially for Dr. Y. W Jia, who gave me valuable advices and selfless help in both academy and life. I will never forget the discussions we had, days and nights we worked together.

Thanks go to my family for their unbelievable support. They are the most important people in my world and I dedicate this thesis to them.

Last but not the least, I would like to knowledge the support from Ph.D studentship awarded by The Hong Kong Polytechnic University.

Table of Contents

List of Figures

List of Tables

List of Abbreviations

MPPT	Maximum Power Point Tracking
PV	Photovoltaic
PFC	Primary Frequency Control
VSWT	Variable Speed Wind Turbine
WT	Wind Turbine
ESS	Energy Storage System
PCC	Point of Common Coupling
KE	Kinetic Energy
PMSG	Permanent Magnet Synchronous Generator
DFIG	Doubly Fed Induction Generator
WF	Wind Farm
LPF	Low Pass Filter
MA	Moving Average
PID	Proportional–Integral–Derivative
UC	Ultra-Capacitor
LB	Lithium-ion Battery
SMES	Superconducting Magnetic Energy Storage
IR	Inertial response
SFC	Secondary Frequency Control
RoCoF	Rate of Change of Frequency
SG	Synchronous Generator
MPP	Maximum Power Point
STC	Standard Test Condition
RSC	Rotor Side Converter
GSC	Grid Side Converter
AGC	Automatic Generation Control
RMSE	Root Mean Square Error
MAPE	Mean Absolute Percentage Error

Chapter 1 Introduction

1.1 Backgrounds

As clean sources of energy, wind and solar generation are receiving increasing attention and showing rapid development across the world in recent years. According to the global wind power market outlook update, more than 680GW of new wind power capacity will come online on a global scale over the next 10 years. The international energy agency predicted that solar power would contribute 16 percent of the worldwide electricity consumption by 2050 [1]. However, unlike conventional power plants, wind energy conversion systems and solar energy conversion systems are interfaced with grid through power electronic converters. The main function of these converters is to realize the maximum power point tracking for harvesting wind/solar energy. In addition, with solar/wind generation is decoupled from grid frequency due to the power electronic control system, and then zero or little inertia can be contributed to system. In this context, the intermittency and un-dispatchable nature of wind/solar power generation pose new challenges for power system operation.

To address the above-mentioned issues, solar and wind energy systems should no longer operate at the “free-running” mode and are required to meet some technical requirements specified by system operators. For example, some grid companies including e.g. E.ON Netz, Hydro-Québec TransÉnergie require that grid connected renewables should possess frequency regulation capability [2-4]. Besides, renewables are required to be capable of actively fulfilling dispatch orders from system operators. It can be speculated that solar/wind energy system would be required to operate like conventional generators in the near future.

1.2 Introduction and Literature Review

1.2.1 Frequency Control Strategies for Solar Systems

Solar systems usually operate at MPPT mode when connecting into grid to ensure the optimal energy harvest. Accordingly, the frequency regulation ancillary service is undertaken by conventional generators. Under this background, maintaining frequency stability in a system with high solar power penetration is a challenging issue.

In recent years, some research has been conducted on how to enable wind systems to provide frequency response, of which strategies can be classified into two types with the first one termed as “virtual inertia control” [5-7], and the second one involving deloading generation as power reserve for primary frequency control [8-10]. By comparison, less investigation has been conducted on solar systems providing frequency regulation service up to now.

Emulated Inertia Control: System inertia contributed via synchronous generators’ rotational rotor is an important system parameter [11, 12], as it determines the immediate system frequency response whenever supply and demand imbalance occurs. Traditionally, solar systems do not possess rotating mass and they cannot offer any inertia contribution. In fact, the DC-link capacitor, which exists in wind energy conversion system and the two-stage solar energy conversion system, has the potential to store or release a certain amount of energy. Hence solar system has the potential to emulate inertial response. E.g. [13] proposes the control strategy that exploiting the energy stored in DC-link capacitor to smooth out power fluctuations. [14] makes use of the capacitor as a buffer to improve system stability. In the same way, with the implementation of a proper control strategy, the two-stage PV systems could contribute inertia support to system.

Deloading Control for Primary Frequency Regulation: The primary frequency control (PFC) is an important way to maintain system frequency stability. Broadly speaking, the primary frequency regulation is mainly contributed by conventional synchronous generators. The function of governor configurated in SGs is to guarantee the rotational speed inversely proportional to the power output. Thus, turbine power would increase/decrease in response to frequency variation. Recently, there are some works dealing with PV systems joining in primary frequency regulation. The focus has been put on incorporating energy storage systems (ESS) with PV farms [15-19]. Certainly, this kind of method involves massive investment and therefore unacceptable from the perspective of PV farm owners. According to [20], the ESS cost is higher and its lifetime is shorter compared with components of PV systems themselves. Consequently, frequency control strategies that involves deloading PV generation output as primary reserve are developed. In [21], the deloading control is achieved by forcing PV arrays operate at lower voltage level than the maximum power point (MPP). As reported in [22], the deloading control is implemented by forcing PV arrays operate at higher voltage level than MPP. Besides, a number of PV arrays are disconnected from inverter through DC-relays to curtail power production in [23]. The newton quadratic interpolation (NQI) algorithm is adopted in [24] to obtain the active power reference for PV system to provide frequency response. A droop control strategy is put forward in [25] to establish the linear relationship between active power support provided by PV generators and frequency deviation. However, the feasibility of the proposed control strategies under changing working conditions are seldom considered in previous works. In practical operation, it is difficult to guarantee solar power generation to reach a required deloading level through controlling PV side dc bus voltage due to the time-varying irradiance and temperature. Although local environment variation is considered in [26] during scheduling PV systems, the proposed control algorithm is complex and has a heavy computation burden. Given that research on frequency regulation of PV systems is still in its early stage, further study should take time-varying working conditions into account when designing frequency control strategy.

1.2.2 Active Power Regulation for Variable Speed Wind Turbines

Among all kinds of wind turbines, the variable speed wind turbines (VSWTs) including the doubly-fed induction generator (DFIG) based wind turbines, the permanent-magnet synchronous generator (PMSG) based wind turbines are widely installed in industry due to their relatively high efficiency and low cost [27]. In this thesis, both DFIG-WTs and PMSG-WTs are considered to verify the proposed active power control strategies.

Resources Utilized for Wind Power Regulation: Delving into the greatest potential of the wind turbine itself for active power regulation has attracted wide attention in both industry and academia in recent years. Such resources consisting of the following three aspects can be synthesized as the self-capability of WTs for power generation adjustment.

The first resource that can be utilized to regulate wind power output is the pitching control, as it directly determines the mechanical power capture capability of WTs. In general, pitch angle control only activates in high wind speed conditions to prevent rotor overspeed. To achieve the power regulation objective, the pitch angle control would activate under below-rated wind speed conditions [28-33]. The pitch angle control could be utilized in whole wind speed region, rendering a large active power regulation range. However, it has a low wind energy harvesting efficiency as the curtailed wind power is directly discarded. Besides, frequent pitch angle manipulation would unavoidably increase mechanical stress and fatigue of WTs.

Another resource that can be used to regulate wind power output lies in the kinetic energy stored in the rotating mass [34-47]. Once the dispatch command is received, the rotating mass can extend wind power generation via KE charging/discharging. To define the relationship between the dispatch command and rotor speed variation, a fuzzy proportional–integral–derivative (PID) controller is established in [41]. In [43], the frequency deviation is introduced as an input signal to the conventional speed controller. Depending on whether the frequency response is required to provide, WTs can switch to a temporary power injection mode in [46] and the set-point is tracked as the new reference with the stored KE delivered into system. Even though the operating point of WT is shifted away from the maximum power point (MPP) when rotor speed control is applied, it has an advantage on energy harvesting compared with pitch angle control as certain amount of energy can still be stored in the rotating mass in the form of KE rather than discarded otherwise.

The last resource that can be utilized is the DC-link capacitor. The DC-link voltage can be varied within a certain range and provide extra active power support. To exploit the energy stored in it, a DC-link voltage controller is introduced in [13, 48-50], in which the DC-link voltage variation is decided by the ratio of the power deviation (i.e. the deviation between dispatch command and actual wind power generation) and DC-link current. However, the regulation effect of the method proposed in [13, 48] can be significantly limited once DC-link voltage reaches to its upper/lower limits, at which the DC-link current shall become zero and thereby the voltage variation would go to infinity. In [49, 50], a proportional relationship between the frequency deviation and voltage variation is established. Compared with pitch angle control and rotor speed control, DC-link voltage control is the most preferable option as it won't affect WTs' MPPT control. However, it should be noted that the available energy in the DC-link capacitor is relatively small.

It is challenging to coordinate the above mentioned three kinds of resources in an effective way. In pioneering works, how to coordinate and utilize these concerned resources for active power regulation has not been well investigated. To fill in this gap, this thesis extensively investigates how to adequately exploit all existing resources and efficiently coordinate them to follow the dispatch order under dynamic working conditions.

Active Power Regulation Strategies at Wind Farm Level: The wind farm could become a dispatchable resource and track the dispatch order given a proper strategy. In [51], the balance between generation and consumption is achieved by controlling the utilization level of each WT to an identical value. A two-layer structured active power regulation scheme is proposed in [52, 53], where the upper layer controller coordinates the operating states of all WTs, and the lower layer controller regulates power generation of individual WT. In [52], the distributed model predictive control is adopted to generate the power reference of individual WT. To minimize wind energy loss during frequency regulation process, [53] assigns the power references among multiple WTs via a centralized optimal dispatch strategy. A distributed control method is proposed in [54] for the WF imitating the inertia and droop characteristics to provide fast frequency response. Taking the trade-off between power reference tracking and minimization of the wind turbine mechanical load into consideration, a distributed model predictive control is developed in [55]. Typically, the simplified model, i.e. the wind farm is uniformly aggregated by single wind turbines, is adopted in most research works while the aerodynamic coupling among wind turbines (i.e. the wake effect) is neglected. It should be noted that wake effect modelling is a challenging issue due to the high nonlinearity involved. The existing work to handle wake interactions can be classified into two types, i.e. by using i) optimization techniques to generate optimal control reference [56-64], and ii) advanced control strategies for individual wind turbines [65, 66]. For the first type, the formulated optimization problem is highly nonlinear and nonconvex. Thus, the solution qualify will significantly influence the control effectiveness. Furthermore, heuristic optimization techniques (e.g. particle swarm optimization and genetic algorithm etc.) are generally utilized to solve such problem, hence the process of reaching the optimum can be unstable and time consuming (especially for a large-scale wind farm). Therefore, this type of approaches can hardly be utilized in an online fashion. By far, research about the second type of approaches is still at its early stage. Given that the energy compromised by individual WT in the WF is different, [66] proposes a variable utilization level control scheme for WTs, where the utilization level of WTs in different rows is set as linear-inversely proportional to its rotor speed. In [65], the KE storage capability is used to offer a buffer for power dispatch, and a consensus algorithm is utilized to ensure the KE utilization ratio among multiple WTs can be reached to an identical value.

1.2.3 Control Strategies for Smoothing Out Wind Power Fluctuations

The increasing wind power penetration may give rise to detriment of power quality owing to its uncertain and intermittent characteristic [67-69]. The VSWTs are nonsynchronous grid connected resources and their free-running operation characteristic intensifies power fluctuations and thereby threaten power system stability. Especially, wind power fast fluctuations leads to frequency variation, system instability [70-72], variation of reactive power loss and voltage flicker at the point of common coupling (PCC) to the main grid [73]. Besides, other technical and economic issues are brought along by wind power fluctuations, e.g. less operational efficiency of thermal units [74], higher reservation cost of power reserve [75], high transmission capacity requirement and high transmission losses [76]. It is straightforward that wind power fluctuations result in more operational challenges for the islanded power systems. Accordingly, smoothing power fluctuations can be significantly beneficial to their stable operation.

Smoothing Reference: Till date, various wind power smoothing approaches have been developed, whereas a general scientific question—to which extent such “smoothed” wind power could indeed contribute to the grid operation—still remains open. The smoothing control reference in some pioneering works is typically generated by hard-coded algorithms. For example, the first order low pass filter (LPF) is utilized in [77-79] to smoothen out high-frequency components contained in wind power fluctuations, in which the smoothing performance is depend on the filtering time constant. Likewise, the moving average (MA) algorithm is used in [80, 81] to eliminate the short-cycle power fluctuations, where the smoothing performance is relying on the selected time window. In [82-84], wind power fluctuations are smoothened by pre-setting ramp limits. A gaussian-based smoothing algorithm and a fuzzy wavelet transform method are reported in [85] and [86] respectively to suppress wind power fluctuations. Such references are only dependent on autogenous wind power generation profiles yet are weakly correlated with grid frequency stabilization; In addition, there lacks a consideration of wind turbine operational constraints, such that obtained references can be technically ineffective in terms of unreasonable over-/under-production demand; and it might be economically inefficient by arbitrarily sacrificing a significant amount of wind energy through predefined hard-coded smoothing mechanism.

Strategies to Trace Smoothing Reference: Till date, methods to follow the smoothing reference in pioneering works can be classified into two categories. The first category is to take advantage of energy storage systems to store excessive energy and release back to grid once required. In [82], the ultra-capacitor (UC) bank and the lithium-ion battery (LB) bank are configurated to smooth out short-term and long-term wind power fluctuations, respectively. Other ESSs such as flywheel and superconducting magnetic energy storage (SMES) have also been utilized in [87-91]. However, such approach inevitably involves heavy investments. Different from the first kind of approach that rely on additional ESSs, the second category pursues to exploit the greatest potential of the WT itself for power smoothing. This kind of strategies is superior over ESSs based ones due to the less investment cost and maximum utilization of the existing resources of WT.

As mentioned above, there are three resources that can be utilized to regulate wind power output. Therefore, control strategies that utilize the existing resources to smooth out power fluctuations could be categories into three classes, i.e., DC-link voltage regulation based control [13, 48], rotor speed regulation based control [39-41] and pitch angle regulation based control [31, 32]. Exploiting the energy stored in the DC-link capacitor to smoothen out wind power fluctuations possess a rapid speed and would not impact the MPPT control of WTs. However, the capacity of the capacitor is limited, especially for the DFIG-WTs. The rotor speed control exploits KE stored in the rotational rotor to smooth out wind power fluctuations. In particular, WTs could withhold power generation and store partial energy in its rotational rotor via rotor speed acceleration in deloading scenarios. The stored KE can be released back to system in overloading scenarios via rotor speed deceleration. The captured mechanical power of WTs can also be smoothed via adjusting blade pitch angle. However, without deloading control in advance to obtain power reserve, pitch angle control can only apply to conditions that power production should be reduced as it does not possess energy storage capability.

1.3 Primary Contributions

To provide ancillary service for system operation, this thesis investigates into some novel control strategies to fulfil the goal of active power regulation of renewables. The primary scientific contributions are summarized as follows:

1. A simultaneous DC-link voltage control and deloading control is proposed to adequately exploit the self-potential of PV systems for providing frequency response. The energy stored in the DC-link capacitor is utilized to emulate the temporary inertial response. In addition, a deloading based control strategy is proposed for offering a long-term primary frequency

control. Considering that the primary frequency contribution is directly determined by the droop gain, a variable droop control strategy is proposed to adaptively adjust the frequency contribution according to the available primary reserve capacity. The effectiveness of the proposed control strategy is verified through analyzing system dynamic frequency behavior in various scenarios.

2. Two control schemes for PMSG-based WT active power regulation are proposed via taking advantage of the DC-link voltage capacitor, rotational rotor and blade pitch angle adjustment. The first control scheme aims to regulate wind power generation by utilizing these three resources simultaneously. It is straightforward that such controller may suffer from a semi-optimal effect in terms of WT mechanical fatigue, energy harvesting rate and so forth, as it needs frequent variation of rotor speed and blade pitch angle. To overcome the above-mentioned problems, the second strategy pursues to take advantage of these three resources in a hierarchical manner. In particular, the regulation task is intelligently fed into each individual resource according to a rule-based algorithm. Both two proposed control schemes are verified through extensive case studies.
3. At the supervisory WF control level considering wake interactions, to provide active power regulation service while achieves the goal of adequately utilizing the KE storage as a buffer and reducing manipulation frequency of blade pitch angle at the same time, an adaptive method to assign the active power regulation task among multiple WTs is proposed.

Distinguished from other control strategies that do not consider the cooperation among multiple WTs, merits of the proposed strategy lie in the following aspects: 1) wind turbine system-friendliness (i.e. less actuation time of blade pitch control to reduce operational wear outs); 2) energy utilization efficiency; 3) over-/under-production capability of wind turbines at instant moments; and 4) control efficiency. The effectiveness of the proposed control strategy is verified under different working conditions, where wind speed fluctuations and load variations are both taken into account.

4. The wind power smoothing control with its consequent effects on system frequency regulation service cost is incorporated in this thesis. A receding horizon control framework is newly proposed, which consists of an optimization module to generate the optimal control reference by taking wind-fluctuation-induced frequency stabilization cost into consideration, and a real-time control module to timely track the smoothing reference for individual WT. It is worth noting that the proposed framework is distinguished among most existing works in this field and holds significant merits as 1) smoothing reference is obtained through system-perceived optimization; and 2) the effectiveness of WT over-/under-production at instant moments can always be ensured through practical-constrained cascade control. Besides, it is worth noting that the computational efficiency of the formulated optimization is satisfactorily high.

1.4 Thesis Layout

The remainder of the thesis is organized as follows. Chapter 2 proposes a simultaneous DC-link voltage control and primary frequency control for PV systems to provide frequency regulation support. In terms of the active power regulation of WT, Chapter 3 presents two control schemes of PMSG-based WT through utilizing the DC-link capacitor, the KE stored in the rotational rotor and the adjustment of blade pitch angle. WT can follow the dispatch order required from system operator with advanced control strategies are adopted. When it comes to active power regulation strategy of wind farm, the active power regulation strategy would be different from individual WT due to the complicated wake effect. A novel control strategy is proposed at the WF level in Chapter 4 to coordinate WTs to fulfill the dispatch order in presence of wake effect. Considering that the wind power fluctuations would bring negative effect on system operation, an optimal wind power smoothing control framework is developed in Chapter 5, where the smoothing command is optimized from an economic perspective. Eventually, Chapter 6 concludes this thesis, and provides perspectives for future work.

Chapter 2 Advanced Control Strategy of Photovoltaic System for Providing Frequency Support

Nomenclature

H_{s}	System equivalent inertia constant
S_{total}	System total capacity
H_{i}	Inertia constant of generator *i*
S_{i}	Capacity of generator *i*
δ	Rotor angle
ω	Rotor speed
ω_0	Synchronous speed
H	Inertia constant
P_m	Mechanical power
P_e	Electrical power
f	Measured system frequency
ΔP_{dc}	Charging/discharging power of DC-link capacitor
P_{pv}	Power captured by PV array
P_{inv}	Power delivered to system from DC-AC inverter
C_{dc}	Capacitance of the DC-link capacitor
U_{dc}	DC-link voltage
H_{dc}	equivalent inertia constant of DC-link capacitor
U_{dc0}	Nominal DC-link voltage
f_0	Nominal system frequency
ΔU_d	Voltage increase of PV side dc bus to achieve deloading
ΔU_E	Voltage increase due to irradiance variation
ΔU_T	Voltage increase due to temperature variation

ΔU_{STC} Voltage increase in standard test condition

Δf Frequency deviation

R Droop parameter

ΔP Change of solar power generation

P_{res} Primary power reserve

P_{mpp} Maximum solar power production

P_{meas} Measured solar power production

λ Deloading coefficient

This chapter is organized as follows. Frequency control strategies for power systems are illustrated in Section 2.1. The simultaneous DC-link voltage control and deloading control of PV systems for providing frequency support is proposed in Section 2.2. Case studies and simulation results are discussed in Section 2.3. The summary is given in Section 2.4.

2.1 Frequency Control Strategies of Power Systems

The conventional synchronous generators are power controllable units from system perspective and the secure and reliable system operation are mainly dependent on them. Their output power can be adjusted to balance the production and consumption, and in turn maintains the frequency stability. Broadly speaking, frequency response of conventional generators is carried out in different successive steps, which can be roughly divided into three categories: the inertial response (IR), the primary frequency control (PFC), and secondary frequency control (SFC). When a load increase or generation loss disturbance occurs, the typical system frequency response is shown in Fig. 2.1.

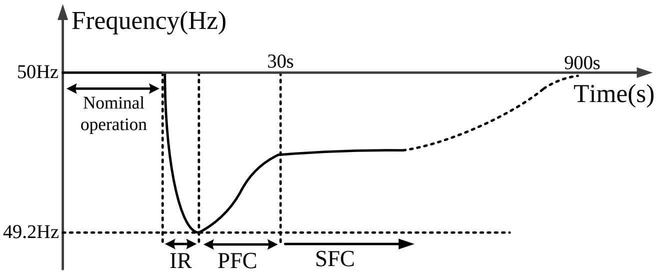

Fig. 2. 1 Frequency response when loss generation or increase load.

2.1.1 Inertial response

The rate of change of frequency (RoCoF) behaviour is closely dependent on total system inertia [92], which is mainly contributed by spinning generators. When power unbalance event occurs, the electrical torque reference T_e changes immediately to counterbalance frequency change. However, the mechanical torque T_m would not change within a short time. As a result, the mismatch between the electrical torque T_e and mechanical torque T_m leads to acceleration or deceleration of rotor speed. Finally, the kinetic energy is fed into or taken from the system to restrain the RoCoF. The transfer function of rotor speed deviation and torques can be seen in Fig. 2.2.

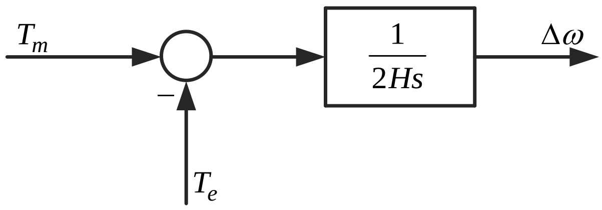

Fig. 2. 2 Transfer function relating speed and torques.

The equivalent inertia constant of the power system can be calculated by the following mathematical formula,

$$H_s = \frac{\sum_{i=1}^{n} H_i S_i}{S_{total}} \tag{2.1}$$

where H_s and S_{total} are the equivalent inertia constant and total capacity of all generators in the system, H_i and S_i are the inertia constant and the capacity of the synchronous generator i.

However, renewables that interfaced with electronic converters cannot contribute any inertia as their power production is decoupled from system frequency. With the increasing penetration of renewables, the system equivalent inertia constant could be significantly reduced. Under this background, the rate of change of frequency behaviour would become worse when suffering from a disturbance.

2.1.2 Primary Frequency Control and Secondary Frequency Control

The PFC aims to stabilize system frequency at a quasi-steady state value after the disturbance. As required by the grid code in England, the PFC should activate within 2s after the disturbance and the support should be fully deliverable to grid at 10s. In addition, the primary reserve should be maintained, where necessary, for a further 20s [93]. According to [94], the instantaneous frequency must not fall below 49.2Hz and rise exceed 50.8Hz when disturbance occurs. Moreover, the quasi-steady-state frequency deviation should not exceed ±180mHz. The conventional generators contribute to system primary frequency regulation by adjusting the valve or gate position of turbines, which in turn changes the mechanical power from the prime motor. With the increasing penetration of renewable energies in the system, the total primary reserve capacity would be decreased. This is a severe challenge for system operator to guarantee the dynamic frequency behavior varying within the permissible range. The main objective of SFC is to ensure the frequency can be brought back to the nominal value and to remain the interchange power between control areas at the scheduled values. A central controller is required for the SFC to generate the active power set points of selected generators. Noted that the SFC is not considered in this Chapter, as it aims to reschedule the active power set points of selected generators in a relatively long time-frame, e.g., it activates about 30s after the disturbance and ends with 15 minutes.

2.2 Advanced Frequency Control Strategy for PV Systems

2.2.1 Overview of the Proposed Frequency Control Method

A typical two-stage PV system is given in Fig. 2.3, where the PV array, DC-DC converter, DC-link capacitor and DC-AC inverter etc are comprised. The primary objective of DC-DC converter is to realize MPPT and to boost the voltage of PV array to an appropriate level. The DC-AC inverter is mainly responsible for controlling the DC-link voltage and transforming the DC current into AC one. More details about PV system topology and control can be referred to [95].

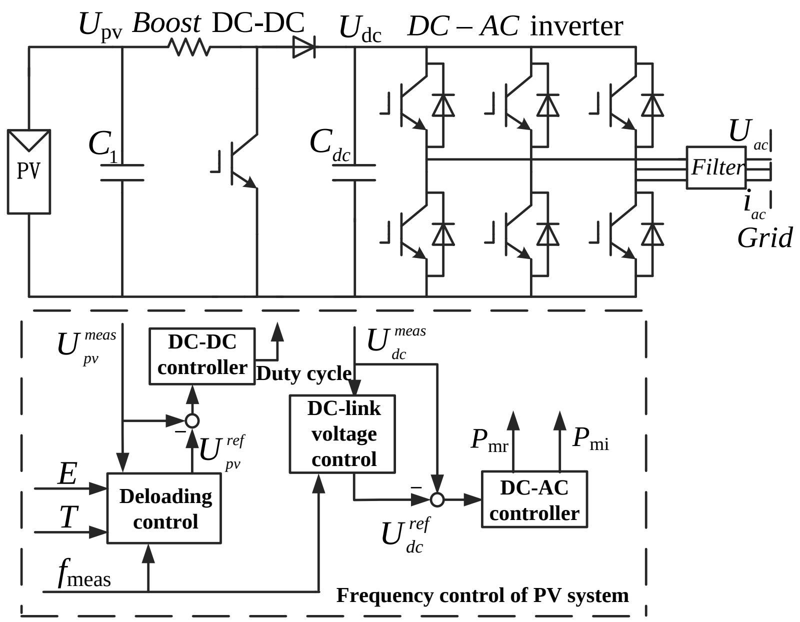

Fig. 2. 3 System outline of PV system and control scheme of the simultaneous frequency control.

It can be found that there is a DC-link capacitor at in the two-stage PV system. The energy stored in the DC-link capacitor can be exploited to provide rapid but temporary inertial response. Considering that the limited capacity of the DC-link capacitor, a deloading control is adopted to provide primary control reserve. Hence, the output power can be adjusted upward or downward power to further counterbalance frequency variations. Even though the deloading control brings economical loss to the PV farm owner, it improves the operation security, especially for the PV dominated microgrid. With the implementation of the proposed simultaneous control strategy, the full potential of PV systems for grid frequency support could be unleashed.

2.2.2 Emulated Inertia Control

The rotor dynamics of a synchronous generator is given in (2.2) in per unit,

$$\begin{cases} \frac{d\delta}{dt} = (\omega - 1)\omega_0 \\ \omega \frac{d\omega}{dt} = \frac{1}{2H}(P_m - P_e) \end{cases} \tag{2.2}$$

where δ denotes rotor angle, ω denotes rotor speed, ω_0 denotes the synchronous speed, H denotes inertia constant, P_m denotes mechanical power, and P_e denotes electrical power.

As shown in Eq (2.2), the rotor speed variation is determined by the mismatch between the mechanical power and the electrical power. The rotor speed can be replaced by system frequency and then Eq (2.2) can be rewritten as,

$$P_m - P_e = 2H\omega \frac{d\omega}{dt} = 2Hf \frac{df}{dt} \tag{2.3}$$

Neglecting the inverter loss, the dynamics of DC-link capacitor voltage U_{dc} can be illustrated as,

$$\Delta P_{dc} = P_{pv} - P_{inv} = C_{dc} U_{dc} \frac{dU_{dc}}{dt} \tag{2.4}$$

where P_{pv} is the power captured by PV array, P_{inv} is the power delivered to system from DC-AC inverter, C_{dc} is the capacitance of the DC-link capacitor. Under normal operation, the DC-link voltage should be maintained at 1 p.u. and ΔP_{dc} equals to 0. When imbalance between P_{pv} and P_{inv} occurs, the capacitor will be charged/discharged accordingly with its voltage deviating from the nominal value. Based on Eq (2.3) and Eq (2.4), it can be found that characteristic of DC-link capacitor is similar with the swing equation of synchronous generators. In this context, the DC-link capacitor can emulate inertial response and the dynamic process can be expressed as,

$$C_{dc}U_{dc}\frac{dU_{dc}}{dt} = 2H_{dc}f\frac{df}{dt} \tag{2.5}$$

where H_{dc} denotes the equivalent inertia constant of DC-link capacitor. Integrating both sides of Eq (2.5),

$$\int_{U_{dc0}}^{U_{dc}} C_{dc}U_{dc}dU_{dc} = 2\int_{f_0}^{f} H_{dc}fdf \tag{2.6}$$

$$\frac{1}{2}C_{dc}(U_{dc}^{2} - U_{dc0}^{2}) = H_{dc}(f^{2} - f_0^{2}) \tag{2.7}$$

where U_{dc0} is the nominal DC-link voltage, f_0 is the nominal system frequency. Via linearization and ignoring high-order terms, Eq (2.7) can be rewritten as,

$$CU_{dc0}(U_{dc} - U_{dc0}) = 2H_{dc}f_0(f - f_0) \tag{2.8}$$

$$U_{dc} = \frac{2H_{dc}f_0}{C_{dc}U_{dc0}}(f - f_0) + U_{dc0} = K_{in}(f - f_0) + U_{dc0} \tag{2.9}$$

Rearranging Eq (2.8), Eq (2.9) is obtained. According to Eq (2.9), a linear proportional relationship between the DC-link voltage variation and frequency deviation can be established. Hence a control loop is introduced as shown in Fig. 2.4. When system frequency variation is detected, the DC-link voltage reference U_{dc}^{ref} would be changed according to the predetermined proportional relation. To restrain excessive voltage variation, the DC-link voltage to is constrained to vary within 0.86-1.14 p.u.. In this chapter, the capacitance of the DC-link capacitor is 30000 μF and K_{in} is set to 10 to achieve satisfactory transient response through trial and error.

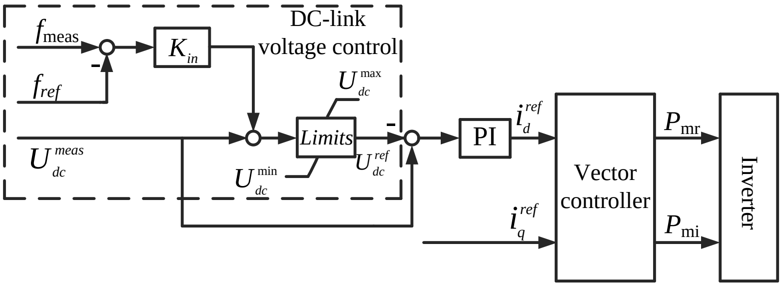

Fig. 2. 4 The proposed DC-link voltage control scheme.

2.2.3 Deloading Control

In a PV embedded microgrid, the deloading control can enhance operation security and facilitate the primary frequency regulation sharing among participants. Firstly, the total power reserve capacity of the microgrid is increased owing to the primary reserve provided by PV systems. Besides, the primary reserve from PV systems are distributed inside the microgrid so that the congestion is accordingly avoided. In this context, the frequency regulation burden of conventional generators can be significantly relieved since PV systems share the primary frequency regulation responsibility.

2.2.3.1 Implementation Method to Achieve Deloading

The deloading control in this chapter is achieved by forcing PV arrays operate at a voltage larger than the value at MPP. To ensure that the deloading control can be easily carried out under time varying irradiance and temperature conditions, a look-up table method is adopted due to its advantage on response speed and accuracy.

The I-V and P-V characteristic curves of PV systems under different irradiance and temperature conditions are demonstrated in Fig. 2.5. It can be found that there exists a specific dc voltage (dots in Fig. 2.5) guarantees the maximum solar power capture under a certain irradiance and temperature. Theoretically, PV arrays would shift away from the MPP either via increasing PV side dc bus voltage or decreasing. However, the curve slope at the right side of MPP is generally larger than the left side, as shown in Fig. 2.5(c) and (d). Hence a small increase in dc voltage could gain the required deloading level. That's the reason why the increasing voltage method is applied to achieve deloading herein. Since the power production of PV system is directly related to the local environment (i.e. irradiance and temperature), the corresponding voltage increase of PV side dc bus can be divided into two parts, with one part attributed to the irradiance variation, and the other one attributed to the temperature variation, as shown in Eq (2.10).

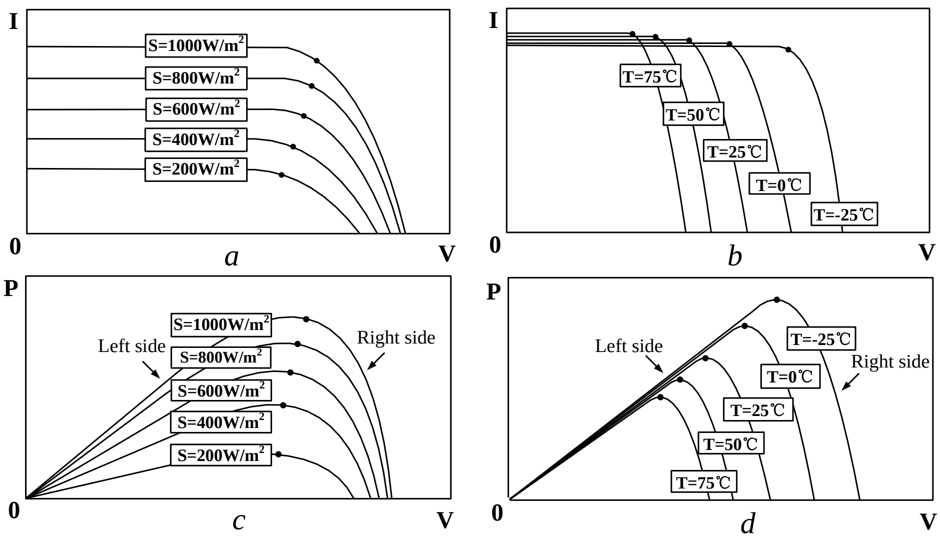

Fig. 2. 5 I-V and P-V characteristics of solar PV (a) I-V characteristic under changing irradiances, (b) I-V characteristic under changing temperatures, (c) P-V characteristic under changing irradiances, (d) P-V characteristic under changing temperatures

$$\Delta U_d = \Delta U_E + (\Delta U_T - \Delta U_{STC}) \tag{2.10}$$

where ΔU_E denotes the dc bus voltage increase when solar irradiance varies while the temperature is fixed at 25^0C. ΔU_T denotes the dc bus voltage increase when temperature varies while the solar irradiance is fixed at 1000W/m^2. ΔU_{STC} stands for the dc bus voltage increase under standard test condition (STC) (i.e. where the solar irradiance E is 1000W/m^2, and the temperature T is 25^0C). According to the power characteristic curves given in Fig. 2.5, the captured solar power can be regulated via adjusting PV side dc bus. To achieve the required deloading level, the first step is to adjust PV side dc bus voltage and measure the solar power generation. The voltage can be continuously tuned via try and error method until the required deloading level is achieved. Two lookup tables of ΔU_E versus E and ΔU_T versus T are obtained and ΔU_d can be defined as the combined effects of E and T.

2.2.3.2 Variable Droop based Primary Frequency Control

Since the power generation of PV system is directly dependent on local irradiance and temperature, which in turn influence its power reserve capacity, it is important to let the primary frequency regulation contribution adjustable. To dynamically adjust the primary frequency regulation support PV system provides under different working conditions, a variable droop method is proposed in this section.

In the primary frequency control scheme, the droop parameter is utilized to represent and reflect the share of primary frequency regulation, which can be defined as,

$$\Delta f = R \cdot \Delta P \tag{2.11}$$

where R is the droop parameter, Δf is frequency deviation and ΔP is the change of solar power generation. The droop parameter is usually expressed as a percentage, which indicates the power-frequency characteristic of the generator. Broadly speaking, a large parameter setting would lead to small primary control contribution and in turn reserve surplus. In contrast, a small parameter setting would contribute more primary frequency regulation support but might lead to system instability.

In general, the droop parameter of conventional generators is fixed and set as a constant, and it is determined according to their rated capacity and the primary control reserve capacity. For example, steam turbines equipped with electro-hydraulic governors typically have a droop parameter ranging from 2.5% to 8% [96]. However, the fixed droop parameter setting is not suitable for PV systems as their power generation and reserve capacity are dynamically changing. Considering the characteristic of renewables, a variable droop parameter setting for DFIG-based WT is proposed in [10], where the droop parameter is set according to the measured wind speed. However, it should be noted that there are more factors affecting solar power production. To adequately exploit of the primary frequency contribution of PV systems under time varying conditions, the droop parameter is set to be linear inversely proportional to the reserve capacity, given as,

$$\frac{1}{R} \propto P_{res} \tag{2.12}$$

$$P_{res} = P_{mpp} - P_{meas} \tag{2.13}$$

$$P_{res} = \lambda P_{mpp} \tag{2.14}$$

where P_{res} denotes the primary power reserve, P_{mpp} denotes the maximum solar power production, P_{meas} denotes the measured actual solar power production, and λ denotes deloading coefficient. By substituting Eq (2.14) into Eq (2.13), the relationship between the primary power reserve and the measured active power production can be described as,

$$P_{res} = P_{meas}\left(\frac{1}{1-\lambda} - 1\right) \tag{2.15}$$

It can be seen from Eqs (2.12-2.15) that the droop parameter is linear inversely proportional to solar power production and the deloading coefficient. Assuming that the deloading coefficient is predetermined as a constant, the reciprocal of R is only linear proportional to the solar power production and the droop parameter can be determined according to,

$$\frac{1}{R} = \frac{P_{meas} - P_{\min}}{P_N - P_{\min}}\left(\frac{1}{R_{\min}} - \frac{1}{R_{\max}}\right) + \frac{1}{R_{\max}} \tag{2.16}$$

where P_{N} is the nominal power of the solar system, $P_{\min}$ is the solar power generation when the deloading control is activated, whose setting can be tuned based on the specific requirement of system operations.

The schematic diagram of proposed deloading based primary frequency control is given in Fig. 2.6. As shown in Eq (2.11), once frequency deviation is detected, the primary power support would be determined according to the droop coefficient. Next, the active power variation for primary power control is sent to a PI controller, and then the PV side dc bus voltage variation is acquired. The voltage variation is limited by ΔU_f^{max} and ΔU_f^{min} (ΔU_f^{max} equals to $U_{mpp} + \Delta U_d - U_{oc}$, where U_{oc} is the open-circuit voltage, ΔU_f^{min} equals to $-\Delta U_d$). Plus the predefined voltage increase ΔU_d, the total voltage variation of PV side dc bus ΔU is finally determined. It is noted that a deloading threshold P_{min} is set in this chapter, which means only when that the solar power production is larger than this threshold, the deloading control would be activated. Or the output signal of the comparing step of solar power generation and the threshold is 0. The AND gate guarantees that the solar systems do not take part in the primary frequency control when the deloading threshold is not meet.

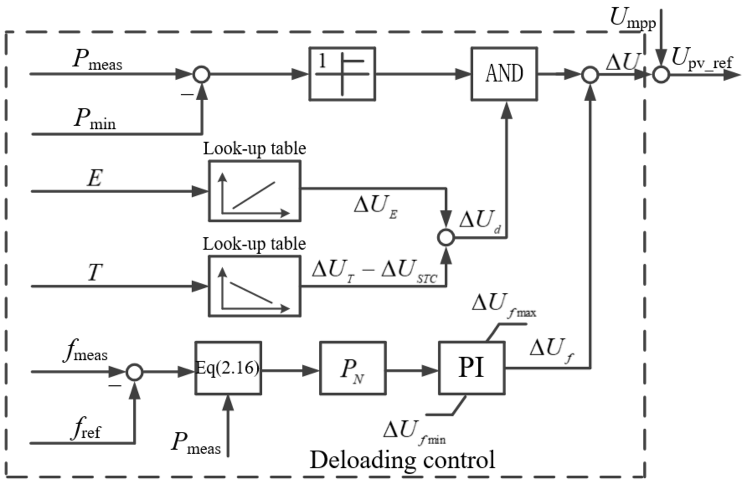

Fig. 2. 6 The proposed deloading control scheme.

2.3 Case Studies

2.3.1 Microgrid Model

A microgrid system is established in DIgSILENT/PowerFactory to test the performance of the proposed control strategy, as given in Fig. 2.7. Six PV generators and a diesel generator are comprised in microgrid, whose parameters can be found in the appendix. There are no ESSs involved in this system to better demonstrate the contribution PV systems provide in frequency regulation. Load 1 is a constant load with $P_{L1} + Q_{L1} = 3MW + 0.3MVAR$, and load 2 is a dump load with $P_{L2} + Q_{L2} = 0.35MW + 0.03MVAR$.

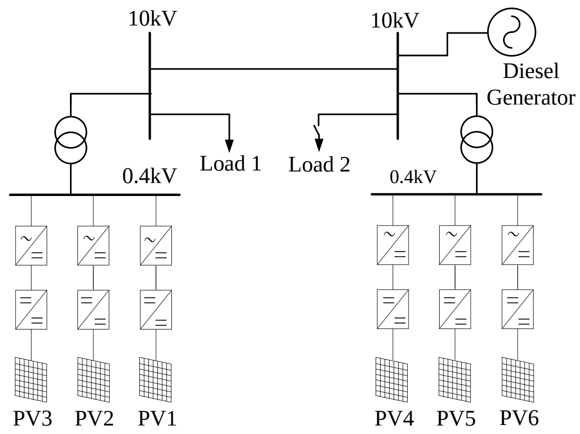

Fig. 2. 7 The test system.

The main frequency regulation responsibility is undertaken by the diesel generator in the studied isolated microgrid. It contributes system inertia as its rotational rotor is directly coupled with system frequency. In addition, it participates in primary frequency control with the droop parameter is set as 4%.

The PV system operates at a deloading mode under normal conditions. The deloading level is directly related with the solar energy harvest and the primary frequency regulation contribution of solar systems. Broadly speaking, a larger value inevitably brings about less solar energy harvesting and a smaller value leads to less contribution to frequency regulation. Recently, some works have been focused on wind energy conversation systems joining in primary frequency regulation, in which the deloading coefficient usually varies between 5% and 10%. In fact, the setting of deloading coefficient can be determined according to possible disturbances, solar penetration and system reserve capacity. Because the high penetration of solar power penetration in the studied system, the deloading coefficient is predefined as 10% in this thesis. In addition, the threshold of the deloading control is set as 20%. That is, the deloading control only activates in the situation when solar power production is larger than its 20% rated capacity. Many grid codes require that the droop parameter should be set between 2%-6%. In this thesis, the droop parameter $R_{\min}$ is set as 4% under STC to obtain a satisfied primary frequency regulation performance. And then $R_{\max}$ is set as 20% according to Eq. (2.16).

2.3.2 Simulation Results

Extensive case studies are considered herein to test the performance of the proposed control strategy. Firstly, the proposed DC-link voltage control is verified, it is conducted in the situation that PV systems operate at MPPT mode. Then several control strategies (i.e. the individual DC-link voltage control, the individual primary frequency control and the simultaneous control) are compared in the constant working condition. Finally, time varying irradiance and temperature conditions are considered to investigate the impact of different working conditions on the performance of the simultaneous control.

2.3.2.1 DC-link Voltage Control under STC with MPPT

The dump load 2 is connected to system at 15s. Fig. 2.8 exhibits the system frequency response, the output solar power and DC-link voltage after the DC-link voltage control is introduced. From Fig. 2.8(a), it can be found that the frequency nadir increases from 49.292Hz to 49.335Hz with the DC-link voltage control while the quasi-steady state frequency remains at 49.810Hz. This is because DC-link voltage control can only provide a rapid yet temporary active power support. As shown in Fig. 2.8(b), when load sudden increase event occurs, after the power surge provided by the discharge of DC-link capacitor, solar power production demonstrates a slight decrease that lasts for several seconds during the DC-link voltage recovery period. Fig. 2.8(c) shows that with the MPPT control, DC-link voltage remains at 1p.u. throughout transit event. By comparison, DC-link voltage decreases in its discharging period when the frequency deviation is introduced.

Since the capacitor capacity is limited, the inertial response it provides is not significant. Fig. 2.8 also gives the example when DC-link capacitance C_{dc} increased to 90000 μF . It can be seen that, with C_{dc}=90000 μF , the dynamic frequency deviation, which is denoted as the difference between frequency nadir/peak and the nominal frequency, decreases by 98mHz, and the RoCoF is also reduced more significantly, as a larger C_{dc} facilitates more power transformation from the capacitor. It is known that a large dynamic frequency deviation or RoCoF would trigger the action of protection relay and the load shedding scheme. With the proposed DC-link voltage control, such problems could be avoided. So as a conclusion, it can be said that an appropriate increase of C_{dc} has a positive impact on system stable operation.

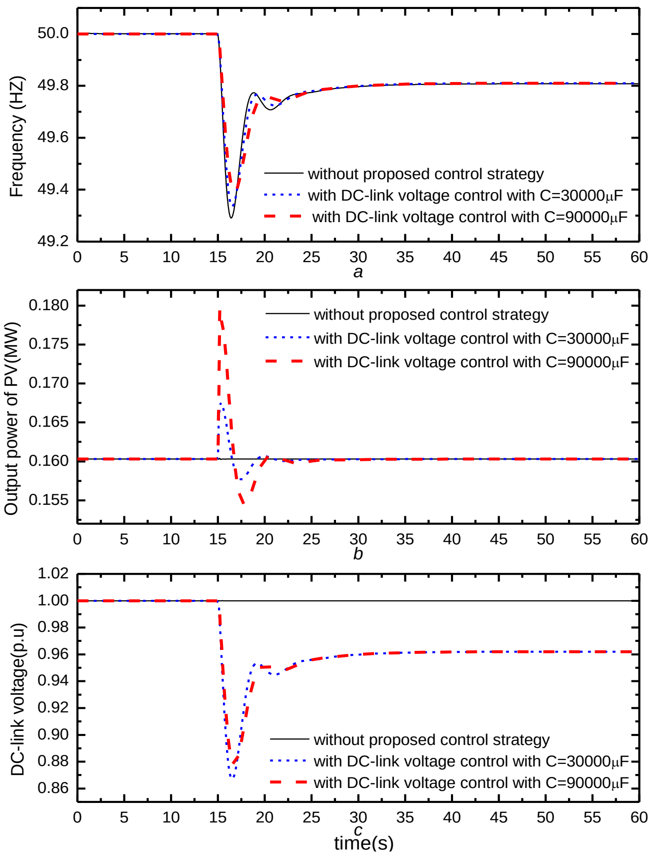

Fig. 2. 8 Simulation results of DC-link voltage control when load increases (a) System frequency, (b) Output power of a PV generator, (c) DC-link voltage

2.3.2.2 Various Frequency Control Strategies Under STC with Deloading

To test the performance of DC-link voltage control, primary frequency control, and simultaneous control, simulations are conducted with load 2 is assumed to connect to system at 15s under STC. The profiles of system frequency, the output solar power and DC-link voltage are given in Fig. 2.9. Solar systems operate at the deloading mode initially, and the deloading level is set as 10%, the droop parameter is set as 4%. Fig. 2.9(a) indicates that the inertial response provided by the DC-link capacitor is not relevant to whether deloading control is applied. Hence the dynamic frequency behavior is the same with previous MPPT mode. Once the primary frequency control is applied, frequency nadir increases from 49.292Hz to 49.472Hz and the quasi-steady state frequency rises from 49.810Hz to 49.857Hz. When the simultaneous control is adopted, the improvement of frequency behavior is the most significant (i.e. frequency nadir is 49.505Hz and the quasi-steady state frequency is 49.857Hz). It can be clearly seen from Fig. 2.9(b) that merits of the DC-link voltage control and the primary frequency control are integrated. Fig. 2.9(c) indicates DC-link voltage variation is mitigated when the simultaneous control is applied as the frequency behavior becomes better.

The dump load 2 is disconnected from system at 15s. The frequency behavior when the DC-link voltage control, the primary frequency control and simultaneous control is applied respectively is shown in Fig. 2.9(d). It can be found that frequency peak decreases from 50.705Hz to 50.654Hz, and quasi-steady state frequency maintains at 50.194Hz with the utilization of DC-link voltage control. Once the primary frequency control is activated, system frequency remains at 50Hz through simulation period, since the output solar power has a large curtail margin. Similarly, when simultaneous control is applied, system frequency maintains at the nominal value.

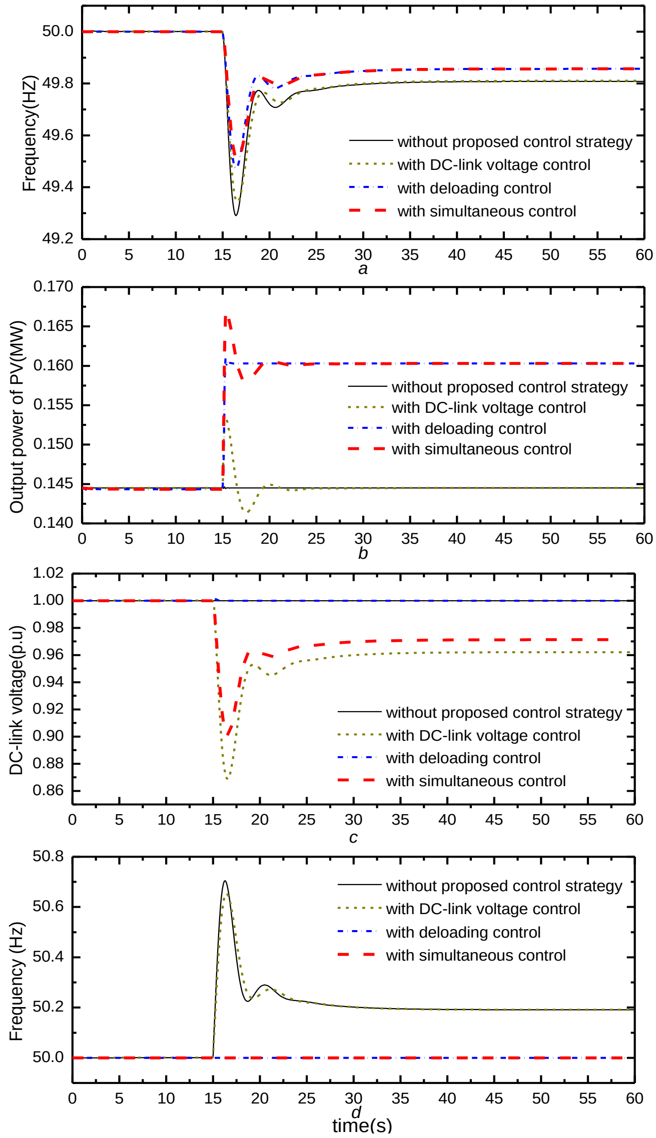

Fig. 2. 9 Simulation results of different control strategies under STC
(a) System frequency when load increases, (b) Output power of a PV generator when load increases, (c) System frequency when load decreases, (d) Output power of a PV generator when load decreases

2.3.2.3 Various Frequency Control Strategies Under Non-STC with Deloading

Fig. 2.10 exhibits frequency behavior under the condition that irradiance is 300W/m^2 and temperature is 15^0C for the same load disturbance with that in Fig. 2.9. Since the power production is low at such an environment condition and the reserve capacity of solar system is correspondingly low, the droop parameter is calculated as 15% according to Eq (2.16). When load sudden increase event occurs, as shown in Fig. 2.10(a), the frequency behavior is identical to the situation under STC. While once primary frequency control is activated, frequency nadir increases from 49.292Hz to 49.345HZ and the quasi-steady state frequency increases from 49.808Hz to 48.810Hz. It can be found that improvement of frequency response is less significant than STC due to the low reserve capacity. When the simultaneous control is utilized, the frequency nadir rises to 49.505Hz. A 0.35-MW load sudden decrease event is assumed to occur at 15s, as shown in Fig. 2.10(b), the frequency behavior is also identical to the STC scenario with the implementation of DC-link voltage control. When the primary frequency control is activated, frequency peak decreases from 50.705Hz to 50.398Hz and the quasi-steady state frequency decreases from 50.194Hz to 50.105Hz. It can be found that the frequency improvement is also less significant than that under STC. This is because the solar power production is low and the enhancing deloading capability is correspondingly low. The simultaneous control leads to the best frequency response with the frequency peak is reduced to 59.37Hz.

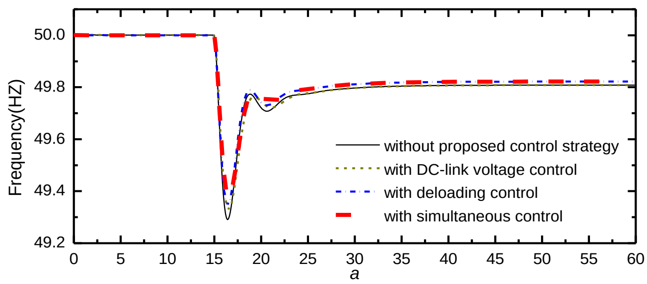

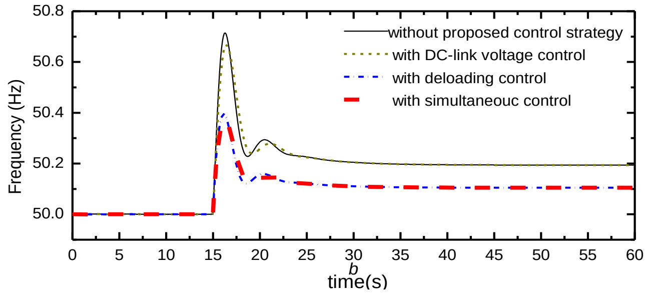

Fig. 2. 10 Simulation results of different control strategies under non-STC (a) System frequency when load increases, (b) System frequency when load decreases

2.3.2.4 Variable Droop Based Simultaneous Frequency Control Under Time Varying Working Conditions

To test feasibility of the simultaneous frequency control strategy under actual working conditions, the time varying irradiance and ambient temperature are considered in this section. Fig. 2.11(a) exhibits a set of measured irradiance and temperature data from a practical PV power plant, which is utilized as the input in our studied solar system. The dump load 2 is connected to system at 620s. The system dynamic operation behavior when PV systems operate at MPPT mode and when the simultaneous frequency control is applied is compared through dynamic simulation. Fig. 2.11(b-g) presents the system frequency behavior, solar output power, diesel output power, droop control gain K_d (the reciprocal of droop parameter, 1/R), PV array voltage and DC-link voltage. Fig. 2.11(b) demonstrates frequency fluctuates with fluctuation of solar power. While with the implementation of the simultaneous control, frequency nearly maintains at 50Hz before the sudden load increase event. This is because frequency peaks and valleys are effectively compensated by the energy stored in the DC-link capacitor and the reserved primary control power. The DC-link voltage control and primary frequency control both have a fast response speed, and therefore the frequency regulation burden of the diesel generator is effectively mitigated. Accordingly, the output power of the diesel generator is almost unchanged throughout simulation, as shown in Fig. 2.11(d). The value of the droop control gain is shown in Fig. 2.11(e), it can be found that that an appropriate control gain can be adaptively adjusted according to the reserve capacity of PV systems. According to Fig. 2.11(f), it can be verified that the deloading can be achieved via change of PV array voltage. It can be seen from Fig. 2.11(g) that the variation of DC-link voltage only becomes significant in the situation that frequency deviation is severe. When the load increase disturbance occurs at 620s, frequency nadir rises from 49.317Hz to 49.496Hz with the simultaneous control via DC-link capacitor discharging and releasing of primary control reserve. Consequently, it can be draw a conclusion that the implementation of simultaneous control is effective under time varying irradiance and temperature situation.

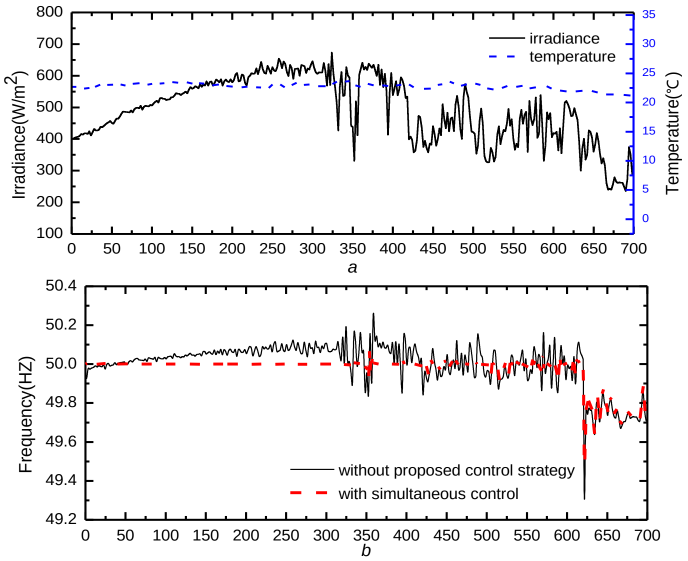

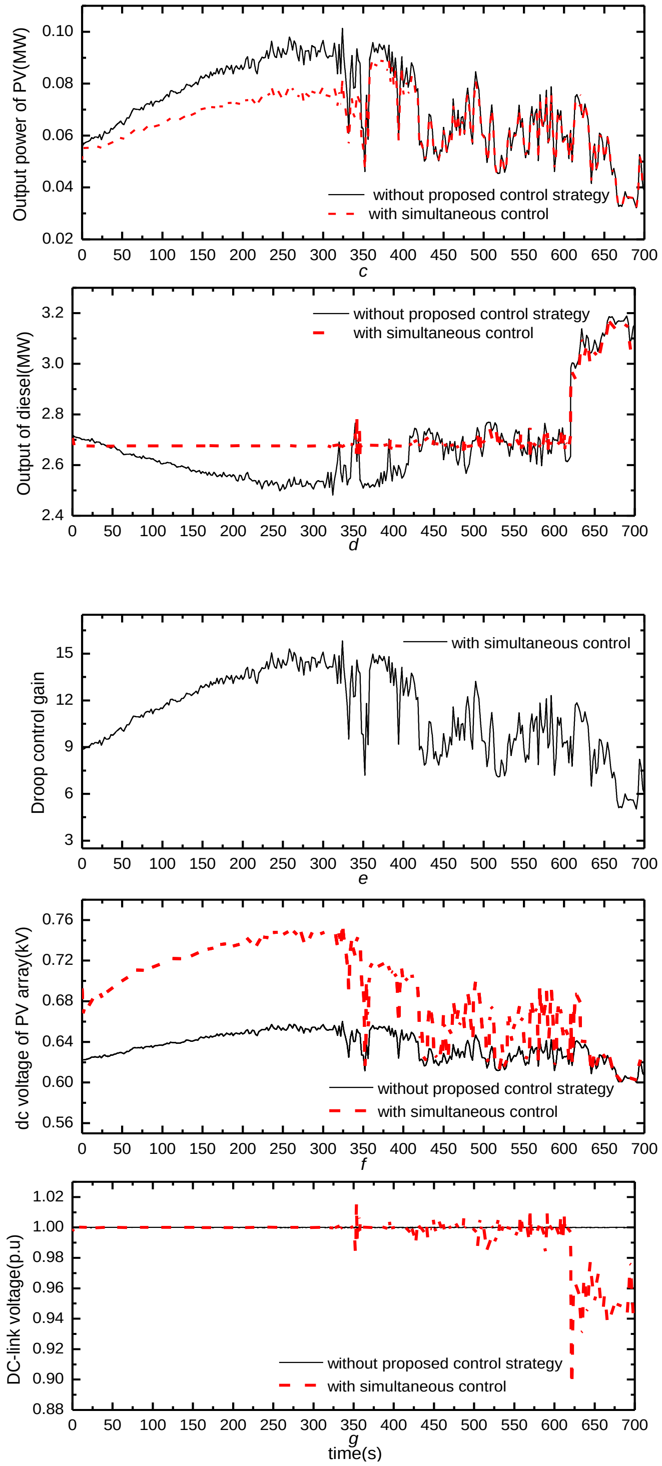

Fig. 2. 11 Simulation results of simultaneous control under time varying irradiance and temperature condition
(a) Varying irradiance and temperature, (b) System frequency, (c) Output power of a PV generator, (d) Output power of diesel generator, (e) Droop control gain, (f) dc voltage of PV array, (g) DC-link voltage

2.4 Summary

In this chapter, a novel control strategy is proposed for the two-stage three phase PV system participating in frequency regulation considering changing operation conditions. Specifically, the DC-link voltage control is developed to mimic the inertia characteristic via utilizing the energy stored in the DC-link capacitor. In addition, PV systems operate at a deloading mode under normal operation to offer power reserve and the designed droop control enables PV systems to provide primary frequency regulation support. Considering the uncertainty characteristic of solar power production, the droop parameter is adaptively adjusted according to the primary reserve capacity. To assess the effectiveness of the proposed simultaneous control, simulations under various operation conditions are considered. Simulation results demonstrate that the proposed simultaneous control combines the merits of DC-link voltage control and primary frequency control and can effectively mitigate system frequency fluctuations. This will significantly mitigate the burden on conventional generators and help to stabilize system frequency of future grids with low inertia.

Chapter 3 Coordinated Control Strategies of PMSG-based Wind Turbine for Active Power Regulation

Nomenclature

P_m	Mechanical power captured from wind by the WT
ρ	Air density
R	Rotor blade radius
v_w	Wind speed
C_p	Power coefficient
λ	Tip speed ratio
β	Pitch angle
ω	Rotor speed
H_{wt}	Inertia of wind rotor mass
H_{g}	Inertia of wind turbine generator
T_m	Turbine mechanical torque
T_{shaft}	Mechanical torque of the shaft
T_e	Electrical torque of the wind turbine generator
θ_s	Shaft twist angle
ω_g	Generator speed
C_{dc}	Capacitance of DC-link capacitor
U_{dc}	DC-link voltage
P_{grid}	Power delivered to grid
P_{s}	Power provided by the stator of PMSG
P_{com}	Dispatch command
P_{mpp}	Active power reference generated according to the MPPT curve
ω_{nom}	Nominal rotational speed

J	Wind turbine equivalent inertia
ΔP	Power deviation between the dispatch command and the wind power generation
$\Delta P_C(t)$	Charging/discharging power from DC-link capacitor
ΔP_1	Power regulation task allocated to DC-link voltage control
ΔP_R	Charging/discharging power from KE
ΔP_2	Power regulation task allocated to rotor speed control
ΔP_3	Power regulation task allocated to pitch angle control
ω_{opt}	Rotor speed at MPP status

The potential of the solar system itself for frequency regulation is adequately exploited in Chapter 2. To delve into the greatest potential of the PMSG-based WT for active power regulation, all existing resources within WT system are utilized in this Chapter. Two control schemes are proposed to coordinate these resources to follow the dispatch order.

This chapter is organized as follows. The modeling of PMSG-based wind turbine is illustrated in Section 3.1. The simultaneous control scheme for active power regulation is developed in Section 3.2. The hierarchical control scheme is proposed in Section 3.3. Case studies and simulation results are discussed in Section 3.4. Finally, the summary is given in Section 3.5.

3.1 Modeling of PMSG-based Wind Turbine

The system configuration of PMSG-based WT is given in Fig. 3.1. The wind turbine is directly connected with the permanent magnet synchronous generator, which is further connected to grid through a full-capacity back-to-back converter. The operating principle of the back-to-back converter is to synchronize the current with variable amplitude along with the frequency of grid. The MPPT control is achieved in the generator side converter controller and the DC-link voltage is regulated in the grid side inverter controller.

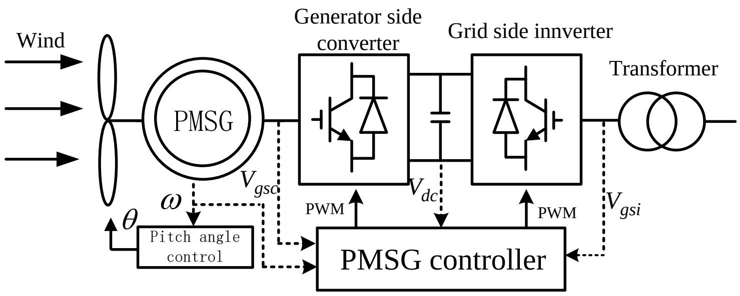

Fig. 3. 1 System configuration of a PMSG-based wind turbine

3.1.1 Wind Turbine Mechanical Model and Drive Train

The mechanical power P_m extracted from the wind is defined as,

$$P_m = \frac{\rho}{2}\pi R^2 {v_w}^3 C_p(\lambda, \beta) \tag{3.1}$$

where ρ is the air density, R is the rotor blade radius, v_w is the wind speed, λ is the tip speed ratio, β is the pitch angle, and C_p is the power coefficient. The power coefficient is a nonlinear function between tip speed ratio and pitch angle. As reported in [97], it can be formulated as,

$$C_p = 0.22(\frac{116}{\lambda_i} - 0.4\beta - 5)e^{-\frac{12.5}{\lambda_i}} \tag{3.2}$$

$$\frac{1}{\lambda_i} = \frac{1}{\lambda + 0.08\beta} - \frac{0.035}{\beta^3 + 1} \tag{3.3}$$

The tip speed ratio is defined as,

$$\lambda = \frac{\omega R}{v_w} \tag{3.4}$$

where ω is the rotor speed.

A two-mass shaft model is built to represent the wind rotor mass that with a larger inertia H_{wt} and the generator with a smaller inertia H_g. Ignoring the damping and loss, the drive train coupling of the wind turbine can be described as,

$$H_{wt}\frac{d\omega}{dt} = T_m - T_{shaft} \tag{3.5}$$

$$\frac{d\theta_s}{dt} = \omega - \omega_g \tag{3.6}$$

$$H_g\frac{d\omega_g}{dt} = T_{shaft} - T_e \tag{3.7}$$

where T_m is the turbine mechanical torque, T_{shaft} and T_e are the mechanical torque of the shaft and electrical torque of the generator, θ_s is the shaft twist angle, ω_g is the generator speed. The turbine mechanical torque is defined as,

$$T_m = \frac{P_m}{\omega} \tag{3.8}$$

3.1.2 Rotor Speed Control and Pitch Angle Control

The PMSG-based wind energy conversion system allows operation at variable speed. At a certain pitch angle, the relationship between power coefficient and rotor speed can be shown in Fig. 3.2. It can be found that there exists a unique rotor speed that corresponds to the maximum power coefficient. The maximum power tracking is achieved by the rotor speed control and the pitch angle control, whose control principle is shown in the upper part and the lower part of Fig. 3.3 respectively. The rotor speed control utilizes the active power generated via the maximum power point tracking curve once the rotor speed is measured as the control reference. And then the active power reference is delivered to the generator side converter control. The lower part shows the pitch angle control. It activates to avoid over-speeding once rotor speed reaches to its upper limit.

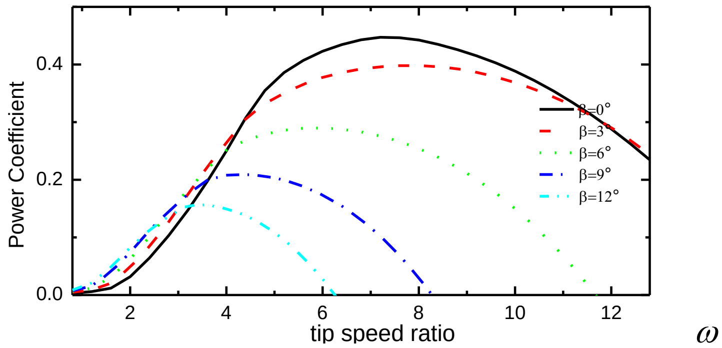

Fig. 3. 2 The $C_p - \lambda$ characteristics

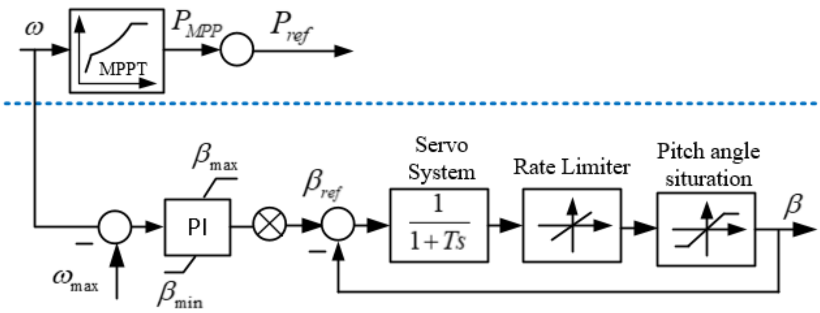

Fig. 3. 3 Rotor speed control and pitch angle control of PMSG-based WTs

3.1.3 Generator Side Converter Control

The active and reactive power control is decoupled by the current control of the generator side converter. The current control works in a voltage-oriented reference frame. The cascaded control structure with the outer power control loop and inner current loop is shown in Fig. 3.4, where P_{meas} and Q_{meas} are the measured active power and reactive power of generator side converter. i_{dsref},

i_{qsref}, u_{dsref}, u_{qsref} are the reference values for d-axis stator current, q-axis stator current, d-axis stator voltage, q-axis stator voltage, respectively. ψ_{ds} is d-axis flux linkage and ψ_{qs} is the q-axis flux linkage. The main purpose the generator side controller is to regulate the power output to achieve the maximum wind power tracking. To this end, the active power reference P_{ref} is set according to the MPPT curve. The reactive power reference Q_{ref} is set to zero to ensure the maximum energy yield. The d-axis rotor current is calculated according to the active power reference, while the q-axis rotor current is calculated according to the reactive power reference. The required d-q components of voltage vectors are obtained from two PI controllers, and the coupling is eliminated via the fed-forward compensation.

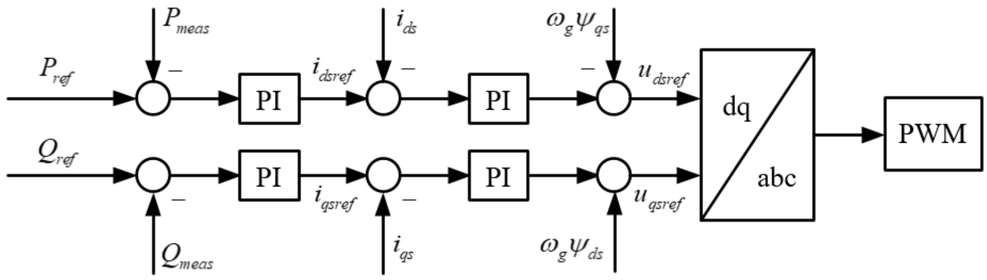

Fig. 3. 4 Generator-side Converter Control

3.1.4 Grid Side Converter Control

Fig. 3.5 depicts the control diagram of grid-side converter, where U_{dcref} is the DC-link voltage reference, U_{dc} is the measured actual voltage of DC-link. i_{dgref}, i_{qgref}, i_{dg}, i_{qg} are the reference value and actual value of d-axis and q-axis current of grid respectively, ω_e is the grid angular frequency, L_d is the d-axis inductance of filter and L_q is the q-axis inductance of filter, U_d is the d-axis of point of common coupling voltage. The main control purpose of the grid side converter is to achieve the stabilization of DC-link voltage and to control the reactive power delivered to grid. The q-axis current is set to zero to ensure the WT to operate at the unity power factor mode.

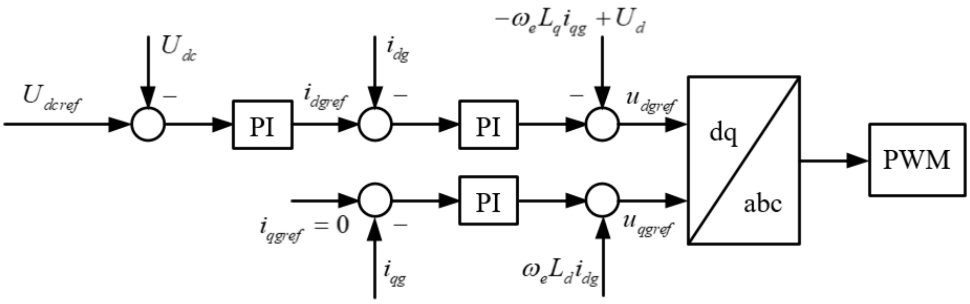

Fig. 3. 5 Grid-side Converter Control

3.1.5 DC-link Voltage Control

The DC-link capacitor is an energy storage device. Its voltage is determined by the power injected into the generator side converter and the power transmitted to the grid side inverter. Their relationship can be expressed as,

$$C_{dc} U_{dc} \frac{dU_{dc}}{dt} = P_{grid} - P_s \tag{3.9}$$

where C_{dc} is the capacitance, P_{grid} is the power delivered to grid and P_s is the power provided by the stator current of PMSG.

3.2 Simultaneous Control Strategy for Active Power Regulation

The DC-link voltage control, rotor speed control, and pitch angle control are individually proposed in this section. Once the dispatch command is introduced into each individual controller, they are able to provide active power regulation service simultaneously.

3.2.1 DC-link Voltage Control

As mentioned before, the DC-link capacitor is an energy storage device. It can provide extra active power support as long as the DC-link voltage is allowed to vary within a small range. According to [98], the variable region of DC-link voltage depends on insulation requirements, current ratings and PWM functionality. In this chapter, the DC-link voltage variation is subject to ±0.14p.u. to avoid excessive voltage fluctuation. It is worth noting that such settings can be adjusted flexibly according to the power electronic devices' intrinsic characteristic. Once the voltage variation is determined, the DC-link capacitor can offer extra active power support in its discharging/charging period. To trace the dispatch command P_{com}, the reference of power delivered to grid P_{grid} can be replaced by P_{com}. In this context, a modified DC-link voltage equation can be rewritten as,

$$C_{dc}U_{dc}\frac{dU_{dc}}{dt} = P_s - P_{com} \tag{3.10}$$

The energy stored/released during the capacitor discharging/charging process could be expressed by integrating Eq (3.10) over time,

$$\int_{t_0}^{t_1} C_{dc}U_{dc}dU_{dc} = \int_{t_0}^{t_1}(P_s - P_{com})dt \tag{3.11}$$

$$\frac{1}{2}C_{dc}(U_{dc1}{}^2\text{-}U_{dc0}{}^2) = \int_{t_0}^{t_1}(P_s - P_{com})dt \tag{3.12}$$

where U_{dc0} and U_{dc1} denote the DC-link voltage at time t_0 and t_1, respectively. U_{dc1} can be expressed in terms of voltage deviation ΔU_{dc}, substituting $U_{dc1} = U_{dc0} + \Delta U_{dc}$ into Eq (3.12), one can obtain,

$$\frac{1}{2}C_{dc}[(U_{dc0}+\Delta U_{dc})^2-U_{dc0}{}^2]=\int_{t_0}^{t_1}(P_s-P_{com})dt \tag{3.13}$$

$$\frac{1}{2}C_{dc}[2U_{dc0}\Delta U_{dc}+\Delta U_{dc}{}^2]=\int_{t_0}^{t_1}(P_s-P_{com})dt \tag{3.14}$$

As mentioned before, ΔU_{dc} is set within ±0.14 p.u.. Therefore, ΔU_{dc}^2 in Eq (3.14) can be neglected. Thus, the DC-link voltage reference U_{dc1} at time t_1 can be expressed as,

$$U_{dc1}=U_{dc0}+\frac{\int_{t_0}^{t_1}(P_s-P_{com})dt}{C_{dc}U_{dc0}} \tag{3.15}$$

Based on the above analysis, a novel DC-link voltage control scheme is designed as given in Fig. 3.6 and it should be introduced to the grid side inverter controller. The working principle of the proposed control scheme is to establish the relationship between the regulation command and the DC-link voltage reference. A sample and hold routine is imported to "remember" the DC-link voltage at the previous moment and to ensure the continuous calculation of the subsequent reference value. The energy released/absorbed during the charging/discharging process from time t_0 to t_1 can be obtained according to the introduced sample and hold routine and register routine. After getting the required information, the DC-link voltage reference can be calculated via Eq (3.15).

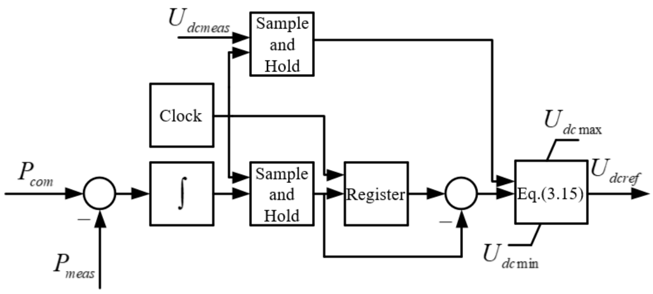

Fig. 3. 6 Control scheme of the proposed DC-link voltage control

3.2.2 Rotor Speed Control

The rotor motion equation is used to describe the rotor speed dynamics, which is described as follows,

$$2H\omega\frac{d\omega}{dt} = P_s - P_{mpp} \tag{3.16}$$

where P_{mpp} denotes the active power reference obtained from the MPPT curve, H denotes the wind turbine inertia constant, and it can be defined as,

$$H = \frac{J\omega_{nom}{}^2}{2P_N} \tag{3.17}$$

where ω_{nom} is the nominal rotational speed, J is the wind turbine equivalent inertia, which can be calculated as,

$$J = J_{tur} + J_{gen} \tag{3.18}$$

where J_{tur} is the turbine inertia and J_{gen} is the generator inertia.

Utilizing the energy stored in the rotating rotor to provide active power support is the core idea of rotor speed control. In fact, the active power reference of the WT can be changed to a new value quickly. Therefore, the active power reference can be replaced by the regulation command other than the MPPT curve. Rewritten Eq. (3.16), a modified rotor motion equation can be obtained as,

$$2H\omega\frac{d\omega}{dt} = P_m - P_{com} \tag{3.19}$$

By integrating Eq (3.19) over time from t_0 to t_1, one can obtain,

$$2\int_{t_0}^{t_1} H\omega d\omega = \int_{t_0}^{t_1} (P_m - P_{com})dt \tag{3.20}$$

$$H(\omega_1^2 - \omega_0^2) = \int_{t_0}^{t_1} (P_m - P_{com})dt \tag{3.21}$$

where ω_0 and ω_1 denote the rotor speed at time t_0 and t_1, respectively. ω_1 is defined as $\omega_1 = \omega_0 + \Delta\omega$, where $\Delta\omega$ is the rotor speed variation. Substituting the above equation into Eq (3.21), it becomes,

$$H[(\omega_0 + \Delta\omega)^2 - \omega_0^2] = \int_{t_0}^{t_1} (P_m - P_{com})dt \tag{3.22}$$

$$H[2\omega_0\Delta\omega + \Delta\omega^2] = \int_{t_0}^{t_1} (P_m - P_{com})dt \tag{3.23}$$

Similarly, $\Delta\omega^2$ can be ignored for a short period of time. Hence, ω_1 can be calculated as follows based on Eq (3.23):

$$\omega_1 = \omega_0 + \frac{\int_{t_0}^{t_1} (P_{wt} - P_{com})dt}{2H\omega_0} \tag{3.24}$$

Based on the above analysis, a new rotor speed control strategy is developed and introduced to the generator side inverter controller, as given in Fig. 3.7. For the sake of providing active power regulation support, the relationship between the regulation command and the rotor speed variation should be established as Eq (3.24) shows. A sample and hold routine and a register routine are introduced to "remember" the rotor speed at the previous and current moments. The upper and lower limits of rotor speed are typically determined by the manufacturer. In this chapter, the upper limit $\omega_{\max}$ is predefined as 1.22p.u. and the lower limit $\omega_{\min}$ is predefined as 0.7p.u.

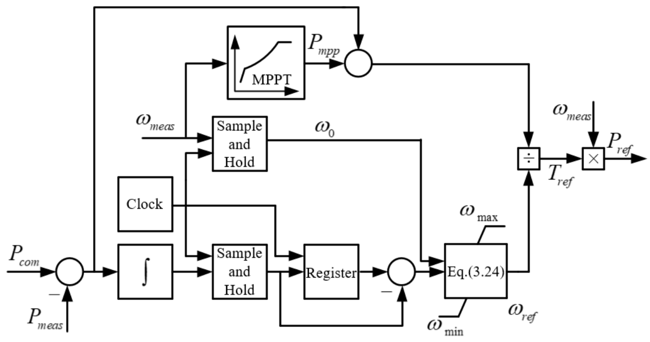

Fig. 3. 7 Control scheme of the proposed rotor speed control

3.2.3 Pitch Angle Control

To curtail mechanical power wind turbine captured from wind when the regulation command is lower than actual wind power output, the regulation command can be introduced into the pitch angle controller to guide and determine a new pitch angle reference. The developed pitch angle control scheme is given in Fig. 3.8. It can be found that the deviation between the captured wind power P_m and the regulation command P_{com} is sent to a PI controller. After that, the new reference value of blade pitch angle is generated.

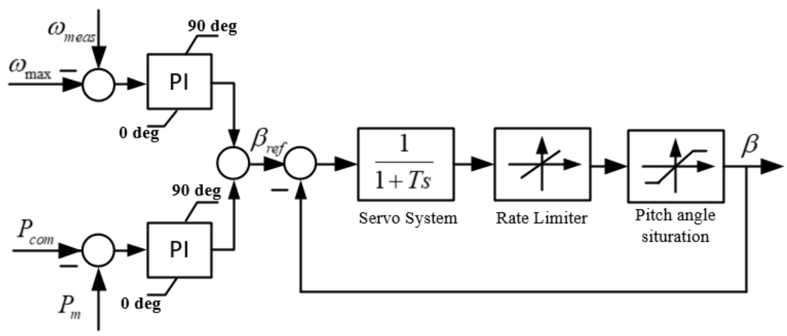

Fig. 3. 8 Control scheme of the proposed pitch angle control

3.2.4 Further Discussion of Simultaneous Control

The identical control reference (i.e. regulation command) is fed into all individual controllers concurrently under the simultaneous control scheme. Accordingly, there are three parts involved in the active power regulation support provided by the WT, which can be expressed as,

$$P_{\text{support}} = P_{dc} + P_{rotor} + P_{pitch} = CU_{dc}\frac{dU_{dc}}{dt} + 2H\omega\frac{d\omega}{dt} + \frac{\rho\pi R^2}{2}\left(C_p^{'} - C_p\right)v_w^3 \quad (3.25)$$

where $C_p^{'}$ is the new power coefficient when pitch angle control is activated.

It can be found from Eq (3.25) that the existing resources of WT are adequately exploited via the simultaneous control. Hence it is easy to understand that the simultaneous control has a larger power regulation capability than individual control does.

3.3 Hierarchical Control Strategy for Active Power Regulation

Although all the existing resources are utilized in the simultaneous control, it is not a cost-efficient strategy as no cooperation exists among these three individual resources. Because the frequent manipulation of blade pitch angle would increase the WT mechanical fatigue and reduce the utilization efficiency of DC-link capacitor and KE storage.

In order to solve the above problems, a hierarchical control scheme is proposed to coordinate the three regulation resources. The procedure of the hierarchical control can be illustrated in the following steps: 1) The three individual regulation resources response to the regulation command per a predefined list. Such list specifies the response priority of the regulation resources. The activation priority is designed to be: i) DC-link voltage control, ii) rotor speed control, and iii) pitch angle control.; 2) The power regulation capability of each resource is evaluated in real time such that they can individually or collectively operate in an effective manner governed by an intelligent rule-based algorithm. In this context, the active power regulation potential of individual resource can be fully exploited under time-varying working conditions.

3.3.1 Regulation Task Allocated to DC-link Voltage Control

The regulation capability of DC-link capacitor lies on the available energy in it. The evaluation of its active power regulation capability is illustrated in the following.

Definition 1: According to the above-mentioned DC-link voltage equation, the available active power support at time instance *t* transformed from DC-link capacitor charging/discharging process can be expressed as,

$$\Delta P_C(t) = \begin{cases} \min[\dfrac{U_{dc}^2(t) - U_{dc\max}^2}{2\Delta t}, \dfrac{U_{dc}^2(t) - U_{dc}^2(t_0)}{2\Delta t}], \Delta P < 0 \\ \max[\dfrac{U_{dc}^2(t) - U_{dc}^2(t_0)}{2\Delta t}, \dfrac{U_{dc}^2(t) - U_{dc\min}^2}{2\Delta t}], \Delta P > 0 \end{cases} \tag{3.26}$$

where $U_{dc}(t)$ and $U_{dc}(t_0)$ are the DC-link voltage at time instance *t* and time t_0, ΔP is the deviation between the regulation command and actual power generation, Δt is the dispatch cycle. Eq. (3.26) ensures that the active power support provided by DC-link capacitor is within its charging/discharging range.

Since the DC-link capacitor has the highest response priority, the control variable $\Delta P_1(t)$ fed into DC-link voltage controller is given as follows,

$$\Delta P_1(t) = \begin{cases} \Delta P, & |\Delta P| \le |\Delta P_c(t)| \\ \Delta P_c(t), & |\Delta P| > |\Delta P_c(t)| \end{cases} \tag{3.27}$$

Eq (3.27) indicates that when the power deviation ΔP is within the regulation ability of DC-link capacitor, $\Delta P_1(t)$ is directly assigned as its power regulation task ΔP . Otherwise, $\Delta P_1(t)$ is assigned according to its maximum regulation capability at the time instance *t*. Eq. (3.27) ensures that the energy storage capability of the DC-link capacitor can be adequately utilized.

3.3.2 Regulation Task Allocated to Rotor Speed Control

Similar to DC-link voltage control, the power regulation capability of rotor speed control counts on the releasable/absorbable energy in the rotational rotor. Its active power regulation capability is evaluated in the following.

Definition 2: According to the above-mentioned rotor motion equation and the mechanical power capture equation of WT, the available active power support at time instance *t* transformed from the KE charging/discharging process is expressed as,

$$\Delta P_R(t) = \begin{cases} \min[P_m(t,\omega_{\max}) - P_m(t_0) + \dfrac{\omega^2(t) - \omega_{\max}^2}{2\Delta t}, \\ P_m(\omega(t)) - P_m(t_0) + \dfrac{\omega^2(t) - \omega_{\max}^2}{2\Delta t}], \Delta P < 0 \\ \max[P_m(\omega(t)) - P_m(t_0) + \dfrac{\omega^2(t) - \omega_{opt}^2(t)}{2\Delta t}, \\ P_m(\omega_{opt}(t)) - P_m(t_0) + \dfrac{\omega^2(t) - \omega_{\text{opt}}^2(t)}{2\Delta t}], \Delta P > 0 \end{cases} \tag{3.28}$$

where $P_m(t,\omega_{\max})$ is the mechanical power captured by WT at instant time *t* with the rotor speed accelerated to the upper limit, $P_m(t_0)$ is the mechanical power captured by WT at time t_0, $P_m(\omega_{opt}(t))$ is the mechanical power captured by WT at instant time *t* with the rotor speed at MPP statues. $\omega(t)$ is the rotor speed at time instance t, $\omega_{opt}(t)$ is the rotor speed at MPP status at time instance t. The reason why set ω_{opt} is to avoid excessive rotor speed deceleration, which may cause WT trip off. Eq. (3.28) guarantees that the active support provided by rotational rotor is within its charging/discharging range.

Since the rotational rotor has the second response priority, the control variable $\Delta P_2(t)$ fed into rotor speed controller can be calculated as follows,

$$\Delta P_2(t)=\begin{cases}0, \left|\Delta P\right| \le \left|\Delta P_C(t)\right| \\ \Delta P-\Delta P_C(t), \left|\Delta P_C(t)\right| < \left|\Delta P\right| \le \left|\Delta P_C(t)\right|+\left|\Delta P_R(t)\right| \\ \Delta P_R(t), \left|\Delta P\right| > \left|\Delta P_C(t)\right|+\left|\Delta P_R(t)\right|\end{cases} \tag{3.29}$$

Eq (3.29) guarantees that the rotor speed control only activates in the situation that ΔP exceeds the regulation ability of DC-link capacitor. And in the situation that the surplus power deviation is within the regulation capability of KE storage, the surplus power deviation is directly delivered into the rotor speed controller. On the contrary, $\Delta P_2(t)$ is assigned as its maximum regulation capability at the time instance t.

3.3.3 Regulation Task Allocated to Pitch Angle Control

To further compensate the active power regulation deficit, pitch angle control shall be activated, which however is at the lowest priority. Based on Eq (3.28) and Eq (3.29), the regulation task allocated to pitch angle control can be expressed as,

$$\Delta P_3(t)=\begin{cases}0, \Delta P \le \left|\Delta P_C(t)\right|+\left|\Delta P_R(t)\right| \\ \Delta P-\left|\Delta P_C(t)\right|-\left|\Delta P_R(t)\right|, \Delta P > \left|\Delta P_C(t)\right|+\left|\Delta P_R(t)\right|\end{cases} \tag{3.30}$$

Eq (3.30) ensures that the blade pitch angle would not activate in the situation when the DC-link capacitor and KE are not fully charged. Once their charging range is used up, the surplus power deviation will be tackled by pitch angle control.

Fig. 3.9 illustrates the proposed rule-based active power regulation allocation algorithm for the hierarchical control.

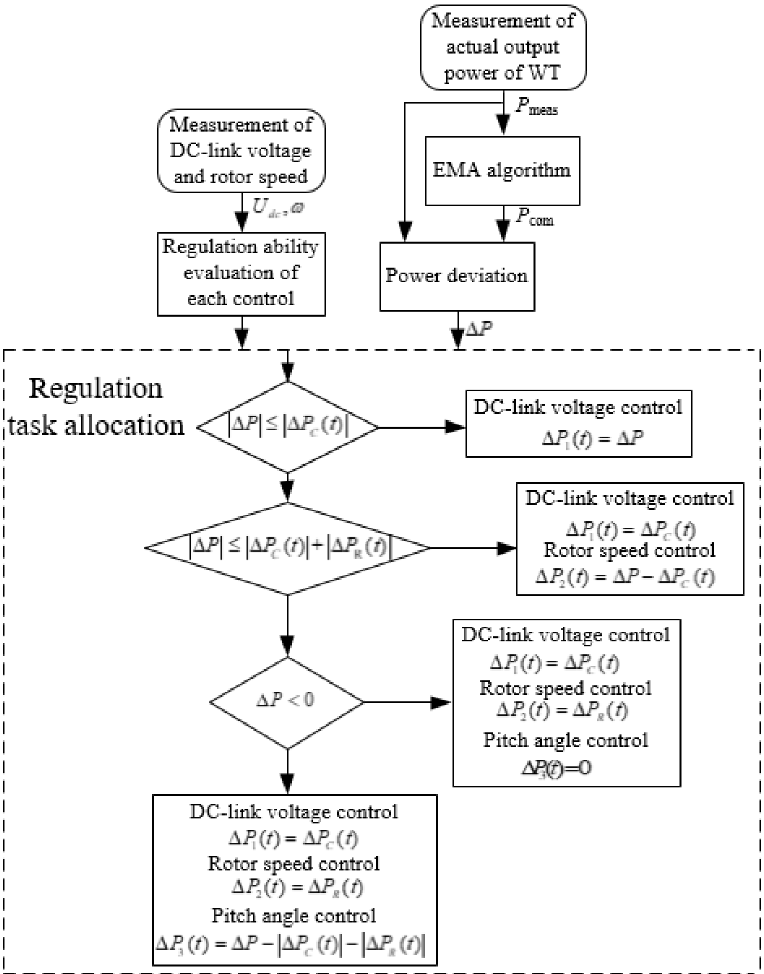

Fig. 3. 9 Flowchart of the proposed hierarchical control

3.3.4 Further Discussion of Hierarchical Control

Admittedly, all the existing resources in the WT are exploited in the hierarchical control to trace the regulation command. Theoretically, it can be well justified that the proposed regulation-task-allocation algorithm is better than the individual control strategy and the simultaneous control strategy. Firstly, it can be found that the well coordination of three individual resources is achieved by following the predefined response priority in the hierarchical control. As a result, the energy utilization efficiency is high throughout the wind power generation regulation process. In addition, other benefits can be gained including 1) over charging/discharging of DC-link capacitor is well avoided (refer to Eq(3.26)); 2) excessive acceleration/deceleration of rotor speed is refrained, which is bounded within $[\omega_{opt}, \omega_{max}]$ (refer to Eq(3.28)); 3) manipulation frequency of pitch angle control is reduced so as to mitigate operational wear; and 4) excessive energy can be readily stored in DC-link capacitor and WT rotating mass to enhance wind energy harvesting efficiency.

It is noted that the proposed hierarchical control can also be applied to the wind farm. At wind farm control level (without taking the wake effect into consideration), the regulation task can be allocated to each WT based on the predefined response priority of the three regulation resources and their corresponding regulation capability. Consequently, all WTs could operate in a distributed manner to enhance total wind energy harvesting and mitigate the mechanical stress of WTs while satisfying the regulation command.

3.4 Case Studies

3.4.1 Simulation Model and Parameter Setup

To test the performance of the proposed control strategies, a test system (as given in Fig. 3.10) including a synchronous generator (SG), a PMSG-based

WT, and a local power load are built up in the simulation platform DIgSILENT/PowerFactory. The nominal capacity of SG is 4.9MVA; the rated power factor is 0.8; and the droop parameter of its governor is set as 4%. For the PMSG-based WT, its rated capacity is 1.5MVA, and other parameters can be referred to Appendix. The load model is a fixed power model and is set as P_L+Q_L=3MW+0.2MVAR.

The exponential moving average (EMA) algorithm is adopted to generating the power regulation command of the WT. The regulation command can be generated as,

$$P_{com}(t)=[(P_{current}-P_{com}(t-1))\times k]+P_{com}(t-1) \tag{3.31}$$

where P_{com} is the regulation command calculated by EMA, $P_{current}$ is the real-time measured wind power output. k is the weighting factor. For the period-based EMA, the weighting factor k can be calculated as k=2/(N+1), where N is a specified number of periods. For practical application, N can be specified by the system operators. In this case studies, N is set to 80 per second as an example case to demonstrate the overall regulation performance of different control strategies, and k is equal to 2/(80+1).

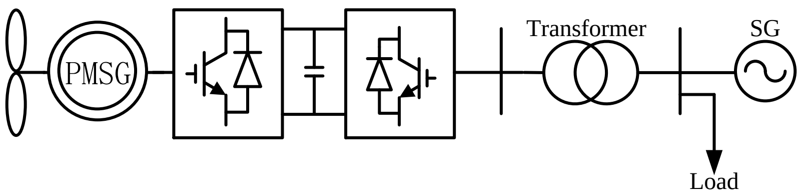

Fig. 3. 10 Diagram of the test system

3.4.2 Control Performance of Individual Strategy

Simulation results are given in this subsection to show the performance of individual DC-link voltage control, rotor speed control, and pitch angle control respectively. The time-varying wind speed used in simulation is shown in Fig. 3.11. The power regulation performance of the PMSG-WT with three individual control strategies as well as the behavior of the rotor speed, DC-link voltage and pitch angle are demonstrated as follows.

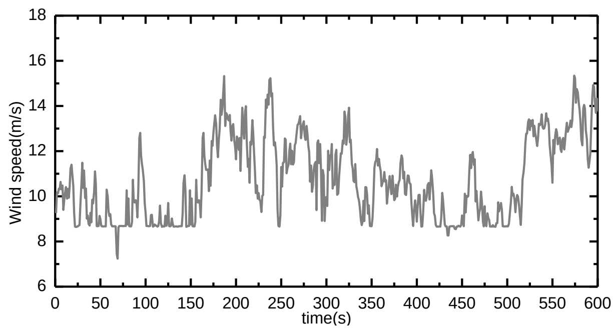

Fig. 3. 11 Wind speed time series used in case study

3.4.2.1 DC-link Voltage Control

The power regulation capability of DC-link capacitor is demonstrated via comparing the WT power generation profiles when the MPPT control is applied and the DC-link voltage control is applied respectively. As shown in Fig. 3.11(a), DC-link voltage control provides extra active power regulation support during its charging/discharging process. However, the regulation performance is non-significant due to the limited capacity of DC-link capacitor. Once the charging/discharging limit is reached, DC-link capacitor cannot track the regulation command anymore. Fig. 3.11(c) indicates that the DC-link voltage varies within the predefined range during the charging/discharging process. Since the mechanical power captured by the WT is not influence by the implementation of DC-link voltage control, the behavior of rotor speed and pitch angle is the same with MPPT control mode, as shown in Fig. 3.11(d, e).

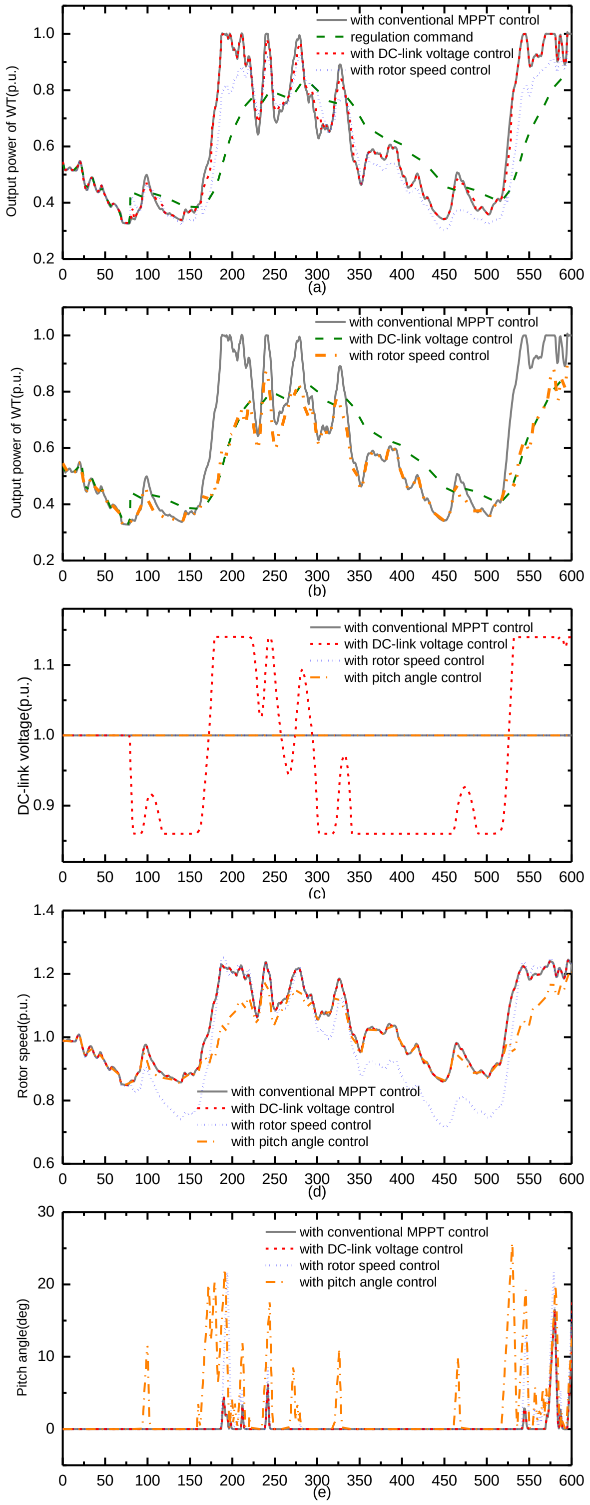
Output power of WT(p.u.)
with conventional MPPT control
regulation command
with DC-link voltage control
with rotor speed control
(a)
Output power of WT(p.u.)
with conventional MPPT control
with DC-link voltage control
with rotor speed control
(b)
DC-link voltage(p.u.)
with conventional MPPT control
with DC-link voltage control
with rotor speed control
with pitch angle control
(c)
Rotor speed(p.u.)
with conventional MPPT control
with DC-link voltage control
with rotor speed control
with pitch angle control
(d)
Pitch angle(deg)
with conventional MPPT control
with DC-link voltage control
with rotor speed control
with pitch angle control
(e)

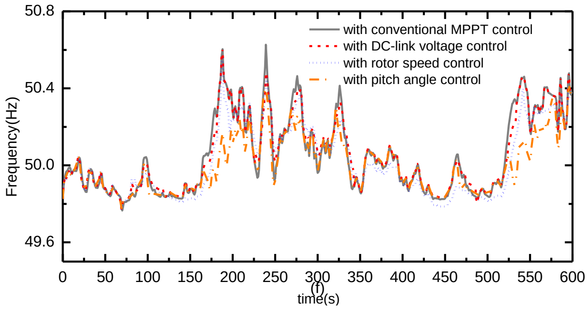

Fig. 3. 12 Simulation results for individual control strategy (a). Output power of PMSG-based WT, (b). Output power of PMSG-based WT, (c). DC-link voltage, (d). Rotor speed, (e). Pitch angle, (f) System frequency

3.4.2.2 Rotor Speed Control

Power production of PMSG-based WT once rotor speed control is implemented can be seen in Fig. 3.11(a). The rotor speed variation during power regulation period is given in Fig. 3.11(d). Visually, given the same regulation command, the regulation performance with the rotor speed control is better than with DC-link voltage control as the KE storage capability is larger than DC-link capacitor. At the same time, significant rotor speed variations are caused compared with MPPT control since additional rotor speed acceleration and deceleration is essential for providing active power support. Specifically, the regulation performance is relatively better when power production is required to decrease compared with the situation when power production should be increased. For example, during the period from 350s to 500s, the regulation command is larger than the mechanical power captured by WT. Hence it requests rotor speed to decelerate to release KE to track the regulation command. However, the energy released from KE discharging is marginal as compared to the energy loss caused by non-MPP operation. Therefore, the lower bound of rotor speed deceleration is set (i.e. ω_{opt}) when allocating regulation task to the rotor speed control in this chapter.

3.4.2.3 Pitch Angle Control

The power production of PMSG-based WT using pitch angle control is presented in Fig. 3.11(b), which can be seen that the control command can be effectively followed in the situation that power production should be curtailed. At the same time, Fig. 3.11(e) shows that the actuation of blade pitch angle becomes more frequent as compared to MPPT control, DC-link voltage control and rotor speed control. It is worth noting that the regulation command cannot be followed rapidly and precisely via adjusting blade pitch angle in some situation. For example, during periods from 227s to 235s and from 250s to 264s, more power generation is supposed to be delivered to system according to the regulation command, however, the pitch angle fails to maintain at zero degree as exhibited in Fig. 3.11(b). This is because the pitch angle control is relatively slow-responding due to its mechanical characteristics.

3.4.2.4 Simultaneous Control Strategy

Simultaneous control integrates three regulation resources and they concurrently trace the regulation command without coordination. Fig. 3.12 demonstrates the regulation performance and indicates that simultaneous control is superior than individual control strategies. In particular, the regulation command can be followed rapidly and precisely when power deloading is required. In contrast, when more power production is required (i.e. overloading), the regulation performance is however less satisfactory. This is because the energy storage capabilities of the DC-link capacitor and KE are not adequately exploited due to the frequent actuation of blade pitch angle. In general, compared with individual control strategies, the fluctuating magnitude of DC-link voltage, the variation of rotor speed and the activation frequency of blade pitch angle are considerably mitigated via deploying the simultaneous control, which can be seen in Fig. 3.12(b-d).

3.4.2.5 Hierarchical Control Strategy

The simulation results with the proposed hierarchical control are given in Fig. 3.12. By comparison, it is clearly seen that the proposed hierarchical control is superior to the simultaneous control especially when overloading is required. For example, in term of the shadow areas marked in Fig. 3.12 (a), the energy harvesting capability of hierarchical control is better than the simultaneous control and the more released energy is calculated as 4.492kW·h. It proves that more overloading support can be provided by the hierarchical control. As can be seen in Fig. 3. 12(b-c), the DC-link voltage and rotor speed are both varied within the acceptable range when the hierarchical control is activated. The regulation task is properly assigned to individual resources according to their response priority and regulation capabilities with the proposed hierarchical control strategy. As a consequence, the manipulation of blade pitch angle is less frequently compared with the simultaneous control, as shown in Fig. 3.12(d). Owing to the regulation command can be better followed by the hierarchical control, the improvement of frequency behavior is more significant as compared to simultaneous control and MPPT control, which can be seen in Fig. 3.12(f). To make a quantitative comparison, the standard system frequency deviation throughout 600s with different control strategies is calculated respectively with the sampling time of 1s. The standard system frequency deviation is 0.206 with MPPT control. When the simultaneous control is utilized, the standard frequency deviation decreases to 0.141. Once the hierarchical control is adopted, the standard frequency deviation is reduced to 0.139. As a result, the power regulation responsibility of SG is significantly alleviated, which in turn reduces the tear and wear and maintenance costs. The deviation between the actual power production and the regulation command, the pitch angle actuation time and the total captured wind energy with MPPT control, simultaneous control and hierarchical control are quantified and listed in Table 3.1. It is obvious that the proposed hierarchical control outperforms the simultaneous control in terms of 1) smaller regulation deviation; 2) less WT mechanical fatigue; and 3) more harvested wind energy.

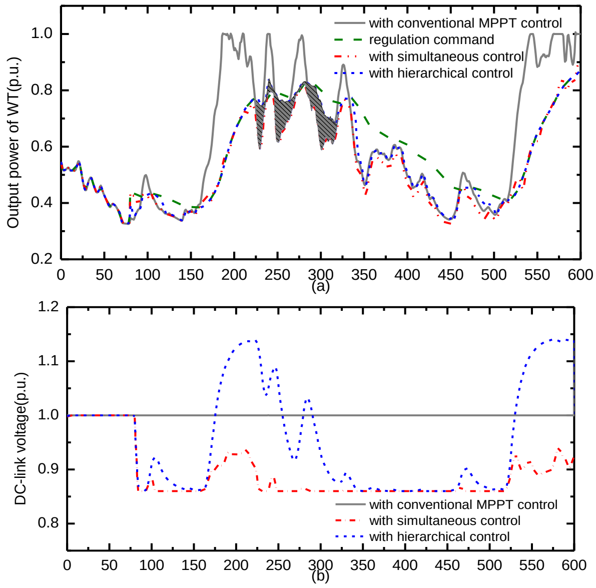

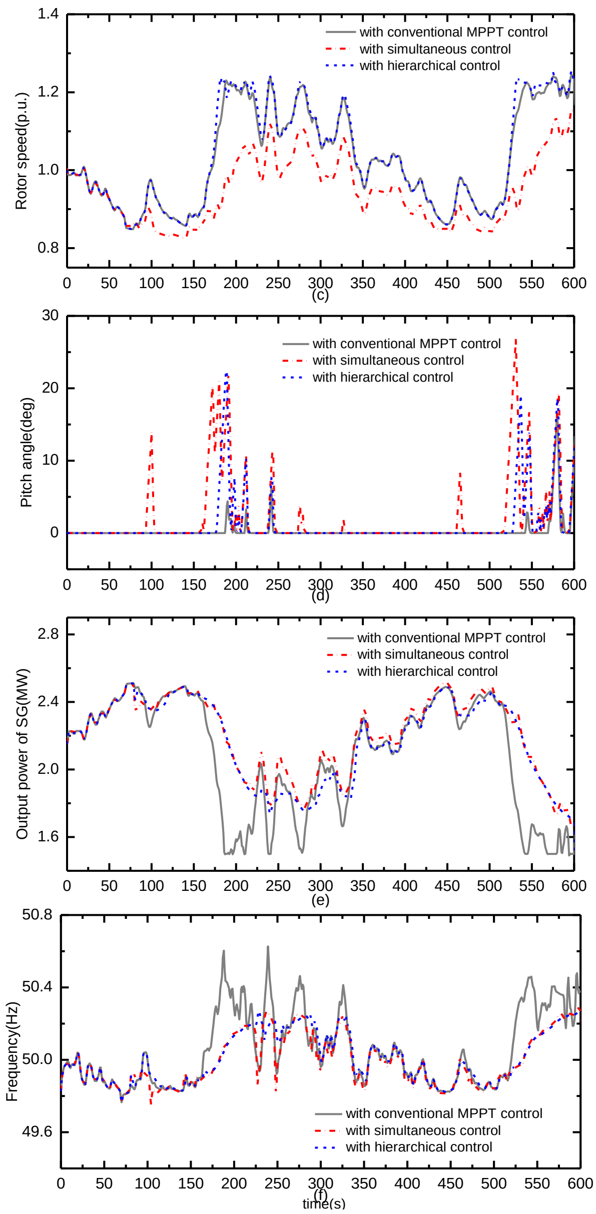

Fig. 3. 13 Simulation results for simultaneous and hierarchical control (a). Output power of PMSG-based WT, (b). DC-link voltage, (c). Rotor speed, (d). Pitch angle, (e) Output power of SG, (f) System frequency

Table 3. 1 Comparison of different control strategies

	MPPT control	Simultaneous control	Hierarchical control
Regulation deviation	0.1483	0.0721	0.0558
Actuation time of pitch angle	61s	187s	120s
Total captured	151.988	132.306	137.681

wind energy	kW·h	kW·h	kW·h

3.5 Summary

This chapter comprehensively investigates two novel control schemes for wind power regulation. The first one utilizes all the regulation resources (i.e. DC-link capacitor, rotating mass and blade pitch angle) of PMSG-WT simultaneously to trace the identical regulation command. To pursue a better regulation performance, the hierarchical control is proposed, which aims to coordinate these three regulation resources in an optimal manner. The regulation resources are utilized in a hierarchical manner via the proposed rule-based regulation task allocation algorithm. Specifically, the response priority of individual regulation resource is predetermined according to their characteristic. In addition, their regulation capability is real-time evaluated. The simulation results exhibit that the proposed hierarchical control can effectively follow regulation command and harvest more energy as compared to simultaneous control scheme.

Chapter 4 A Novel Control Strategy for Wind Farm Active Power Regulation Considering Wake Interactions

Nomenclature

P_{wt}	Mechanical power captured by WT
R	Rotor blade radius
C_{p}	Power coefficient
λ	Tip speed ratio
β	Pitch angle
ω_r	Rotor speed
v	Wind speed
P_{wt}^{mpp}	Mechanical captured by WT under MPPT mode
δv	Velocity deficit
C_{T}	Thrust coefficient
A	Area swept by rotor blades
A^{shadow}	Area of wind turbine under shadowing
D	Diameter of rotor blade
J	Equivalent inertia of wind turbine
H	Inertia constant
P_{KE}	Charging/discharging power in the form of rotor speed accelerating
$\omega_{r\max}$	Maximum rotor speed
$\omega_{r\min}$	Minimum rotor speed
ω_{rmpp}	Rotor speed under MPPT mode
P_{KE}^{cha}	Charging power in the form of rotor deceleration
P_{KE}^{disc}	Discharging power in the form of rotor deceleration

$P_{e\min}^{rot}$ The minimum output power of wind turbine with KE fully charged

$P_{e\max}^{rot}$ The maximum output power of wind turbine with KE fully discharged

ΔP_{rot}^{de} Available charging range of KE

ΔP_{rot}^{ov} Available discharging range of KE

ΔP_{wt} Active power regulation task of individual WT

P_{wt}^{act} Measured actual power output of WT

P_{WF}^{com} Dispatch command of the WF

P_{WF}^{act} Measured actual power output of WF

The active power regulation strategy at individual wind turbine control level is investigated in Chapter 3. While when it comes to the upper layer wind farm control level, interactions between the wind turbine should not be neglected. The impact of wake effect on wind power regulation is considered in this chapter, and a novel control scheme is proposed to coordinate WTs in the WF to trace the dispatch order.

This chapter is organized as follows. The modeling of DFIG-based WT and wake effect are illustrated in Section 4.1 The active power control measures of individual DFIG-based WT are discussed in Section 4.2. The adaptive power dispatch strategy for wind farm is proposed in Section 4.3. Case studies and the corresponding analysis are given in Section 4.4. Section 4.5 summarizes this chapter.

4.1 DFIG-based Wind Turbine and Wake Effect Models

4.1.1 DFIG Model

Doubly fed induction generator based wind turbine is a popular wind energy conversion system in industry due to its relatively low capacity of the embedded converter. DFIG-based wind energy conversion system comprises wind turbine, gear-box, induction generator and back-to-back converter, which are given in Fig. 4.1, where ω_r is rotor speed; i_r is rotor current; i_g is grid current; V_{dc} is DC-link voltage; β_{ref} is pitch angle reference; P_{ref} is active power reference generated via MPPT curve. It can be found that the stator is directly connected to grid, while the rotor is interfaced with grid through a back-to-back converter. In general, the capacity of the converter is about 20-30 percent of WT rated capacity. The back-to-back converter is dedicated for synchronizing the electric power and the instantaneous current with varying amplitudes and frequency to the main grid. The MPPT control is achieved at the rotor side converter (RSC) controller and the DC-link voltage is regulated in the grid side converter (GSC) controller.

The main difference between the DFIG and PMSG is that there exists a gear-box in the DFIG wind energy conversion system and its converter capacity is significantly less than PMSG. The modelling and control principle of the back to back converter are similar with PMSG and can be seen in Section 3.1.

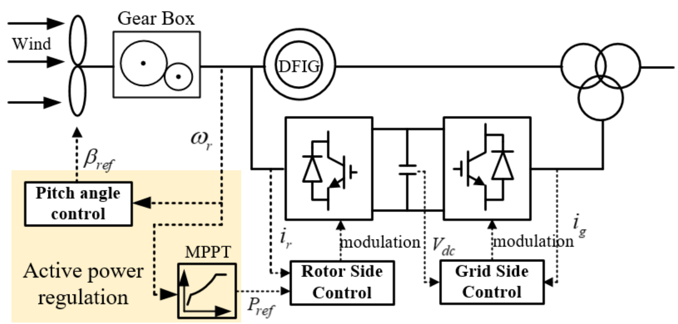

Fig. 4. 1 DFIG wind turbine configuration

The mechanical power extracted from the wind is defined as,

$$P_{wt} = \frac{\rho}{2} \pi R^2 v^3 C_p(\lambda, \beta) \tag{4.1}$$

$$\lambda = \frac{\omega_r R}{v} \tag{4.2}$$

where ρ is air density, R is rotor blade radius, v is wind speed, λ is the tip speed ratio, β is pitch angle, and C_p is power coefficient. Power coefficient represents a nonlinear relationship between the tip speed ratio and pitch angle.

Normally, the blade pitch angle maintains at zero degree when the wind speed is lower than the rated value. In this context, C_p is only dependent on λ. According to Eq. (4.1), there exists a specific rotor speed that yields the maximal power coefficient $C_{p\max}$ for a given wind speed, and the maximum mechanical power captured by the WT can be expressed as,

$$P_{wt}^{mpp} = \frac{\rho}{2} \pi R^2 C_{p\max}(\lambda_{opt}, \beta = 0) v^3 \tag{4.3}$$

where λ_{opt} is the optimal tip speed ratio that could gain the maximum power coefficient.

4.1.2 Wake Effect Model

Wind turbines extract energy form wind and there exists a wake behind the turbine. Broadly speaking, layout of the wind farm and the operation status of each wind turbine both have influence on the wake effect. The power generation of the WF is impacted by the aggregated wake effect. In recent years, several wake models have been put forward. Jensen's wake model is one of the most prevalent one as it is appropriate for engineering applications [99]. In this chapter, Jensen's model is applied to characterizes the wake effect. Jensen's wake effect model is established based on the assumption that the wake expands downstream linearly, which can be shown in Fig. 4.2. The velocity profile of the wind turbine *i* after wake impact can be given by,

$$v_i = v_0(1-\delta v_i) \tag{4.4}$$

where v_0 is the free wind speed, δv_i is the aggregated velocity deficit. It should be known that the effective wind velocity of wind turbine *i* is not only influenced by the neighbor upstream wind turbine that is directly in front of it, but also other upstream wind turbines. Taking wake impact attributed by multiple upstream wind turbines into consideration, the aggregated velocity deficit of wind turbine *i* can be calculated as,

$$\delta V_i = \sqrt{\sum_{j\in N:x_j<x_i}(\delta V_{ij})^2} = \sqrt{\sum_{j\in N:x_j<x_i}((1-\sqrt{1-C_{Tj}})(\frac{D_j}{D_j+2k(x_i-x_j)})^2(\frac{\mathrm{A}_{j\to i}^{shadow}}{A_i}))^2} \tag{4.5}$$

where D_j is the diameter of the turbine *j* blades; C_{Tj} is the thrust coefficient of the turbine *j*, which also represents a nonlinear relationship between the tip speed ratio and the pitch angle. The thrust coefficient can be acquired through a look-up table or curve fitting [100, 101], as given in Fig. 4.3. $x_{\mathrm{i}} - x_{\mathrm{j}}$ is the distance of upstream turbine *j* and downstream turbine *i* along with the wind direction. *k* is the roughness coefficient, it has a default value of 0.075 for farmlands and 0.04 for offshore locations. $\mathrm{A}_{j\to i}^{shadow}$ is the overlap between the area spanned by the wake shadow cone generated by turbine *j* and the area swept by the turbine i (A_i). $A_{j\to i}^{shadow}$ can be calculated using the following mathematical formula,

$$A_{j\to i}^{shadow} = (D_i + 2k(x_i - x_j))^2 \cos^{-1}\left(\frac{L_{ij}}{D_i + 2k(x_i - x_j)}\right) + D_i^2 \cos^{-1}\left(\frac{d_{ij} - L_{ij}}{D_i + 2k(x_i - x_j)}\right) - d_{ij} z_{ij} \tag{4.6}$$

where d_{ij} is the distance between the centre of downstream wind turbine and the centre of the wake effect, L_{ij} is the distance between the centre of the wake effect and the shadow area.

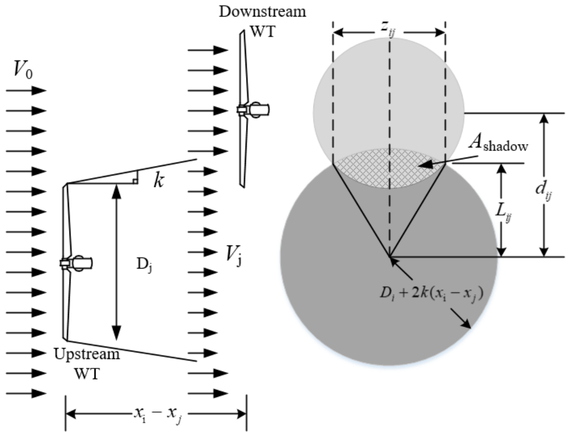

Fig. 4. 2 Jensen's wake effect model

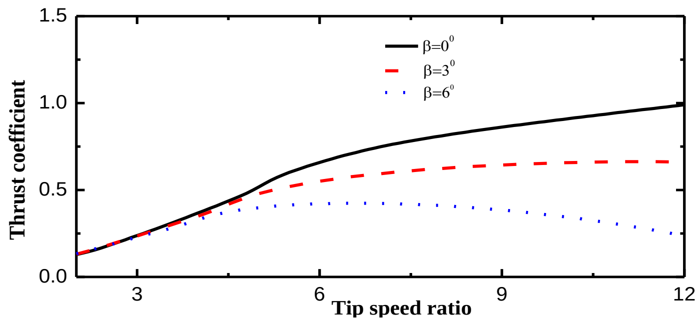

Fig. 4. 3 Thrust coefficient

4.2 Active Power Control Measures of Individual Wind Turbine

In regard to how to regulate the output power via the rotor speed regulation based control and the pitch angle regulation based control, detailed discussion is given in this section. In addition, the energy loss brought by different deloading control strategies is analyzed respectively.

4.2.1 Rotor Speed Regulation based Control

The wind power can be expanded (i.e. $\pm\Delta P$) via utilizing the KE stored in the rotating mass, which is the essential idea of rotor speed control. The dynamic process of the rotor speed regulation based control is illustrated in Fig. 4.4. To extract the maximum mechanical power, WT operates at point A, where the active power reference is generated via the MPPT curve. To become a dispatchable power resource, the WT should no longer operate at the MPPT mode and the active power reference should be revised as the dispatch command. In fact, the active power reference of the WT can be modified to a new value rapidly due to the fast response of power electronic devices. However, the turbine mechanical power cannot change suddenly. The mismatch between the electric power and mechanical power causes rotor speed acceleration/deceleration, which in turn offers extra active power support during KE charging/discharging process. In particular, if less wind power generation is demanded, the WT operating point will be shifted to point B with rotor speed accelerated to a new value. On the other hand, if the dispatch command is larger than MPP, WT can temperately shift to point D with rotor speed deceleration and eventually return back to point A.

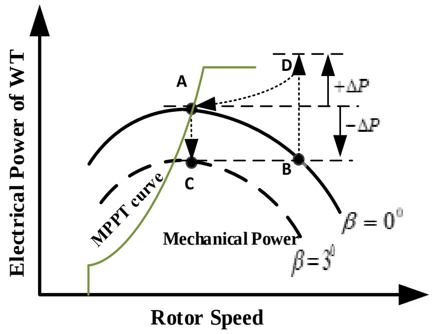

Fig. 4. 4 Control dynamics for rotor speed control and pitch angle control

4.2.2 Pitch Angle Regulation based Control

Under MPPT control mode, the blade pitch angle activates to restrain rotor overspeed when wind speed is larger than the rated value. In power regulation mode, the pitch angle control would activate more frequently than MPPT control. The dynamic process of utilizing pitching control to regulate wind power generation (i.e. $-\Delta P$) can also referred to Fig. 4.4. In particular, in the situation that the received power command is less than actual power production, WT shifts to point C via increasing pitch angle. Different from rotor speed control, pitching control cannot store any excessive energy and thus cannot provide extra power support when overloading is needed.

4.2.3 Wind Energy Loss Analysis

For an individual WT, if the deloading coefficient is fixed, the captured mechanical power can be expressed as,

$$P_{wt}^{del} = \frac{1}{2}\rho A C_{pdel}\left(\lambda, \beta\right) v^3 \tag{4.7}$$

where C_{pdel} denotes the deloading power coefficient.

According to Eq (4.1), the rotor speed and blade pitch angle variation can both alter the captured mechanical power by wind turbine. Since their working principle is different, the corresponding wind energy loss is also different and the detailed information is given respectively in the following.

4.2.3.1 Rotor Speed Control

For an individual WT, the KE stored in its rotational rotor can be expressed as,

$$E = \frac{1}{2} J \omega_r^2 \tag{4.8}$$

where J denotes the equivalent inertia of the WT.

As mentioned above, the imbalance between the captured mechanical power and electric power of WT leads to rotor speed variation. The charging/discharging power during rotor speed variation process can be calculated via the differential of Eq (4.8). In MPPT mode, the electric power reference is determined by the MPPT curve. To provide active power regulation ancillary service, the dispatch command is introduced to the wind turbine controller and is tracked as the new active power reference. The above-mentioned process can be expressed as,

$$P_{wt} - P_e = P_{wt} - P_{com} = \frac{dE}{dt} = J\omega_r \frac{d\omega_r}{dt} = P_{KE} \tag{4.9}$$

where P_{com} is the dispatch command and P_{KE} is the charging/discharging power.

The inertia constant H of the WT can be expressed as,

$$H = \frac{J\omega_{rnom}^2}{2P_{wtN}} \tag{4.10}$$

where P_{wtN} is the nominal power of WT, ω_{rnom} is the nominal turbine speed.

Using the definition of inertia constant, Eq (4.9) can be rewritten as Eq (4.11) in per-unit form,

$$P_{wt[pu]} - P_{com[pu]} = 2H\omega_{r[pu]}\frac{d\omega_{r[pu]}}{dt} \tag{4.11}$$

Integrating Eq (4.11) over time t_0 to t_1, when the dispatch command is less than MPP, the total wind energy production once the rotor speed regulation based deloading control is utilized can be obtained as following,

$$E_{wt}^{rot} = \int_{t_0}^{t_1}\sum_{i=1}^{N} P_{wti}dt = \int_{t_0}^{t_1} P_{WF}^{com}dt + 2H\int_{t_0}^{t_1}\sum_{i=1}^{N}\omega_{ri}d\omega_{ri} = \int_{t_0}^{t_1} P_{WF}^{com}dt + H\sum_{i=1}^{N}(\omega_{ri1}^2 - \omega_{ri0}^2) \tag{4.12}$$

where N is the number of WTs in the WF.

In contrast, the total wind energy production of the WF with MPPT control can be expressed as,

$$E_0 = \int_{t_0}^{t_1}\sum_{i=1}^{N} P_{wti}^{mpp}dt \tag{4.13}$$

According to Eq (4.12) and Eq (4.13), the wind energy loss with rotor speed regulation based deloading control can be expressed as,

$$E_{loss}^{rot} = E_0 - E_{wt}^{rot} = \int_{t_0}^{t_1}(\sum_{i=1}^{N} P_{wti}^{mpp} - P_{WF}^{com})dt - H\sum_{i=1}^{N}(\omega_{ri1}^2 - \omega_{ri0}^2) \tag{4.14}$$

It can be found that a portion of curtailed wind power is stored in the rotating mass via KE charging. Hence the wind energy loss during active power regulation process can be decreased.

4.2.3.2 Pitch Angle Control

Unlike the rotor speed control, pitch angle control does not possess any component to store the excessive energy and the redundant power is directly curtailed when it is activated. Correspondingly, the total wind energy production of the WF with the utilization of pitching based deloading control can be expressed as,

$$E_{wt}^{pit} = \int_{t_0}^{t_1} \sum_{i=1}^{N} P_{wti} dt = \frac{1}{2} \int_{t_0}^{t_1} P_{WF}^{com} dt \tag{4.15}$$

According to Eq (4.13) and Eq (4.15), the wind energy loss brought along by pitching based deloading control can be calculated as,

$$E_{loss}^{pit} = E_0 - E_{wt}^{pit} = \int_{t_0}^{t_1} (\sum_{i=1}^{N} P_{wti}^{mpp} - P_{WF}^{com}) dt \tag{4.16}$$

Comparing Eq (4.14) to Eq (4.16), it can be observed that the main difference of the energy loss brought along by rotor speed regulation based deloading control and pitch angle regulation based deloading control lies in KE alternation. In addition to the advantage on energy storage, there are other two reasons that why rotor speed control is preferred. The first reason is that it has a fast response as the rotor speed is controlled through electronic converters. The second reason is that the frequent actuation of blade pitch angle unavoidably leads to mechanical fatigue.

4.3 Proposed Adaptive Control Strategy in Wind Farm

For the sufficient utilization of the buffer provided by KE and mitigating the pitch actuator manipulation frequency while following the dispatch command, the cooperation among WTs in the WF should be investigated. An adaptive method is proposed in this section to assign the active power regulation task to individual WT according to their operational status with taking the wake characteristic into consideration.

4.3.1 Power Dispatch in Deloading Situation

The deloading control should be applied in the situation when the dispatch command is less than WF actual power production capability. To trace the dispatch command, a feasible solution is to equally allocate the deloading task to individual WT. Nevertheless, when wake interactions are involved, this is no longer the optimal solution. The wind speed reaching down-WTs is significantly lower than the free wind speed due to the wake effect, which in turn ensures that they have larger KE charging range than up-WTs. The equally distribution method would lead to the consequence that the pitch angle of upstream WTs should be increased to a large value to meet the deloading task while the KE of down WTs is not fully charged. To enhance total KE storage in the WF and reduce mechanical fatigue of WTs, the deloading task should be assigned adaptively to individual WT based on their KE charging range.

Though the rotor speed control has a higher responses priority in the proposed deloading task allocation strategy, it should be known that the variation of rotor speed of up WTs generates influence on energy harvesting capability of down WTs owing to the wake effect. As exhibited in Fig. 4.3, the rotor speed acceleration leads to increase of the thrust coefficient when the blade pitch angel maintains at zero degree. This results in the reduction of wind speed reaching downstream WTs, and in turn decreasing their power production. To enhance total KE storage, the response priority of rotor speed control of WTs in different rows is predefined as per from back row to front row in sequence in this chapter. In case all WTs' KE is fully charged while the deloading requirement is not reached, the blade pitch angle has to manipulate. Similarly, the variation of blade pitch angle impacts the operation states of down WTs. It can be observed from Fig. 4.3, the thrust coefficient decreases with the increase of pitch angle, and then gives rise to increase of wind speed reaching downstream WTs. Therefore, to reduce mechanical fatigue, the response priority of pitch angle control in different rows WTs is also defined from back row to front row in sequence.

In case the response priority of the deloading control in different rows WTs is determined, the next task is to evaluate the deloading capability of each WT. According to Eq (4.9), the power production of WT is decided by two terms. The first term is the captured mechanical power, and the second term is the power converted from the KE variation. Specifically, the available power converted from KE charging can be determined by current rotor speed and the maximum rotor speed, and it can be formulated as following with a linear KE injection,

$$P_{\mathrm{KE}}^{cha} = \frac{\Delta E}{\Delta t} = P_{wtN} H \frac{\omega_{r\max}^2 - \omega_r^2}{\Delta t} \tag{4.17}$$

where P_{KE}^{cha} is the charging power through rotor acceleration, Δt is the dispatch cycle.

According to Eq (4.9) and Eq (4.17), the WT power production with KE fully charged can be expressed as,

$$P_{e\min}^{rot} = \frac{1}{2}\rho A C_p(\omega_{r\max}) v^3 - P_{KE}^{cha} \tag{4.18}$$

The two scenarios that the deloading requirement could be achieved by only depending on rotor speed control or depending on the integration of rotor speed control and pitch angle control are going to be discussed respectively in the following.

4.3.1.1 Deloading via Rotor Speed Control

Assuming there are *m* rows WTs and each row consists of *n* WTs in the WF. In the situation the required deloading level can be reached by only utilizing rotor speed control, as expressed in Eq. (4.19), the deloading task should be assigned to individual WT adaptively base on their instant KE charging range.

$$P_{WF}^{com} \geq m\sum_{i=1}^{n} P_{e\min i}^{rot} \tag{4.19}$$

As mentioned before, the last row WTs has the highest response priority, and their deloading task can be allocated as,

$$\Delta P_{wt,n} = \min\left\{\frac{m \cdot n}{m}\Delta P, \Delta P_{rot,n}^{de}\right\} = \min\left\{n\Delta P, \Delta P_{rot,n}^{de}\right\} \tag{4.20}$$

where ΔP is the deviation between the actual power production of WF P_{WF}^{act} and the dispatch command of the WF P_{WF}^{com} (i.e. $\Delta P = P_{WF}^{act} - P_{WF}^{com}$), $\Delta P_{rot,n}^{de}$ is the deviation between the power production of the *n*-th row WT and their power production with KE fully charged $P_{e\min,n}^{rot}$. Eq. (4.20) guarantees that if the deloading demand can be achieved with the rotor speed regulation based control of the last row WTs, the deloading task would assign to them equally. Otherwise, the deloading task would assign to them based on their available

KE charging range.

Based on the predefined response priority and the regulation capability evaluation, the deloading task allocated to the arbitrary upstream *i*-th row WTs is defined as,

$$\Delta P_{wt,i} = \min\left\{ n\Delta P - m\sum_{j=i+1}^{n} \Delta P_{wt,j}, \Delta P_{rot}^{de,i} \right\} \tag{4.21}$$

It can be found that Eq (4.20) and Eq (4.21) ensure that the deloading task can be allocated to each WT adaptively based on their response priority and their instant KE charging range. As a result, the KE storage capability can be adequately exploited.

4.3.1.2 Deloading via Integration of Rotor Speed Control and Pitch Angle Control

In the scenario that the required deloading level cannot be reached via only relying on rotor speed control, as shown in Eq (4.22), the pitch angle control has to be involved in.

$$P_{WF}^{com} < m\sum_{i=1}^{n} P_{e\min i}^{rot} \tag{4.22}$$

As mentioned above, the last row WTs has the highest priority of the pitching based deloading control. In this context, the deloading task can be calculated as,

$$\Delta P_{wt,n} = \min\left\{ n\Delta P - m\sum_{i=1}^{n\text{-}1} \Delta P_{rot,i}^{de}, P_{wt,n}^{act} \right\} \tag{4.23}$$

where $P_{wt,n}^{act}$ is the actual power production of the *n*-th row WT. Eq (4.23) guarantees that the excessive power that cannot be transformed into KE will be discarded via the increase of blade pitch angle. Similarly, for the *i*-th row WTs, the deloading task can be assigned in accordance with the following mathematical formula,

$$\Delta P_{wt,i} = \min\left\{ n\Delta P - m(\sum_{j=1}^{i-1}\Delta P_{rot,j}^{de} + \sum_{j=i+1}^{n}\Delta P_{wt,j}), P_{wt,i}^{act} \right\} \tag{4.24}$$

where $P_{wt,i}^{act}$ is the actual power production of the *i*-th row WT. Eq (4.23) and Eq (4.24) ensure that the activation frequency of pitch actuator is mitigated as much as possible meanwhile fulfilling the deloading command.

4.3.2 Power Dispatch in Overloading Situation

When the dispatch command is larger than actual power production, WF is expected to deliver more power to grid, which is referred as overloading control. To follow the dispatch command, the stored KE in deloading situation should be released back to system. Similarly, when wake effect is taken into account, the cooperation of WTs should be investigated. As mentioned before, the rotor speed variation of up WTs would affect power production of down WTs. As Fig. 4.3 shows, the rotor speed deceleration leads to thrust coefficient decreases, which increases wind speed reaching down-WTs and in turn increases their power production. Therefore, the overloading task allocation priority among different rows WTs should be predetermined from the front row WTs to the back row WTs in sequence.

It is worth noting that the rotor speed variation should be limited by the operating ranges, as the WT might stall if too much KE is extracted. Based on [102], if the rotor speed of WT is lower than the MPP one, the system small signal stability would be reduced. To avoid this issue, the maximum power production of individual WT should be subjected to the following formula,

$$P_{e\max}^{rot} = \frac{1}{2}\rho AC_p(\omega_{rmpp})v_w^3 - P_{KE}^{disc} = \frac{1}{2}\rho AC_p(\omega_{rmpp})v_w^3 - P_{wtN}H\frac{\omega_{rmpp}{}^2 - \omega_r^2}{\Delta t} \quad (4.25)$$

where ω_{rmpp} is the rotor speed at MPP status, P_{KE}^{disc} is the discharging power during rotor deceleration.

As mentioned before, the first row WTs has the highest priority to provide response to active power regulation service in overloading scenario, and the corresponding overloading task can be expressed as,

$$\Delta P_{wt,1} = \min\left\{n\Delta P, \Delta P_{rot,1}^{ov}\right\} \quad (4.26)$$

where $\Delta P_{rot,1}^{ov}$ is the deviation between the actual power production of the *n*-th row WT and its power production with KE fully discharged $P_{e\max,1}^{rot}$. Eq (4.26) guarantees that the minimal value (negative) of WT overloading capability and the deviation between power command and actual power production of the WF is selected. This allocation method avoids the excessive rotor speed deceleration. In case the power deviation still cannot be offset with the completely discharge of KE of the first front row WTs, the remaining power deviation will be allocated to their neighbor down WTs. Against this background, the overloading task of the *i*-th row WTs can be allocated as,

$$\Delta P_{wt,\mathrm{i}} = \min\left\{n\Delta P - m\sum_{j=1}^{i-1}\Delta P_{rot,j}^{ov}, \Delta P_{rot,i}^{ov}\right\} \quad (4.27)$$

In the same way, Eq (4.27) ensures the *i*-th row WTs can be operate in a stable region during the KE discharge process.

In order to fulfill the proposed adaptive control scheme for active power regulation in the WF, a WF central controller should be established as shown in Fig. 4.5, where P_{WF}^{com} , P_{WF}^{act} are dispatch command and measured actual power production of the WF, respectively; $\omega_{r,i}$, β_i , v_i , $P_{wt,i}^{act}$, $P_{wt,i}^{mpp}$, $P_{ref,i}$ are rotor speed, pitch angle, wind speed, measured actual power production, the maximum captured mechanical power and the active power reference of the *i*-th WT, respectively. The deloading/overloading task allocated to individual $\Delta P_{wt,i}$ would be adaptively calculated based on Eqs (4.19-4.27). During the process when WTs participate in active power regulation, the wind speed reaching downstream WTs are impacted by operation states of upstream WTs and the corresponding value can be calculated via wake equations. It is worth noting that the evaluation of KE charging/discharging range and the subsequent active power regulation task allocation for individual WT can be execute promptly, which guarantees the online application feasibility of proposed control strategy.

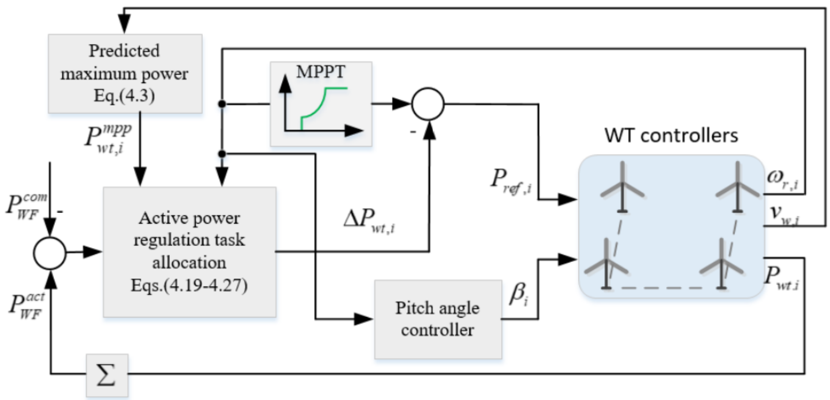

Fig. 4. 5 The proposed adaptive active power regulation method for WF

4.4 Case Studies

To access the effectiveness of the proposed strategy, a testing system including two conventional synchronous generators (SGs), a DFIG-based wind farm (there are three rows and each row consisting of four WTs in the WF), and a time varying power load is modelled in DIgSILENT/PowerFactory. The schematic diagram can be seen in Fig.4.6. The total nominal capacity of the wind farm is 60-MVA. The spacing of two adjacent DFIGs is 10R. Detailed simulation parameter settings can be referred to the Appendix.

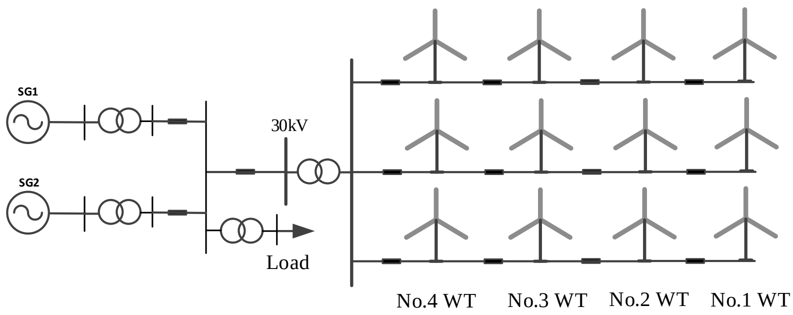

Fig. 4. 6 Single line diagram of the text system

To evaluate the performance of the proposed adaptive power control strategy, different wind speed scenarios (i.e. low constant wind speed, high constant wind speed and variable wind speed) are considered in case studies. Detailed simulation results for above three cases is analyzed as following.

4.4.1 Low Wind Speed Condition

The concerned free wind speed v_0 is assumed as 9m/s. The load consumption is set as 90-MW initially, a load sudden decrease (4.8-MW) event occurs at t=80s and a load sudden increase (9-MW) event occurs at t=160s respectively. The regulation performance of the uniform power dispatch method (i.e. the regulation task is equally distributed to each WT) and the proposed method is compared through simulation. Fig. 4.7(a) exhibits the dynamic frequency behaviour throughout simulation, it can be observed that when load decrease disturbance occurs, the frequency peak is 50.253Hz and the quasi-steady state frequency is 50.094Hz when the MPPT control is applied. By comparison, the frequency behavior is the worst with MPPT control. This is due to the power balance responsibility is only dependent on SGs. Once the WF provides active power regulation service, the WF power production decreases to follow the dispatch command. Consequently, system frequency maintains at 50Hz throughout the event no matter applies the uniform power dispatch strategy or the proposed strategy. Since the total KE charging range of WTs is sufficient enough, the required deloading level can be reached without the activation of the pitch angle control. Hence the blade pitch angle remains at zero degree with both the uniform deloading control and the adaptive deloading control. However, the operation status of WTs is different with different deloading strategies, which as shown in Fig. 4.7(c). Overall, compared with the condition when the uniform deloading strategy is applied, the total KE storage capacity in the WF is larger with the proposed adaptive deloading control strategy. This is owing to the wake characteristic, as illustrated in section 4.3. Accordingly, the WF could generate more active power when overloading is needed, which in turn improves system frequency behaviour. It can be found that frequency nadir increases from 49.616Hz to 49.905Hz with the proposed adaptive overloading strategy during sudden increase disturbance, while the frequency nadir improvement is 284mHz with the uniform overloading strategy. The SGs' output power generation profile is exhibited in Fig. 4.7(f). It can be discovered that after WF taking part in active power regulation service, their mechanical power remains almost unchanged throughout the load decrease disturbance. While in load increase disturbance, when the proposed adaptive control strategy is applied, the mechanical power from the governor increases slower than under the condition that the uniform power dispatch control and MPPT control are applied. The impact of wake interactions on the effective wind speed reaching downstream WTs can be found in Fig. 4.7(e).

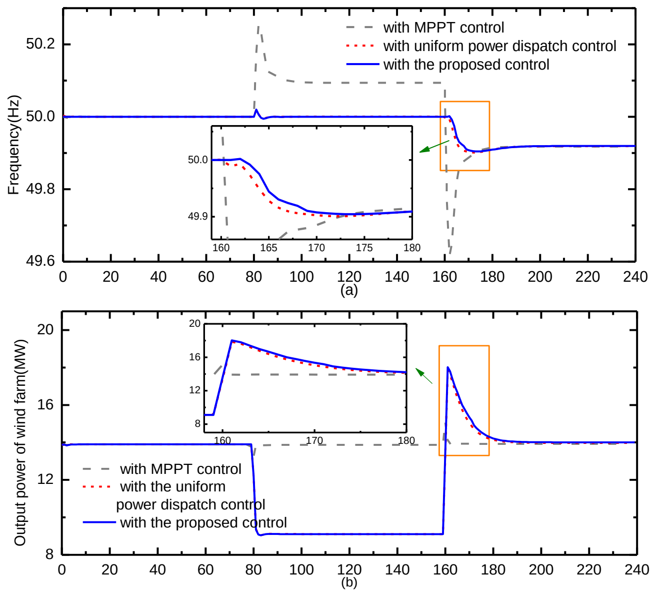

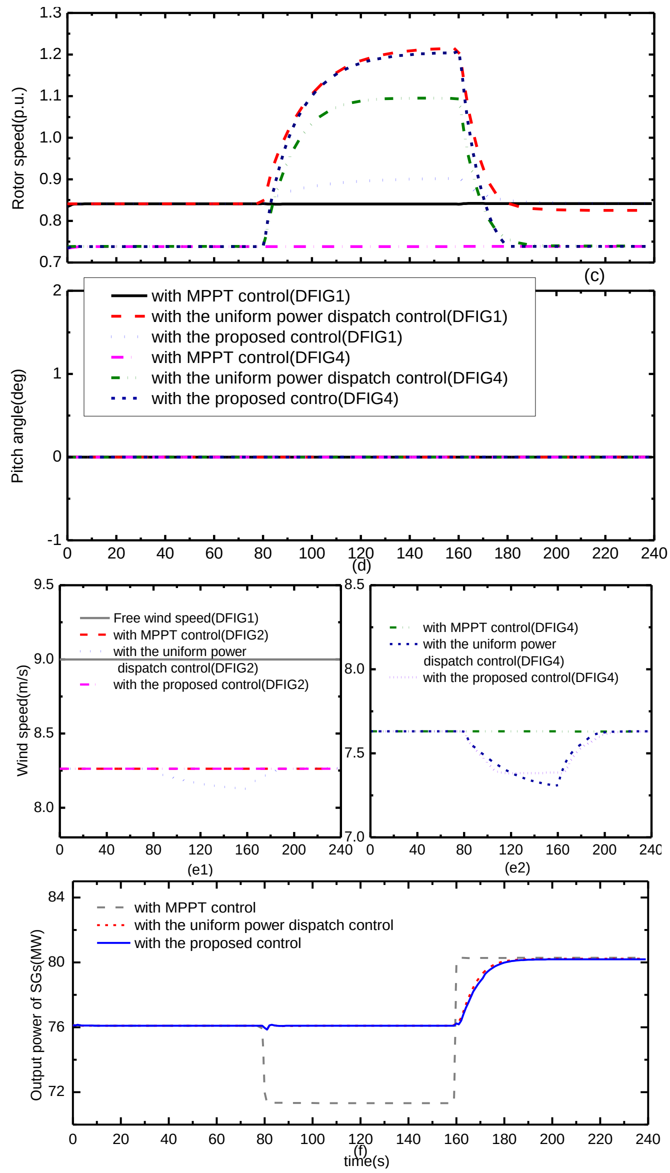

Fig. 4. 7 Simulation results for case study with low constant wind speed. (a) System frequency, (b) WF output power, (c) DFIG rotor speed, (d) DFIG pitch angle, (e) Wind speed, (f) SGs output power

4.4.2 High Wind Speed Condition

A 12m/s free wind speed is considered in this case. The load variation events are set the same with case 1. It can be found that after WF offering active power regulation serve, the mismatch between load and generation is completely offset throughout the load increase disturbance with both uniform and adaptive deloading strategy. And then system frequency maintains at 50Hz.

However, the pitch angle control of the first row DFIG has to activate to achieve the deloading requirement once the uniform power dispatch control is applied, as it already operates at a relatively high rotor speed before the event. In contrast, when the proposed adaptive strategy is implemented, the KE of downstream WTs is fully charged since the deloading task is allocated to them based on their available KE charging range. Hence pitch angle control of upstream WTs does not need to response to the dispatch command. The load increases by 9-MW at *t*=160s. By comparison, it can be clearly seen from Fig. 4.8(a) that system behavior is the best with the proposed adaptive deloading strategy as the dynamic frequency deviation is the smallest and the recover time is the least. Specifically, frequency nadir increases to 49.9Hz in the situation that the proposed control is applied, while frequency nadir only increases to 49.887Hz with the uniform power dispatch control. This is because more KE can be stored in the rotational rotor in deloading situation with the proposed adaptive strategy, and then more active power can be released back to system in overloading scenario, as shown in Fig. 4.8(b).

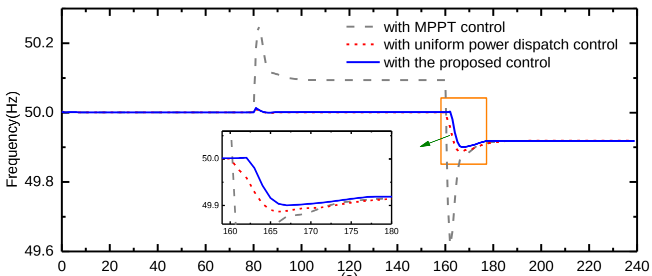

(a)

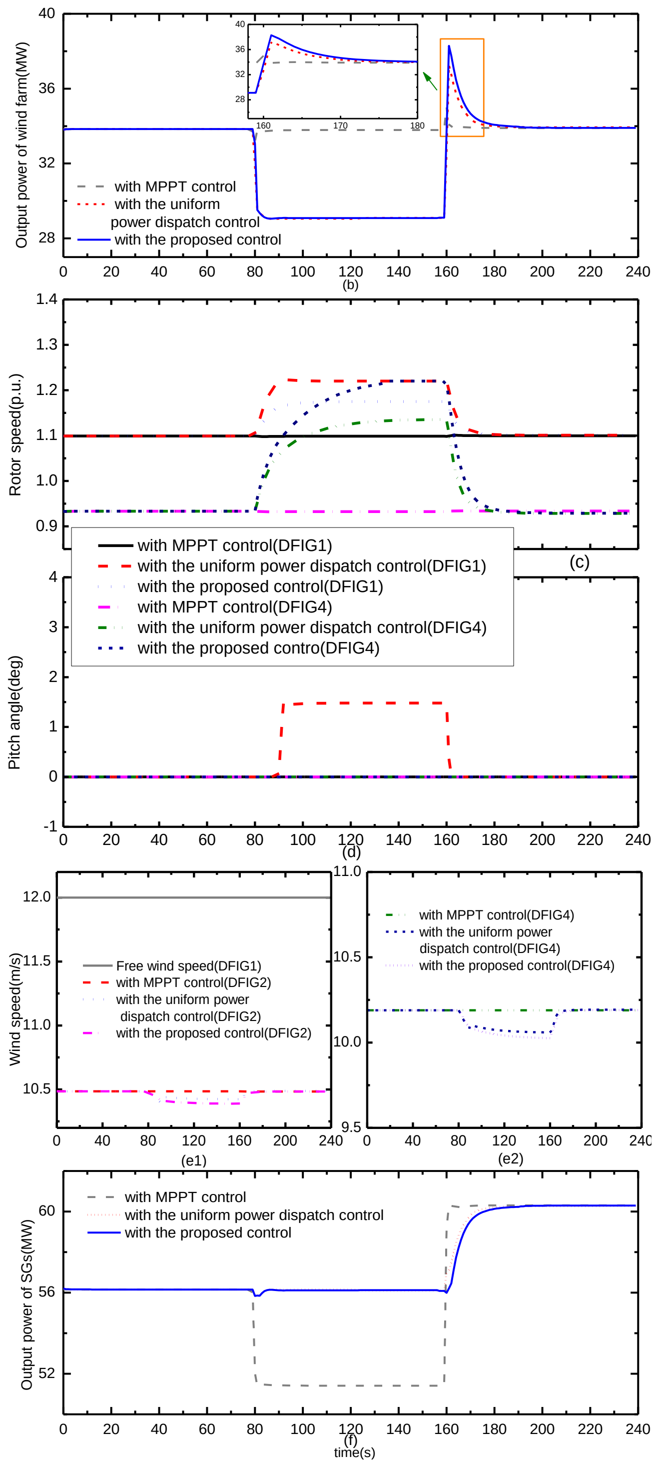

Fig. 4. 8 Simulation results for case study with high constant wind speed. (a) System frequency, (b) WF output power, (c) DFIG rotor speed, (d) DFIG pitch angle, (e) Wind speed, (f) SGs output power

4.4.3 Variable Wind Speed Condition

A set of time varying wind speed data for 300s is exhibited in Fig. 4.9(e), which is used to evaluate the active power regulation service the WF contributes. The active power regulation performance when different control strategies is utilized is assessed by comparing the following four aspects: *total energy harvesting, total amount of pitch regulation, total amount of pitch angle actuation time, standard frequency deviation deviation (i.e. the standard frequency deviation is quantified to evaluate the frequency behavior, which is defined as:* $\delta = \sqrt{1/N\sum_{i=1}^{N}(f_{meas} - f_{ref})^2}$ *,where N is the total sampling amount, which is 300 in this simulation,* f_{meas} *is the measured frequency and* f_{ref} *is the nominal frequency)and standard dispatch command deviation (i.e. the standard dispatch command deviation is quantified to evaluate the active power regulation performance, which is defined as:* $\delta = \sqrt{1/N\sum_{i=1}^{N}(P_{\mathrm{WF}}^{act} - P_{WF}^{com})^2}$ *).* Simulation results are demonstrated in Tables 4. 1 and Figs. 4. 9 respectively.

As indicated in table 4.1, the proposed strategy is more energy-efficient than the uniform power dispatch strategy as the total captured wind energy through the proposed adaptive strategy is larger. This is because more KE can be stored in the rotating mass when deloading is required and hence more active power support can be provided when ovloading is needed with the proposed adaptive dispatch strategy. Since the rotor speed control always response to the active power regulation task with the highest priority in the proposed strategy, the total amount of pitch regulation and total amount of pitch angle actuation time are both reduced significantly compared with the uniform power dispatch strategy. Therefore, it can be concluded that the mechanical fatigue of WTs can be significantly mitigated. To show the dynamic operation status of WTs while fulfilling the dispatch command, Fig. 4.9(c) and (d) give the profiles of. It can be seen that when the uniform power dispatch strategy is applied, the rotor speed of back row WTs is lower than up row WTs, and the pitch angle of up row WTs activates more frequently accordingly. This is because KE of down-WTs is always not fully charged. When the proposed adaptive dispatch strategy is applied, the charging range of down WTs can be adequately exploited and pitch angle control of up WTs does not need to activate. In addition, the excessive rotor speed deceleration is avoided due to Eqs (4.25-4.27) and then the stable operation of WTs can be always ensured, as shown in Fig. 4.9(c). Compared with the condition when the MPPT control is utilized, system frequency fluctuations are significantly mitigated no matter with the uniform power dispatch method or with the proposed adaptive dispatch method. In particular, the proposed adaptive method has a better frequency regulation performance as indicated in Fig. 4.9(a) and Table 4.1. The frequency regulation burden of SGs is significantly reduced as system frequency fluctuation is mitigated after WF participating in active power regulation service. As a consequence, their power generation becomes smoother, which can be seen in Fig. 4.9(f). Hence their tear and wear and the operation and maintenance costs are reduced remarkably. The influence of upstream WTs' operation on wind speed reaching downstream WTs is demonstrated in Fig. 4.9(e). In the light of simulation results, it can be deduced that the active power regulation task can be adaptively assigned to individual WT based on their response priority and their KE charging/discharging range. As a result, the total wind energy loss and mechanical stress of WTs are lower down while providing active power regulation service.

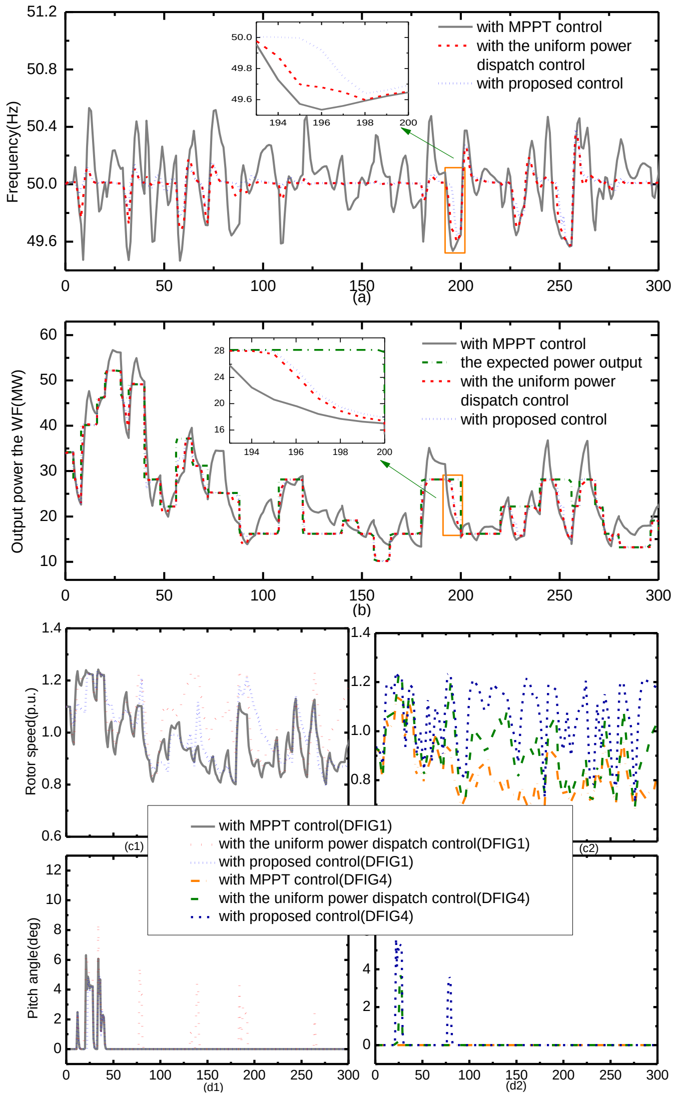

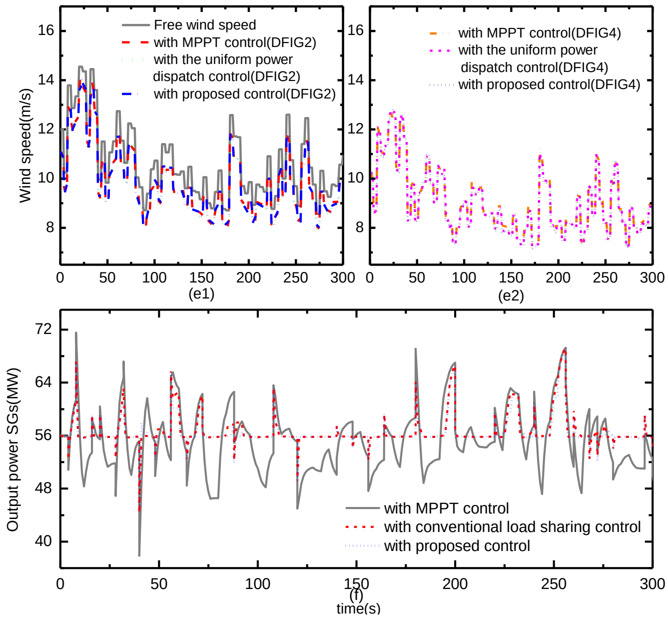

Fig. 4. 9 Simulation results for case study with time-varying wind speed. (a) System frequency, (b) WF output power, (c) DFIG rotor speed, (d) DFIG pitch angle, (e) Wind speed, (f) SGs output power

Table 4. 1 Comparisons of simulation results

	MPPT control	Uniform power dispatch	The proposed control
Total captured wind energy(kW·h)	1713.52	1629.85	1639.02
Total amount of pitch regulation(deg)	250.59	588.51	401.64
Total amount of pitch angle actuation time(s)	123	324	174
Standard frequency deviation (Hz)	0.23	0.11	0.09
Standard dispatch command deviation	4.84	2.76	2.51

4.5 Summary

This chapter proposes a novel control strategy for WF complying with the dispatch command, which inherently takes wake effect into account. In that WTs operation states are different from each other owing to wake effect, an adaptive method to allocate the active power regulation task among WTs is developed. Specifically, the deloading and overloading task allocation priority of WTs in different rows are predetermined based on the wake characteristic. In addition, a KE storage estimation module is set up to measure the KE charging/discharging range of each WT in real time. Consequently, the variable rotor speed operation range can be adequately exploit in deloading situation and the stable operation of WTs can be guaranteed in overloading situation. The proposed control strategy is tested in a WF and simulation results exhibit its promising performance in enhancing total energy harvesting of the WF and alleviating mechanical fatigue of WTs meanwhile providing active power regulation ancillary service.

Chapter 5 Mileage-responsive Wind Power Smoothing

Nomenclature

$D_m(t)$	Mileage of AGC unit *m* at time slot *t*
$P_{reg}^{m}(t)$	Actual power output at time slot *t* of AGC unit *m*
$S_m(t)$	Mileage price at time slot *t*
$K_m(t)$	Performance coefficient of AGC unit *m* at time slot
γ_t	Mileage-based clearing price at time slot t
g_t^i	Regulation power of AGC unit *i* at time slot *t*
E_{base}^{wf}	Base values for normalizing energy harvesting of the wind farm
$C_{\text{base}}^{\text{mileage}}$	Base values for mileage cost
P_{Ei}^{t}	Electric power output of the *i*-th WT
ρ	Air density
v_{t}	wind speed
C_{P}	power coefficient
J	Equivalent moment of inertia of turbine blades and

	generator
α	Weighting coefficient
P_{MPPi}^{t}	maximum mechanical power that captured from wind
P_{Ki}	maximum power that can be converted KE release
ω_{MPP}	rotor speed at MPP status
$\omega_i(t)$	Rotor speed of the *i*-th WT at time slot *t*
$\beta_i(t)$	Pitch angle of the *i*-th WT at time slot *t*
$D_m^{up}(t)$	Up regulation mileage of AGC unit *m* at time slot *t*
$D_m^{down}(t)$.	Down regulation mileage of AGC unit *m* at time slot *t*
$P_{reg\_up}^{m}(t)$	Up regulation power of AGC unit *m* at time slot *t*
$P_{reg\_down}^{m}$	Down regulation power of AGC unit *m* at time slot *t*
$P_{schedule}(t)$	Scheduled power generation in power grid at time slot *t*
$P_{load}(t)$	Instantaneous system load demand at time slot *t*
$P_{wind}(t)$	Power generation of wind farm at time slot *t*

In Chapter 3 and Chapter 4, the dispatch order for the individual WT and the WF is predetermined and the correlation between wind power generation and system balancing needs is not considered. In this chapter, the negative impact of wind power fluctuations on main grid is qualified, and a mileage-responsive receding horizon optimization method is proposed to optimize the dispatch command. The optimization is incorporated into real-time wind turbine control to mitigate the negative effect of wind power fluctuations.

This chapter is organized as follows. The smoothing reference generation is descripted in Section 5.1. To track the generated smoothing reference in real-time, the cascade control strategy for individual WT is presented in Section 5.2. Cased studies are shown in Section 5.3 to verify the effectiveness of the prosed smoothing framework. Section 5.4 summarizes this chapter.

5.1 Smoothing Reference Generation

5.1.1 Mileage Cost Derived from Regulation Market

Grid frequency stability is directly related with generation-demand balance. In systems normal operation, Automatic Generation Control (AGC) is typically responsible for maintaining grid frequency at its nominal value. With the high penetration of wind power, it becomes difficult to maintain the instantaneous generation-demand balance due to the stochastic nature of wind power. To counterbalance generation-demand balance, the fast-responding AGC units are encouraged to participate in regulation market. In this context, the concept of “mileage” is widely accepted by independent system operators

(ISO) in recent years. Mileage represents the sum of absolute changes in generation outputs spanning multiple control intervals in a given period [103]. It can be found that the AGC units earn profits by provide real-time regulation capacity, while the utility pay for such regulation service, which is referred to as mileage payment [104]. The calculation of mileage payment to AGC unit *m* at cycle *i* can be gained through the product of three terms (as reported in [105]), which can be expressed by,

$$\gamma_m(t) = |D_m(t) \cdot S_m(t) \cdot K_m(t)| \tag{5.1}$$

where $D_m(t)$ denotes the actual mileage. It can be defined as the active power injection or withdrawal in the course of following the AGC dispatch signal, as expressed as,

$$D_m(t) = P_{reg}^m(t) - P_{reg}^m(t-1) \tag{5.2}$$

where $P_{reg}^m(t)$ is the actual power output at control cycle *t*.

$S_m(t)$ in Eq. (5.1) is the mileage price, which is market-dependent. It is periodically cleared in the market based on the bid-in price and the historical performance of unit *m*.

$K_m(t)$ in Eq. (5.1) is the coefficient that reflects the general performance of unit *m* while following the dispatch signals. Different ISO adopt different methods to evaluate this coefficient [106]. In this thesis, $K_m(t)$ is determined via three variables: *regulation rate* k_1, *response delay* k_2 *and regulation precision* k_3. Specifically, the regulation rate quantifies the regulation rate of unit m in response to dispatch signal, which can be calculated by the deviation between the measured regulation rate and the standard regulation rate of the control area. The response relay quantifies the delay between the time that AGC signal is received and the time that the output power of unit m starts to change. It can be calculated as, k_2=1-response delay time/5min. The regulation precision is calculated through k_3=1- regulation error/maximum allowable error, where regulation error denotes the absolute deviation between the AGC signal and the actual output of unit m and the maximum allowable error is defined as 1.5% of the rated capacity of unit m. $K_m(t)$ can be determined via weighted linear combination of k_1, k_2 and k_3, i.e.

$$K_m(t) = a_1 k_1 + a_2 k_2 + a_3 k_3 \tag{5.3}$$

where a_1, a_2, and a_3 represent non-negative weights and satisfy $a_1 + a_2 + a_3 = 1$. Normally, the specific value is determined by the ISO. In this thesis, a_1=0.5, a_2=0.25, a_3=0.25.

5.1.2 Receding Horizon Optimization

To fulfil the system-accepted wind power smoothing task, the smoothing reference generation should not only focus on current operating point, the systems future operating points should be also taken into account. To this end, a model predictive control framework is developed. In a specified look-ahead time window (i.e. from present t_0 to future time instance t_T), the smoothing task is formulated as the following optimization problem.

$$\min\ -\alpha\sum_{t=t_0}^{t=t_T}\sum_{i=1}^{N}P_{Ei}^{t}/E_{\text{base}}^{wf}+(1-\alpha)\sum_{t=t_0}^{t=t_T}\sum_{i=1}^{n}(\gamma_t g_t^i)^2/(C_{\text{base}}^{\text{mileage}})^2 \tag{5.4}$$

where γ_t denotes mileage-based clearing price in regulation markets at time slot t, g_t^i represents the regulation power of AGC unit i at time slot t, E_{base}^{wf} and $C_{\text{base}}^{\text{mileage}}$ are base values for normalizing energy harvesting of the wind farm and mileage cost, respectively. P_{Ei}^{t} is the electric power output of the i-th WT at time slot t. P_{Ei}^{t} can be determined by two terms, where the first term is the mechanical power wind turbine captured from wind energy and the second term is the power converted from the kinetic energy stored in the rotating mass. It can be mathematically calculated using the following equation,

$$P_{Ei}^{t}=0.5\rho A{v_{ti}}^3C_{Pi}^{t}-J\omega_i(t)[\omega_i(t)-\omega_i(t-1)]/\Delta t \tag{5.5}$$

where ρ is air density, A is rotor swept area, v_t is wind speed, C_P is power coefficient, J is the equivalent moment of inertia of turbine blades and generator.

From the objective function (5.5), it can be found that the two independent normalized objectives, i.e. maximization of wind energy harvesting and minimization of wind fluctuations induced mileage cost, are integrated together through the weighted-sum strategy. The trade-off between these two objectives can be adjusted via the weighting coefficient α. The weights α can be chosen according to specific rationales set under different operating conditions. For example, under normal conditions, an unbiased weight can be set (i.e. α=0.5) as there is no preferences of maximizing wind energy harvesting and minimizing mileage cost. Under abnormal conditions, for example, system contingency occurs, a large weight α can be chosen to release regulation burden of AGC units. In general, a larger α results in a more smothered wind power output. In contrast, a smaller α results in a less wind fluctuation induced mileage cost. The selection of α should be determined according to AGC regulation pressure level and system reserve.

When quantifying the mileage cost, its clearing price γ_t is determined according to the specific market information that including bid-in regulation, mileage price and historical performance of AGC units [107]. Detailed price-clearing mechanism can be referred to [107].

According to Eq. (5.5), the power coefficient C_p modelling is important for wind energy harvesting calculation. In this chapter, the power coefficient is modelled by using the real data of a typical 5MW DFIG offshore wind turbine [100] from NREL. The data is widely studied and utilized in industry. And then, C_p is fitted through polynomial regression, of which the resulting parameters are listed in Table 5.1. Figure 5.1 shows the actual and fitted curve of C_p, respectively. The goodness-of-fit is evaluated and reported in Table 5.2 (i.e. mean absolute percentage error MAPE and root mean square error RMSE). Given such level of fitting precision, the fitted C_p can be directly used for the formulated optimization problem. In this connection, it can be verified that the polynomial regression gives rise to satisfactory modeling accuracy.

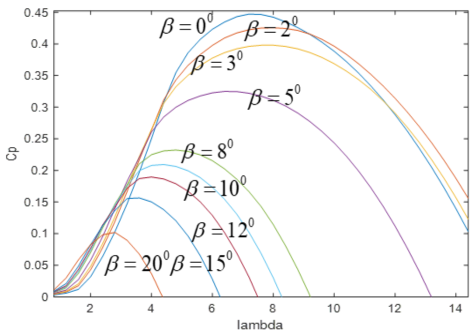

(a)

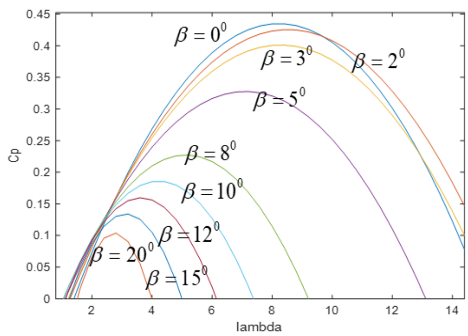

(b)

Fig. 5. 1 Cp curves with different ß (a) real curves; (b) fitted curves

Table 5. 1 Fitting parameters

model	$C_{Pi}^{t}=[c_{11}\beta_i(t)^2+c_{12}\beta_i(t)+c_{13}]\lambda_{ti}^2+[c_{21}\beta_i(t)^2+c_{22}\beta_i(t)+c_{23}]\lambda_{ti}+[c_{31}\beta_i(t)^2+c_{32}\beta_i(t)+c_{33}]$				
c11	-1.9543e-4	c21	0.0010	c31	-0.0015
c12	0.0010	c22	-0.0101	c32	0.0206
c13	-0.0094	c23	0.1538	c33	-0.1969

Table 5. 2 Goodness-of-fit evaluation

MAPE	0.1236
RMSE	0.1112

The second term in Eq. (5.5) lies in the conversion of KE storage. It can be found that the electric power output power of WT is extended via rotor speed acceleration/deceleration. In the situation that rotor speed is accelerated to its upper limit, the pitching blades activate. However, in the situation that rotor speed is decelerated to a value that is smaller than the value in MPP status, the small signal stability of the WT would be reduced [102]. In order to avoid this problem, when determining the electric output power reference, it should be subject to the following constraints,

$$0 \le P_{Ei}^{t} \le P_{MPPi}^{t} + P_{Ki} \tag{5.6}$$

where P_{MPPi}^{t} is the maximum mechanical power that captured from wind, P_{Ki} is the maximum power that can be converted KE release via rotor speed deceleration. To ensure that the over-deceleration can be avoided, P_{Ki} is mathematically expressed as,

$$P_{Ki} = 0.5J[\omega_i(t-1)^2 - \omega_{MPPi}(t)^2]/\Delta t \quad (5.7)$$

where ω_{MPP} denotes the rotor speed at MPP status.

In addition to the above-mentioned electric power output constraint, the WT should also be subject to the following practical constraints,

$$\omega_{\min} \le \omega_i(t) \le \omega_{\max} \quad (5.8)$$

$$\beta_{\min} \le \beta_i(t) \le \beta_{\max} \quad (5.9)$$

where $\omega_{\min}, \omega_{\max}, \beta_{\min}, \beta_{\max}$ denotes the maximum rotor speed, the maximum rotor speed, the maximum pitch angle and the maximum pitch angle respectively.

The AGC units take part in regulation market should be subject to the operational constraints,

$$D_m^{up}(t) = P_{reg\_up}^m(t) - P_{reg\_up}^m(t-1) \quad (5.10)$$

$$D_m^{down}(t) = P_{reg\_down}^m(t-1) - P_{reg\_down}^m(t) \quad (5.11)$$

$$0 \le P_{reg\_up}^m(t) \le P_{reg\_cap} \quad (5.12)$$

$$0 \le P_{reg\_down}^m(t) \le P_{reg\_cap} \quad (5.13)$$

where $D_m^{up}(t)/D_m^{down}(t)$ denotes the up/down regulation mileage of AGC unit *m*, $P_{reg\_up}^m(t)/P_{reg\_down}^m$ denotes the up/down regulation power of AGC unit *m*. The power balancing constraint of system should also be considered in real time operation.

$$P_{load}(t) - P_{wind}(t) = P_{schedule}(t) + \sum_{m=1}^{M}(D_m^{up}(t) - D_m^{down}(t)) \tag{5.14}$$

where $P_{schedule}(t)$ is the scheduled power generation in power grid at time slot t $P_{load}(t)$ is the instantaneous system load demand at time slot t, $P_{wind}(t)$ is the power generation of wind farm at time slot t.

5.2 Cascade Control Strategy for Individual Wind Turbine

The generation cycle of the smoothing reference is identical with the AGC cycle. Once the smoothing reference is generated via the receding horizon optimization module, the smoothing command should be real-timely tracked by the WTs. Consequently, as shown in Fig. 5.2, the optimization module and WT control module are closely coupled and mutually influenced.

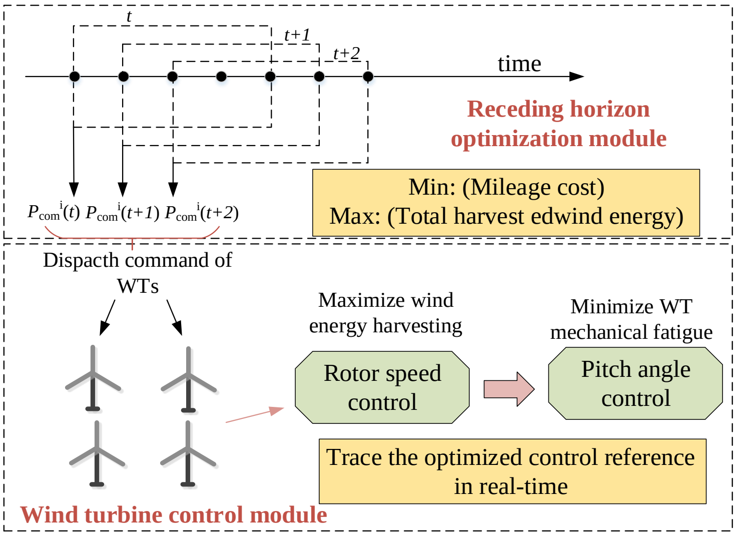

Fig. 5. 2 The proposed mileage-inspired wind power smoothing control framework

In this section, a cascade control is designed to fulfil the smoothing reference, in which the rotor speed control has a high activation list and the pitching control will complement the power smoothing task, the detailed information can be seen in Fig. 5.3. Since the accessional energy storage systems are not adopted in this thesis, the self-capability of DFIG-based WTs are made full use of to regulate output power. Broadly speaking, the DC-link capacitor capacity of DFIG-based WTs is significantly less than the capacitance of PMSG-based WTs. Hence the rotor speed control and pitching control are sequentially adopted to fulfil the command.

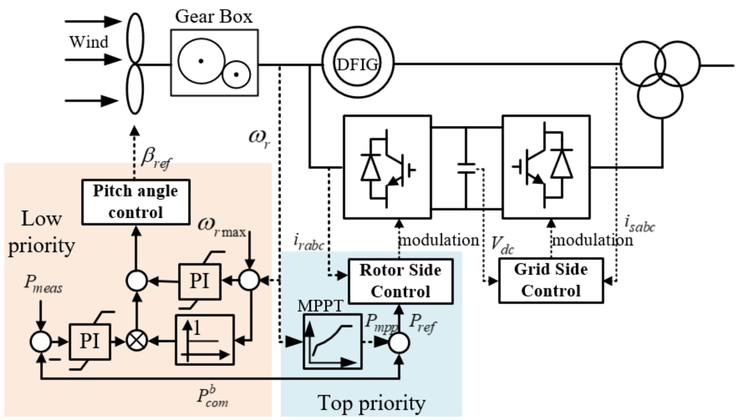

Fig. 5. 3 Proposed cascade control for wind power smoothing

The rotating mass of WT system is utilized at the top priority to build up a “energy buffer”. In this context, the excessive energy can be stored timely in deloading situation and released back to system in overloading situation. As formulated in Section 5.1, the smoothing objective is to maximize wind energy harvesting and minimize the fluctuation induced mileage cost, which amounts to enhancing the energy buffer as much as possible. This is because the sufficient “energy buffer” can greatly support WT overloading/deloading to effectively track the optimal smoothing references. Consistently, a cascade control strategy (as illustrated in Fig. 5.3) is devised on the WT level by following the control priority from rotor speed control to pitch angle control. The proposed cascade control has the following merits: 1) Energy harvesting efficiency would be increased by utilizing the rotating mass to store/release extra energy; 2) WT system wear outs would be mitigated as pitch angle control for power curtailment is placed at the lowest priority.

Once WTs operate at the power smoothing mode, the rotational speed is usually higher than MPPT mode. There is a concern that the mechanical loss would be increase. While according to [108], the mechanical loss (i.e. the bearing loss and windage loss) related to the rotational speed only accounts for 2%-3% of the total losses in a WT. Since this loss is minor, the control cost is not included when calculating the total wind energy production and the mileage cost.

5.3 Case Studies

5.3.1 Experimental Setup

To demonstrate the effectiveness of the proposed power smoothing control scheme, a test system that consists 3 AGC units, a wind farm with 4 homogenous DFIG wind turbines and time varying load is constructed as shown in Fig. 5.4.

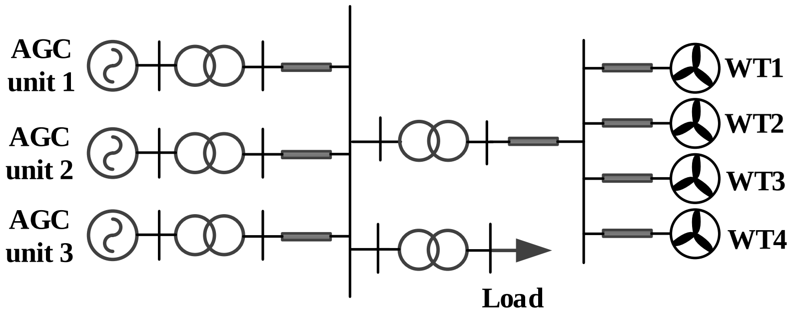

Fig. 5. 4 Configuration of the testing system

In the testing system, the power imbalance between scheduled energy and net load is complemented by AGC units. As shown in Fig. 5.5, the shaded area denotes the regulation mileage. With the implementation of the proposed smoothing method, the shadow area in Fig. 5.5 could be reduce. Simulation parameters are predefined as shown in Table 5.2. The price clearing mechanism can be referred to [107].

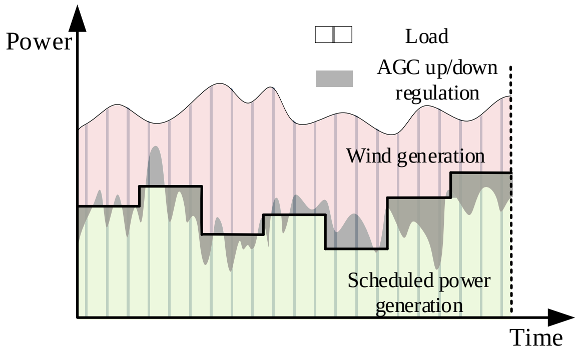

Fig. 5. 5 Schematic diagram of power balance in wind embedded power systems

Table 5. 3 System parameters

AGC	p_m: normalized regulation performance score P^i_{offer} : mileage bidding price of unit i (\$/MW) g^i_{cap} : maximum biddable capacity of unit i (MW)
	$p^1_m = 0.7168$ $\quad P^1_{offer} = 2\$/MW$ $\quad g^1_{cap} = 1.5$
	$p^2_m = 0.6074$ $\quad P^2_{offer} = 4\$/MW$ $\quad g^2_{cap} = 4$
	$p^3_m = 1$ $\quad P^3_{offer} = 1\$/MW$ $\quad g^3_{cap} = 2.5$
Wind speed data	Online accessible [109]
Wind farm	The studied wind farm consists of 4 homogeneous NREL 5MW DFIG wind turbines [100] whose total nominal capacity is 20 MW.

In the case study, 1 hour time series of wind speed is considered, as shown in Fig. 5.6. It is assumed that all WTs in the studied wind farm are exposed to the same wind speed. The update cycle of the smoothing command is consistent with ACG control cycle, which means the formulated non-linear optimization problem should be solved every 4 seconds. The lookahead time window of the receding horizon optimization is set to be 20s, during which the wind speed prediction accuracy can be satisfactorily high. In this case study, the optimization part can be readily solved in 0.2732s (this computation time is averaged by 10000 individual simulations based on Dell Precision Tower with CPU E5-2650 v4@2.20GHz (2 processors)).

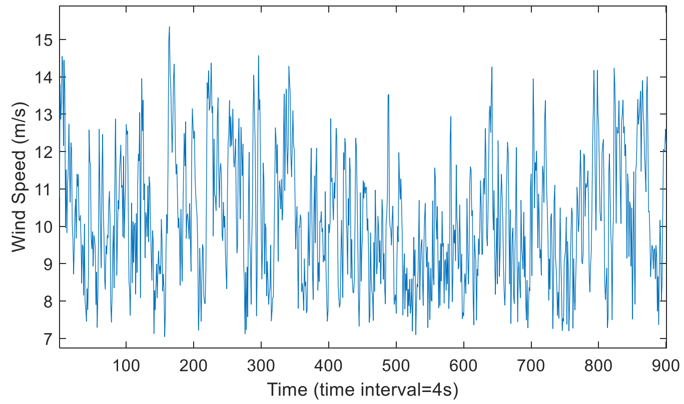

Fig. 5. 6 Wind speed

5.3.2 Wind Power Smoothing Performance

It should be noted that the overall smoothing performance is influenced by different weights applied to wind energy harvesting and mileage cost. To investigate the trade-off between maximizing wind energy harvesting and minimizing wind fluctuation induced mileage cost, different α setting is compared for time-domain simulations.

The energy yield from the wind farm can be expressed as,

$$E = \int_{t_0}^{t_T} \sum_{i=1}^{N} (P_{wti} + P_{ki}) dt \tag{5.15}$$

To make a quantitative comparison, the total energy yield of the wind farm is calculated using a sample time of 1 second. According to Fig. 5.7(a), for

$\alpha = 1$, corresponding to maximum energy yield without smoothing out power fluctuations, the total captured wind energy is 9.519×10^3kWh. The energy yield calculation is repeated for varying α from 1 to 0.7, 0.5, and 0.3. Not surprisingly, it can be found that the corresponding wind energy yields are reduced to 8.889×10^3kWh, 8.443×10^3 kWh, 8.192×10^3kWh, which can be seen in Fig. 5. 7(a-c). As demonstrated in simulation results, the decrease of α serves the aim to allow a reduction of energy yield to smooth wind power fluctuations. Thereafter, the mileage cost is lowered down. The detailed wind energy harvesting and wind power fluctuation induced mileage cost are reposted in Table 5.4. To make a quantitative comparison, it can be found that the total mileage cost without smoothing control implementation is 1.1708×10^4\$. The mileage cost is reduced to 2.68×10^3\$, 2.64×10^3\$, 2.61×10^3\$ by lowering down weight α to 0.7, 0.5 and 0.3 respectively. It proves that even though a certain amount of energy loss is brought about by the smoothing control, there is significant potential for reducing mileage cost induced by wind fluctuations. By comparison, it is easy to conclude that the lower α settings increases the energy loss to achieve the target of lessening mileage cost. In practice, the selection of α is dependent on the practical requirements of the trade-off between energy yield and mileage regulation payment.

To track the optimized smoothing command, the KE based rotor speed control and pitching based control activates in the predefined cascading manner as shown in Fig. 5(d, e). As exhibited, when over-generation event happens, a portion of the energy is primarily converted to KE via rotor speed acceleration to deliver less electric power to system. In the case that the KE is charged full, pitch angle control initiates to limit power production. As illustrated before, a low α indicates that a lower mileage cost is expected and accordingly a better wind power smoothing effect is required. Not surprisingly, simulation results show that the activation frequency of pitch angle increases along with the decrease of α to achieve the smoothing requirement. To make a quantitative comparison, we compare the total activation time of the pitch angle control throughout the simulation period. In the case that when no smoothing control is applied, the total blade pitch angle activation time of a WT is 157s. For cases $\alpha = 0.7, 0.5, \text{and } 0.3$ respectively, the total activation time of pitch angle control increases to 376s, 606s and 700s. Apparently, lower α pushes the activation of pitch angle control to follow the more strictly smoothing command. When under-generation event occurs and more power production is expected from the wind farm, the stored KE is released back to system via rotor speed deceleration. The proposed cascading control ensures that the overloading potential of the WT is fully utilized via making efficient use of KE in turbines. It is worth noting that over-deceleration is avoided as the discharging range of the KE is real-time evaluated (refer to Eq (5.6)). In conclusion, the smoothing command optimized by the receding horizon control can be followed accurately and rapidly with the coordination of rotor speed control and pitch angle control.

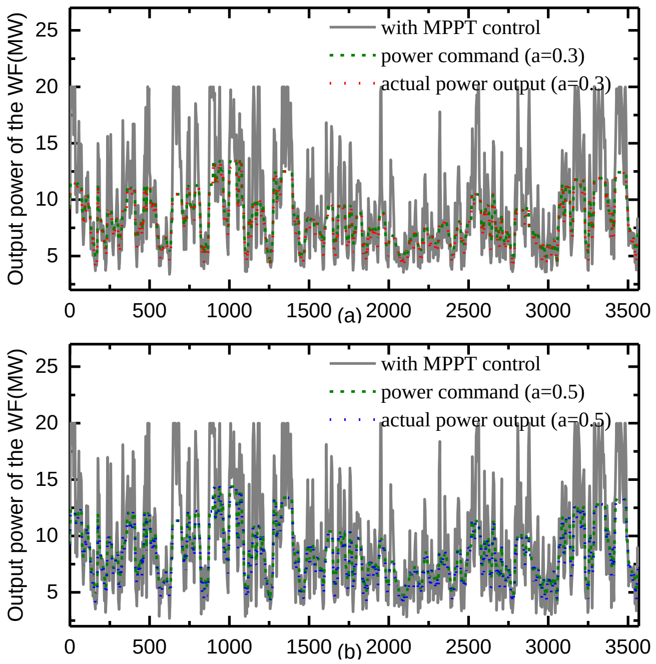

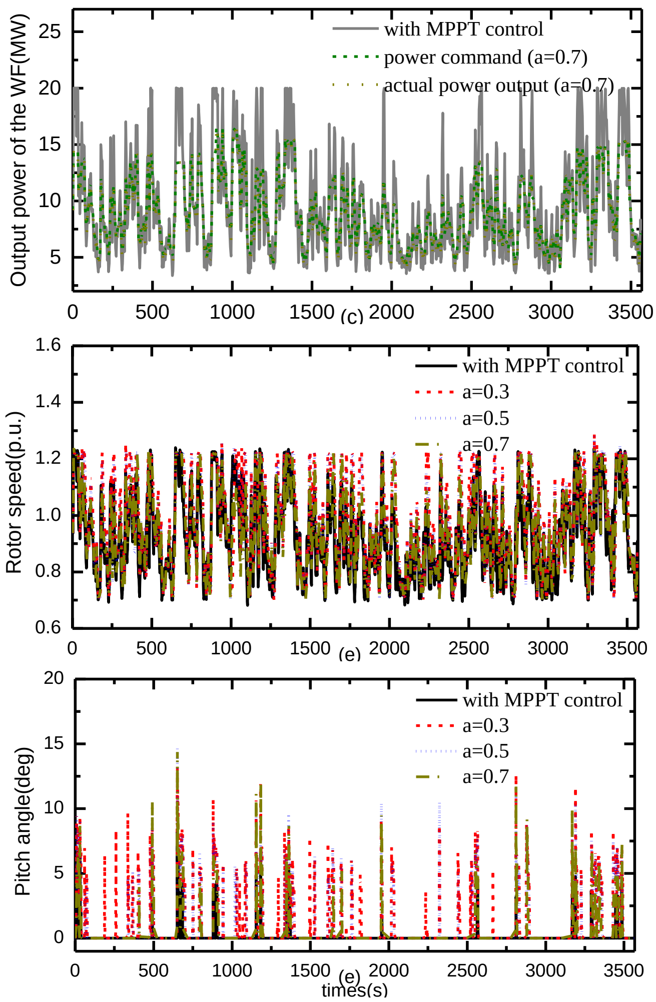

Fig. 0.1 Smoothing results with the proposed strategy (a) Output power of the WF with α =0.3, (b) Output power of the WF with α =0.5, (c) Output power of the WF with α =0.7, (d) Rotor speed of the WT, (e) Pitch angle of the WT

Table 5. 4 Simulation results (for 1 hour) obtained by different weighting factors

		Wind energy production (kWh)	Mileage cost ($)
Proposed method	α=0.3	8.192×10^3	2.61×10^3
	α=0.5	8.443×10^3	2.64×10^3
	α=0.7	8.889×10^3	2.68×10^3
MPPT		9.519×10^3	1.1708×10^4

5.4 Summary

This chapter newly proposes an optimal wind power smoothing control paradigm from the perspective of system operation. At the upper optimization level, a receding horizon control scheme is adopted to generate the optimal smoothing reference by taking wind-fluctuation-induced mileage cost and wind power production into consideration simultaneously. At the lower WTs control level, the potential of WTs making use of its KE stored in the rotational rotor and pitch angle adjustment capability to expand power generation range is adequately explored. The effectiveness of the proposed control strategy is successfully tested through case studies. It is highlighted that the proposed system-oriented smoothing control has the advantage on ensuring genuinely smoothed operation of WTs subject to various constraints.

Chapter 6 Conclusions and Future Scope

6.1 Conclusions

Variable renewable energies, such as wind energy and solar energy, would become major power resources in the future. With the reduction of costs of wind and solar technologies, the large-scale deployment of solar power and wind power has occurred all over the world. Currently, the annual renewable energy penetration level in countries like Denmark, Ireland and Germany is higher than 20%. Different from thermal generators, power production of wind and solar system is variable and uncertain as they are determined by local weather conditions. Consequently, PV generators and wind turbines are non-dispatchable units from system perspective as they cannot adjust their power generation to meet changes in demand. With the increasing penetration of solar power and wind power, many operation challenges are brought along associated with their uncontrollable nature. Under this background, it is necessary to develop advanced control strategies to change the uncontrollable nature of solar and wind systems. In this way the renewable penetration limits within the system can be improved.

This thesis endeavors to design effective control strategies for solar and wind systems to enable them to no longer operate at the “free-running” mode and to provide ancillary service for system operation. The main conclusions and contributions of this thesis are summed up as follows.

1. ***A simultaneous DC-link voltage control and droop control of two-stage PV systems for providing frequency response:*** A novel frequency control strategy is proposed for two-stage PV system. Specifically, the energy stored in the DC-link capacitor is utilized to contribute inertia. In addition, a deloading control strategy is applied to offer power reserve for primary frequency response. In addition, considering that the reserve capacity of the solar system is directly related to environment conditions (i.e. temperature and irradiance), the droop gain is adaptively changed according to the reserve capacity. Accordingly, solar PV can significantly improve system dynamic frequency behavior. This will largely relieve the burden to traditional generators and help to stabilize system frequency of future grids with reduced inertia.
2. ***A hierarchical control strategy of PMSG-WTs for active power regulation:*** An active power regulation strategy of PMSG-WTs that coordinate the individual DC-link voltage control, rotor speed control and pitch angle control in a hierarchical manner is proposed. All the active power regulation resources (i.e. DC-link capacitor, rotational rotor and blade pitch adjustment capability) are adequately exploited in the proposed control scheme. To optimally trace the dispatch command, a response priority of each controller is predetermined via taking their own characteristic into consideration. The active power regulation task allocation of each controller is assigned based on their response priority and their regulation capability. The energy harvesting efficiency can be improved and the mechanical stress of the WT

can be mitigated while fulfilling the dispatch command with the proposed control scheme.

3. ***An active power regulation strategy of wind farm considering the wake effect:*** An active power regulation strategy is proposed to enable wind farm to follow the dispatch command, which inherently takes wake effect into account. Due to the influence wake interactions, the operation status of WTs in different locations are different from each other. Accordingly, their active power regulation capabilities though rotor speed control and blade pitch angle control are different. To improve the total energy harvesting capability and to reduce the mechanical stress of the WTs, different response priority is determined for WTs in different rows. In addition, a KE storage estimation module is set up to adequately exploit the variable rotor speed range as a buffer in deloading situation and to guarantee WTs stable operation in overloading situation. The regulation task of individual WTs is assigned according to its response priority and its available KE charging/discharging range. The WF becomes a dispatchable resource with the implementation of the proposed strategy.
4. ***A mileage-inspired wind power smoothing control:*** An optimal wind power smoothing control scheme is proposed, which incorporates two objectives (i.e. maximizing wind farm power generation and minimizing AGC mileage cost) together. From the system perspective, a mileage-inspired receding horizon control is developed to properly assess the consequence induced by wind power fluctuations Compared with other

smoothing control strategies, whose smoothing reference are typically generated by hard-coded algorithms (e.g. moving average, low-pass filer, ramping limits, etc.), the proposed control strategy has the following advantages: 1) the smoothing reference is closely correlated with system needs. Therefore, the obtained smoothing power can be beneficial to power system is questionable; 2) the wind turbine operational constraints are taken into account such that obtained control references is practically effective in terms of over-/under-production demand; and 3) the computational efficiency of the formulated optimization is satisfactorily high.

6.2 Future Scope

This thesis dedicates to provide several effective control strategies to enable renewable systems to provide system ancillary service, e.g. frequency regulation, following system dispatch command and smoothing out power fluctuations. There is a lot of work needed to be further studied in the future, and the research perspectives are outlined as follows,

1. ***Frequency regulation strategy of the WF considering wake effect:*** Recently, aggregated WT models are generally adopted in research work about wind farm frequency regulation. However, the actual frequency regulation contribution from the WF needs to be further investigated due to the wake interactions. Specifically, when a certain amount of power reserve of the WF is required, the deloading level and the deloading approach of individual WTs should be determined with taking the mutual influence of wind turbines into account. For example, at the wind farm control level, an

optimization algorithm should be applied to find the optimal operation state of each WT to obtain the required deloading level and to achieve the objective of maximizing total KE storage. In addition, the virtual inertia gain and the droop gain should also be optimized to optimally provide frequency response. However, it should be noted that the formulated optimization problem is non-linear and non-convex due to the complexity and nonlinearity involved in the wake effect model. How to compromise the modelling accuracy and solution quality is a challenge issue and need to be handled in future work.

2. ***Power regulation scheme for the renewables in a performance based balancing market***: In recent years, some grid codes require that the renewables should no longer operate at the “free-running mode”. For example, as required e.g. in Danish grid code [110], the power production of the wind farm shall be regulated so as to maintain the power balance of the balance responsible market player and/or the system operators. Under this background, downward or upward power generation of renewables should be instantly and suitably available. In a performance based market, the renewables could receive subsidies for energy generation and bare certain share of balancing cost for power fluctuations. The system operational status and the balancing market should be both comprehensively considered to maximize the total revenue of the wind/solar farm. To this end, an optimal power regulation scheme for renewables can be proposed.

It is worth noting that it is challenging to determine the share of the balancing cost of renewables and is worth in-depth study.

3. ***Power regulation of renewables considering forecast uncertainty***: When developing the optimal regulation scheme for renewables under a performance based market, as illustrated in the second research perspective, the forecasting information of renewables is necessary. However, it should be noted that the forecast information is not 100% accurate. In such a context, how to manage the uncertainty and to ensure the optimality of the proposed control scheme is a challenging issue to be handled. Especially for wind turbines, as is known that an inappropriate control reference allocation could lead to WTs' unstable operation or WTs' trip off. How to guarantee the stability of the wind energy conversion system in the proposed optimal control scheme is an essential issue to be addressed.

Appendix

A. Parameter of studied PV system

Table A. Paramater1 of PV system in Chapter 2

Item	Value
Open-circuit voltage	43.8V
Short-circuit current	5A
Maximum power voltage(STC)	35V
Maximum power current(STC)	4.58A
Maximum power (STC)	160kW
Series number	20
Parallel number	50
DC-link voltage	1.15kV
DC-link capacitor	30000 μF

B. Parameter of the studied wind turbines

Table B. 1 Parameters of the PMSG-WT in Chapter 3

Symbol	ITEM	Value
V_{rated}	Rated wind speed	14m/s
T_b	Time constant of the pitch serve	0.5 s
J_{tur}	Turbine inertia	6100000kgm^2
R	Rotor blade radius	30m
P_{rated}	Rated power	1.5 MW
U_g	Terminal Voltage	3.3 kV
J_{gen}	Generator inertia	130kgm^2
C	Capacitance of DC-link capacitor	0.075F
$U_{dcrated}$	Rated DC-link voltage	7.1kV

Table B. 2 Parameter of the DFIG-WT in Chapter 4 and Chapter 5

Symbol	ITEM	Value
T_b	Time constant of the pitch serve	0.5 s
H	Inertia constant	4s
P_{rated}	Rated power	5 MW
U_g	Terminal Voltage	3.3 kV
C	Capacitance of DC-link capacitor	4813μF
$U_{dcrated}$	Rated DC-link voltage	1.15kV
ω_{rmin}	Lower limit of rotor speed	0.7p.u.
ω_{rmax}	Upper limit of rotor speed	1.22p.u

C. Parameters of the studied SGs

Table C. 1 Parameters of the SG in Chapter 2 and Chapter 3

Item	Value
Rated MVA	4.9MVA
Power factor	0.8
Terminal voltage	10kV
Inertia time constant	2.5s
Droop parameter	4%
Governor time constant	0.3s
Servo time constant	11.88s
Exciter regulation gain	400
Exciter time constant	0.01s

Table C. 2 Parameters of SGs in Chapter 4

Symbol	ITEM	Value
S_{g1}	Rated MVA	90MVA
S_{g2}	Rated MVA	30MVA
U_g	Terminal Voltage	30 kV
H_{g1}	Inertia Time constant	8.7s
H_{g2}	Inertia Time constant	4s
R_P	Turbine permanent droop	0.04
T_r	Governor time constant	8.408s
T_{servo}	Servo-motor time constant	0.5s
K_{gain}	Exciter regulator gain	400
T_e	Exciter time constant	0.01s

Reference

[1] Q. Cao, Y.-D. Song, J. M. Guerrero, and S. Tian, "Coordinated control for flywheel energy storage matrix systems for wind farm based on charging/discharging ratio consensus algorithms," *IEEE Transactions on Smart Grid,* vol. 7, no. 3, pp. 1259-1267, 2016.

[2] B.-I. Crăciun, T. Kerekes, D. Séra, and R. Teodorescu, "Frequency support functions in large PV power plants with active power reserves," *IEEE Journal of Emerging and Selected Topics in Power Electronics,* vol. 2, no. 4, pp. 849-858, 2014.

[3] E.-E. ENTSO-E, "Network Code for Requirements for Grid Connection Applicable to all Generators (NC RfG), March 2013," ed.

[4] H.-Q. TransÉnergie, "Transmission Provider Technical Requirements for the connection of power plants to the Hydro-Québec Transmission System," *Montréal, QC, Canada*, 2009.

[5] D. Gautam, L. Goel, R. Ayyanar, V. Vittal, and T. Harbour, "Control strategy to mitigate the impact of reduced inertia due to doubly fed induction generators on large power systems," *IEEE Transactions on Power Systems*, vol. 26, no. 1, pp. 214-224, 2011.

[6] M. Kayikçi and J. V. Milanovic, "Dynamic contribution of DFIG-based wind plants to system frequency disturbances," *IEEE Transactions on Power Systems,* vol. 24, no. 2, pp. 859-867, 2009.

[7] J. Van de Vyver, J. D. De Kooning, B. Meersman, L. Vandevelde, and T. L. Vandoorn, "Droop control as an alternative inertial response strategy for the synthetic inertia on wind turbines," *IEEE Transactions on Power Systems,* vol. 31, no. 2, pp. 1129-1138, 2016.

[8] Y. Li, Z. Xu, and K. Meng, "Optimal power sharing control of wind turbines," *IEEE Transactions on Power Systems,* vol. 32, no. 1, pp. 824-825, 2017.

[9] Y. Li, Z. Xu, and K. P. Wong, "Advanced control strategies of PMSG-based wind turbines for system inertia support," *IEEE Transactions on Power Systems,* vol. 32, no. 4, pp. 3027-3037, 2017.

[10] J. Zhao, X. Lyu, Y. Fu, X. Hu, and F. Li, "Coordinated microgrid frequency regulation based on DFIG variable coefficient using virtual inertia and primary frequency control," *IEEE Transactions on Energy Conversion,* vol. 31, no. 3, pp. 833-845, 2016.

[11] E. P. I. Association, "Connecting the Sun: Solar photovoltaics on the road to large-scale grid integration," *Online], Sept*, 2012.

[12] P. Tielens and D. Van Hertem, "Grid inertia and frequency control in power systems with high penetration of renewables," 2012.

[13] A. Uehara *et al.*, "A coordinated control method to smooth wind power fluctuations of a PMSG-based WECS," *IEEE Transactions on energy conversion,* vol. 26, no. 2, pp. 550-558, 2011.

[14] M. F. M. Arani and E. F. El-Saadany, "Implementing virtual inertia in DFIG-based wind power generation," *IEEE Transactions on Power Systems*, vol. 28, no. 2, pp. 1373-1384, 2013.

[15] S. Adhikari and F. Li, "Coordinated Vf and PQ control of solar photovoltaic generators with MPPT and battery storage in microgrids," *IEEE Transactions on Smart Grid*, vol. 5, no. 3, pp. 1270-1281, 2014.

[16] C. A. Hill, M. C. Such, D. Chen, J. Gonzalez, and W. M. Grady, "Battery energy storage for enabling integration of distributed solar power generation," *IEEE Transactions on smart grid*, vol. 3, no. 2, pp. 850-857, 2012.

[17] N. Kakimoto, S. Takayama, H. Satoh, and K. Nakamura, "Power modulation of photovoltaic generator for frequency control of power system," *IEEE Transactions on Energy Conversion*, vol. 24, no. 4, pp. 943-949, 2009.

[18] K. O. Oureilidis, E. A. Bakirtzis, and C. S. Demoulias, "Frequency-based control of islanded microgrid with renewable energy sources and energy storage," *Journal of Modern Power Systems and Clean Energy*, vol. 4, no. 1, pp. 54-62, 2016.

[19] D. Wu, F. Tang, T. Dragicevic, J. C. Vasquez, and J. M. Guerrero, "Autonomous active power control for islanded ac microgrids with photovoltaic generation and energy storage system," *IEEE Transactions on energy conversion*, vol. 29, no. 4, pp. 882-892, 2014.

[20] A. Hoke, M. Shirazi, S. Chakraborty, E. Muljadi, and D. Maksimovic, "Rapid Active Power Control of Photovoltaic Systems for Grid Frequency Support," *IEEE Journal of Emerging and Selected Topics in Power Electronics*, 2017.

[21] C. Rahmann, V. Vittal, J. Ascui, and J. Haas, "Mitigation control against partial shading effects in large-scale PV power plants," *IEEE Transactions on Sustainable Energy*, vol. 7, no. 1, pp. 173-180, 2016.

[22] P. Zarina, S. Mishra, and P. Sekhar, "Exploring frequency control capability of a PV system in a hybrid PV-rotating machine-without storage system," *International Journal of Electrical Power & Energy Systems*, vol. 60, pp. 258-267, 2014.

[23] P. Moutis, A. Vassilakis, A. Sampani, and N. Hatziargyriou, "DC switch driven active power output control of photovoltaic inverters for the provision of frequency regulation," *IEEE Transactions on Sustainable Energy*, vol. 6, no. 4, pp. 1485-1493, 2015.

[24] H. Xin, Y. Liu, Z. Wang, D. Gan, and T. Yang, "A new frequency regulation strategy for photovoltaic systems without energy storage," *IEEE Transactions on Sustainable Energy*, vol. 4, no. 4, pp. 985-993, 2013.

[25] A. Okou, O. Akhrif, R. Beguenane, and M. Tarbouchi, "Nonlinear control strategy insuring contribution of PV generator to voltage and frequency regulation," 2012.

[26] E. I. Batzelis, G. E. Kampitsis, and S. A. Papathanassiou, "Power reserves control for PV systems with real-time MPP estimation via curve fitting," *IEEE Transactions on Sustainable Energy*, vol. 8, no. 3, pp. 1269-1280, 2017.

[27] H. Polinder, F. F. Van der Pijl, G.-J. De Vilder, and P. J. Tavner, "Comparison of direct-drive and geared generator concepts for wind turbines," *IEEE Transactions on energy conversion*, vol. 21, no. 3, pp. 725-733, 2006.

[28] R. M. Kamel, A. Chaouachi, and K. Nagasaka, "Three control strategies to improve the microgrid transient dynamic response during isolated mode: A comparative study," *IEEE Transactions on Industrial Electronics*, vol. 60, no. 4, pp. 1314-1322, 2013.

[29] P. Moutis, S. A. Papathanassiou, and N. D. Hatziargyriou, "Improved load-frequency control contribution of variable speed variable pitch wind generators," *Renewable Energy,* vol. 48, pp. 514-523, 2012.

[30] E. Valsera-Naranjo, A. Sumper, O. Gomis-Bellmunt, A. Junyent-Ferré, and M. Martínez-Rojas, "Pitch control system design to improve frequency response capability of fixed-speed wind turbine systems," *International Transactions on Electrical Energy Systems,* vol. 21, no. 7, pp. 1984-2006, 2011.

[31] M. Chowdhury, N. Hosseinzadeh, and W. Shen, "Smoothing wind power fluctuations by fuzzy logic pitch angle controller," *Renewable Energy,* vol. 38, no. 1, pp. 224-233, 2012.

[32] T. Senjyu, R. Sakamoto, N. Urasaki, T. Funabashi, H. Fujita, and H. Sekine, "Output power leveling of wind turbine generator for all operating regions by pitch angle control," *IEEE Transactions on Energy conversion,* vol. 21, no. 2, pp. 467-475, 2006.

[33] X. Tang, M. Yin, C. Shen, Y. Xu, Z. Y. Dong, and Y. Zou, "Active Power Control of Wind Turbine Generators via Coordinated Rotor Speed and Pitch Angle Regulation," *IEEE Transactions on Sustainable Energy,* 2018.

[34] J. Van de Vyver, J. D. De Kooning, B. Meersman, L. Vandevelde, and T. L. Vandoorn, "Droop control as an alternative inertial response strategy for the synthetic inertia on wind turbines," *IEEE Trans. Power Syst,* vol. 31, no. 2, pp. 1129-1138, 2016.

[35] D. Ochoa and S. Martinez, "Fast-Frequency Response provided by DFIG-Wind Turbines and its impact on the grid," *IEEE Trans. Power Syst,* vol. 32, pp. 4002-4011, 2017.

[36] J. M. Mauricio, A. Marano, A. Gómez-Expósito, and J. L. M. Ramos, "Frequency regulation contribution through variable-speed wind energy conversion systems," *IEEE Transactions on Power Systems*, vol. 24, no. 1, pp. 173-180, 2009.

[37] P.-K. Keung, P. Li, H. Banakar, and B. T. Ooi, "Kinetic energy of wind-turbine generators for system frequency support," *IEEE Transactions on Power Systems,* vol. 24, no. 1, pp. 279-287, 2009.

[38] J. Morren, S. W. De Haan, W. L. Kling, and J. Ferreira, "Wind turbines emulating inertia and supporting primary frequency control," *IEEE Transactions on power systems,* vol. 21, no. 1, pp. 433-434, 2006.

[39] A. M. Howlader, N. Urasaki, T. Senjyu, A. Uehara, A. Yona, and A. Saber, "Output power smoothing of wind turbine generation system for the 2-MW permanent magnet synchronous generators," in *Electrical Machines and Systems (ICEMS), 2010 International Conference on*, 2010, pp. 452-457: IEEE.

[40] Y. Kim, M. Kang, E. Muljadi, J.-W. Park, and Y. C. Kang, "Power Smoothing of a Variable-Speed Wind Turbine Generator in Association With the Rotor-Speed-Dependent Gain," *IEEE Transactions on Sustainable Energy,* vol. 8, no. 3, pp. 990-999, 2017.

[41] S. G. Varzaneh, G. Gharehpetian, and M. Abedi, "Output power smoothing of variable speed wind farms using rotor-inertia," *Electric Power Systems Research*, vol. 116, pp. 208-217, 2014.
[42] G. Diaz, P. G. Casielles, and C. Viescas, "Proposal for optimising the provision of inertial response reserve of variable-speed wind generators," *IET Renewable Power Generation*, vol. 7, no. 3, pp. 225-234, 2013.
[43] Y. Kim, M. Kang, E. Muljadi, J.-W. Park, and Y. C. Kang, "Power smoothing of a variable-speed wind turbine generator in association with the rotor speed–dependent gain," *IEEE Trans. Sustain. Energy*, vol. 8, no. 3, pp. 990-1000, 2017.
[44] S. Wang, J. Hu, X. Yuan, and L. Sun, "On inertial dynamics of virtual-synchronous-controlled DFIG-based wind turbines," *IEEE Trans. Energy Convers*, vol. 30, no. 4, pp. 1691-1702, 2015.
[45] H. Ye, W. Pei, and Z. Qi, "Analytical modeling of inertial and droop responses from a wind farm for short-term frequency regulation in power systems," *IEEE Transactions on Power Systems*, vol. 31, no. 5, pp. 3414-3423, 2016.
[46] S. Wang and K. Tomsovic, "A Novel Active Power Control Framework for Wind Turbine Generators to Improve Frequency Response," *IEEE Transactions on Power Systems*, 2018.
[47] Y. Zhang, A. Melin, S. M. Djouadi, M. Olama, and K. Tomsovic, "Provision for guaranteed inertial response in diesel-wind systems via model reference control," *IEEE Transactions on Power Systems*, 2018.
[48] A. M. Howlader, T. Senjyu, and A. Y. Saber, "An integrated power smoothing control for a grid-interactive wind farm considering wake effects," *IEEE Systems Journal*, vol. 9, no. 3, pp. 954-965, 2015.
[49] J. Zhu, C. D. Booth, G. P. Adam, A. J. Roscoe, and C. G. Bright, "Inertia emulation control strategy for VSC-HVDC transmission systems," *IEEE Trans. Power Syst*, vol. 28, no. 2, pp. 1277-1287, 2013.
[50] J. Zhu *et al.*, "Synthetic Inertia Control Strategy for Doubly Fed Induction Generator Wind Turbine Generators Using Lithium-Ion Supercapacitors," *IEEE Transactions on Energy Conversion*, vol. 33, no. 2, pp. 773-783, 2018.
[51] W. Zhang, Y. Xu, W. Liu, F. Ferrese, and L. Liu, "Fully distributed coordination of multiple DFIGs in a microgrid for load sharing," *IEEE Transactions on Smart Grid*, vol. 4, no. 2, pp. 806-815, 2013.
[52] P. Kou, D. Liang, and L. Gao, "Distributed coordination of multiple PMSGs in an islanded DC microgrid for load sharing," *IEEE Transactions on Energy Conversion*, vol. 32, no. 2, pp. 471-485, 2017.
[53] H. Wang, Z. Chen, and Q. Jiang, "Optimal control method for wind farm to support temporary primary frequency control with minimised wind energy cost," *IET Renewable Power Generation*, vol. 9, no. 4, pp. 350-359, 2014.
[54] Z. Wang and W. Wu, "Coordinated Control Method for DFIG-Based Wind Farm to Provide Primary Frequency Regulation Service," *IEEE Transactions on Power Systems*, vol. 33, no. 3, pp. 2644-2659, 2018.
[55] H. Zhao, Q. Wu, Q. Guo, H. Sun, and Y. Xue, "Distributed model predictive control of a wind farm for optimal active power controlpart II: Implementation

with clustering-based piece-wise affine wind turbine model," *IEEE transactions on sustainable energy,* vol. 6, no. 3, pp. 840-849, 2015.

[56] J. Park and K. H. Law, "A data-driven, cooperative wind farm control to maximize the total power production," *Applied Energy,* vol. 165, pp. 151-165, 2016.

[57] J. R. Marden, S. D. Ruben, and L. Y. Pao, "A model-free approach to wind farm control using game theoretic methods," *IEEE Transactions on Control Systems Technology,* vol. 21, no. 4, pp. 1207-1214, 2013.

[58] J. S. González, M. B. Payán, J. R. Santos, and Á. G. G. Rodríguez, "Maximizing the overall production of wind farms by setting the individual operating point of wind turbines," *Renewable Energy,* vol. 80, pp. 219-229, 2015.

[59] N. Gionfra, G. Sandou, H. Siguerdidjane, D. Faille, and P. Loevenbruck, "Wind farm distributed PSO-based control for constrained power generation maximization," *Renewable Energy,* 2018.

[60] B. Zhang, M. Soltani, W. Hu, P. Hou, Q. Huang, and Z. Chen, "Optimized power dispatch in wind farms for power maximizing considering fatigue loads," *IEEE Transactions on Sustainable Energy,* vol. 9, no. 2, pp. 862-871, 2018.

[61] T. Knudsen, T. Bak, and M. Svenstrup, "Survey of wind farm control—power and fatigue optimization," *Wind Energy,* vol. 18, no. 8, pp. 1333-1351, 2015.

[62] A. S. Ahmadyar and G. Verbič, "Coordinated operation strategy of wind farms for frequency control by exploring wake interaction," *IEEE Transactions on Sustainable Energy,* vol. 8, no. 1, pp. 230-238, 2017.

[63] S. Ma, H. Geng, G. Yang, and B. C. Pal, "Clustering based Coordinated Control of Large Scale Wind Farm for Power System Frequency Support," *IEEE Transactions on Sustainable Energy,* 2018.

[64] N. Gionfra, G. Sandou, H. Siguerdidjane, D. Faille, and P. Loevenbruck, "Wind farm distributed PSO-based control for constrained power generation maximization," *Renewable Energy,* vol. 133, pp. 103-117, 2019.

[65] X. Gao, K. Meng, Z. Y. Dong, D. Wang, M. S. El Moursi, and K. P. Wong, "Cooperation-Driven Distributed Control Scheme for Large-Scale Wind Farm Active Power Regulation," *IEEE Transactions on Energy Conversion,* vol. 32, no. 3, pp. 1240-1250, 2017.

[66] Y. Li, Z. Xu, J. Zhang, H. Yang, and K. P. Wong, "Variable Utilization-Level Scheme for Load-Sharing Control of Wind Farm," *IEEE Transactions on Energy Conversion,* vol. 33, no. 2, pp. 856-868, 2018.

[67] N. S. Naidu and B. Singh, "Grid-interfaced DFIG-based variable speed wind energy conversion system with power smoothening," *IEEE transactions on sustainable energy,* vol. 8, no. 1, pp. 51-58, 2017.

[68] P. Sorensen *et al.*, "Power fluctuations from large wind farms," *IEEE Transactions on Power Systems,* vol. 22, no. 3, pp. 958-965, 2007.

[69] Y. Jia *et al.*, "Powering China's sustainable development with renewable energies: current status and future trend," *Electric Power Components and Systems,* vol. 43, no. 8-10, pp. 1193-1204, 2015.

[70] A. M. Howlader, N. Urasaki, A. Yona, T. Senjyu, and A. Y. Saber, "A review of output power smoothing methods for wind energy conversion systems," *Renewable and Sustainable Energy Reviews,* vol. 26, pp. 135-146, 2013.

[71] B. Ni and C. Sourkounis, "Energy yield and power fluctuation of different control methods for wind energy converters," in *Industry Applications Society Annual Meeting (IAS), 2010 IEEE*, 2010, pp. 1-7: IEEE.

[72] Y. Li, Z. Xu, and K. P. Wong, "Advanced control strategies of PMSG-based wind turbines for system inertia support," *IEEE Trans. Power Syst,* vol. 32, no. 4, pp. 3027-3037, 2017.

[73] G. Shafiullah, A. M. Oo, A. S. Ali, and P. Wolfs, "Potential challenges of integrating large-scale wind energy into the power grid–A review," *Renewable and sustainable energy reviews,* vol. 20, pp. 306-321, 2013.

[74] J. C. Smith, M. R. Milligan, E. A. DeMeo, and B. Parsons, "Utility wind integration and operating impact state of the art," *IEEE transactions on power systems,* vol. 22, no. 3, pp. 900-908, 2007.

[75] G. Strbac, "Quantifying the system costs of additional renewables in 2020," *DTI report,* 2002.

[76] D. J. Swider and C. Weber, "The costs of wind's intermittency in Germany: application of a stochastic electricity market model," *International Transactions on Electrical Energy Systems,* vol. 17, no. 2, pp. 151-172, 2007.

[77] C. Abbey, K. Strunz, and G. Joos, "A knowledge-based approach for control of two-level energy storage for wind energy systems," *IEEE Transactions on Energy Conversion,* vol. 24, no. 2, pp. 539-547, 2009.

[78] Q. Jiang and H. Wang, "Two-time-scale coordination control for a battery energy storage system to mitigate wind power fluctuations," *IEEE Transactions on Energy Conversion,* vol. 28, no. 1, pp. 52-61, 2013.

[79] W. Li, G. Joós, and J. Bélanger, "Real-time simulation of a wind turbine generator coupled with a battery supercapacitor energy storage system," *IEEE Transactions on Industrial Electronics,* vol. 57, no. 4, pp. 1137-1145, 2010.

[80] X. Lyu, J. Zhao, Y. Jia, Z. Xu, and K. P. Wong, "Coordinated Control Strategies of PMSG-based Wind Turbine for Smoothing Power Fluctuations," *IEEE Transactions on Power Systems,* 2018.

[81] X. Zhao, Z. Yan, and X.-P. Zhang, "A wind-wave farm system with self-energy storage and smoothed power output," *IEEE Access,* vol. 4, pp. 8634-8642, 2016.

[82] Q. Jiang and H. Hong, "Wavelet-based capacity configuration and coordinated control of hybrid energy storage system for smoothing out wind power fluctuations," *IEEE Transactions on Power Systems,* vol. 28, no. 2, pp. 1363-1372, 2013.

[83] M. Khalid and A. Savkin, "Minimization and control of battery energy storage for wind power smoothing: Aggregated, distributed and semi-distributed storage," *Renewable Energy,* vol. 64, pp. 105-112, 2014.

[84] Y. Zhou, Z. Yan, and N. Li, "A novel state of charge feedback strategy in wind power smoothing based on short-term forecast and scenario analysis," *IEEE Transactions on Sustainable Energy,* vol. 8, no. 2, pp. 870-879, 2017.

[85] A. Addisu, L. George, P. Courbin, and V. Sciandra, "Smoothing of renewable energy generation using Gaussian-based method with power constraints," *Energy Procedia*, vol. 134, pp. 171-180, 2017.
[86] X. Li, Y. Li, X. Han, and D. Hui, "Application of fuzzy wavelet transform to smooth wind/PV hybrid power system output with battery energy storage system," *Energy Procedia*, vol. 12, pp. 994-1001, 2011.
[87] F. Diaz-Gonzalez, F. D. Bianchi, A. Sumper, and O. Gomis-Bellmunt, "Control of a flywheel energy storage system for power smoothing in wind power plants," *IEEE Transactions on Energy Conversion,* vol. 29, no. 1, pp. 204-214, 2014.
[88] W. Guo, L. Xiao, and S. Dai, "Enhancing low-voltage ride-through capability and smoothing output power of DFIG with a superconducting fault-current limiter–magnetic energy storage system," *IEEE Transactions on Energy Conversion,* vol. 27, no. 2, pp. 277-295, 2012.
[89] H. M. Hasanien, "A set-membership affine projection algorithm-based adaptive-controlled SMES units for wind farms output power smoothing," *IEEE Transactions on Sustainable Energy,* vol. 5, no. 4, pp. 1226-1233, 2014.
[90] G. Suvire and P. Mercado, "Active power control of a flywheel energy storage system for wind energy applications," *IET Renewable Power Generation,* vol. 6, no. 1, pp. 9-16, 2012.
[91] F. Zhang *et al.*, "Battery ESS planning for wind smoothing via variable-interval reference modulation and self-adaptive SOC control strategy," *IEEE Transactions on Sustainable Energy,* vol. 8, no. 2, pp. 695-707, 2017.
[92] A. Mullane and M. O'Malley, "The inertial response of induction-machine-based wind turbines," *IEEE Transactions on power systems,* vol. 20, no. 3, pp. 1496-1503, 2005.
[93] P. M. Ashton, C. S. Saunders, G. A. Taylor, A. M. Carter, and M. E. Bradley, "Inertia estimation of the GB power system using synchrophasor measurements," *IEEE Transactions on Power Systems,* vol. 30, no. 2, pp. 701-709, 2015.
[94] C. E. O. H. ENTSO-E, "P1-Policy 1: Load-Frequency Control and Performance," ed: Tech. Rep. 2000-130-003, May 2000.[Online]. Available: http://www. eurelectric. org, 2009.
[95] M. C. Di Piazza and G. Vitale, "Photovoltaic field emulation including dynamic and partial shadow conditions," *Applied Energy,* vol. 87, no. 3, pp. 814-823, 2010.
[96] *IEEE Recommended Practice for Functional and Performance Characteristics of Control Systems for Steam Turbine-Generator Units (122-1991)*. USA, 1992, p. 1.
[97] M. F. M. Arani and Y. A.-R. I. Mohamed, "Assessment and enhancement of a full-scale PMSG-based wind power generator performance under faults," *IEEE Transactions on Energy Conversion,* vol. 31, no. 2, pp. 728-739, 2016.
[98] J. Zhu, C. D. Booth, G. P. Adam, A. J. Roscoe, and C. G. Bright, "Inertia emulation control strategy for VSC-HVDC transmission systems," *IEEE Transactions on Power Systems,* vol. 28, no. 2, pp. 1277-1287, 2013.

[99] F. González-Longatt, P. Wall, and V. Terzija, "Wake effect in wind farm performance: Steady-state and dynamic behavior," *Renewable Energy*, vol. 39, no. 1, pp. 329-338, 2012.
[100] J. Jonkman, S. Butterfield, W. Musial, and G. Scott, "Definition of a 5-MW reference wind turbine for offshore system development," *National Renewable Energy Laboratory, Golden, CO, Technical Report No. NREL/TP-500-38060*, 2009.
[101] T. Ackermann, *Wind power in power systems*. John Wiley & Sons, 2005.
[102] N. A. Janssens, G. Lambin, and N. Bragard, "Active power control strategies of DFIG wind turbines," in *Power Tech, 2007 IEEE Lausanne*, 2007, pp. 516-521: IEEE.
[103] A. D. Papalexopoulos and P. E. Andrianesis, "Performance-based pricing of frequency regulation in electricity markets," *IEEE Transactions on Power Systems*, vol. 29, no. 1, pp. 441-449, 2014.
[104] Y. Chen, R. Leonard, M. Keyser, and J. Gardner, "Development of performance-based two-part regulating reserve compensation on miso energy and ancillary service market," *IEEE Transactions on Power Systems*, vol. 30, no. 1, pp. 142-155, 2015.
[105] A. Sadeghi-Mobarakeh and H. Mohsenian-Rad, "Performance Accuracy Scores in CAISO and MISO Regulation Markets: A Comparison based on Real Data and Mathematical Analysis," *IEEE Transactions on Power Systems*, 2018.
[106] K. S. Ko, S. Han, and D. K. Sung, "Performance-based settlement of frequency regulation for electric vehicle aggregators," *IEEE Transactions on Smart Grid*, vol. 9, no. 2, pp. 866-875, 2018.
[107] A. Sadeghi-Mobarakeh and H. Mohsenian-Rad, "Optimal bidding in performance-based regulation markets: An mpec analysis with system dynamics," *IEEE Transactions on Power Systems*, vol. 32, no. 2, pp. 1282-1292, 2017.
[108] J. Tamura, "Calculation method of losses and efficiency of wind generators," in *Wind energy conversion systems*: Springer, 2012, pp. 25-51.
[109] Online available: http://www.winddata.com/
[110] "Wind Turbines Connected to Grids with Voltages above 100kv", Danish Grid Code, online accessible: https://en.energinet.dk/